

An Experimental and Numerical Study on Decayed Azobé Sheet-piles



An Experimental and Numerical Study on Decayed Azobé Sheet-piles

by

Ganesh Shri Raam Kalaichelvi Senthil Kumar

to obtain the degree of Master of Science

at the Delft University of Technology,

to be defended publicly on Tuesday January 31, 2023 at 09:45 AM.

Student number: 5134978

Project duration: May 11, 2022 – January 31, 2023

Thesis committee: Prof. dr. ir. J.W.G. van de Kuilen, TU Delft (chair)

Dr. ir. G.J.P. Ravenshorst, TU Delft

Assoc. Prof. dr. A. Cicirello, TU Delft

Dr. A.C. Kamath, TU Delft

An electronic version of this thesis is available at <http://repository.tudelft.nl/>.

Preface

This thesis presents the results of an experimental and numerical study on decayed Azobé sheet-piles. This thesis marks the culmination of my Master's in Structural Engineering at TU Delft's Faculty of Civil Engineering and Geosciences, with a specialization in Steel, Timber and Composite structures.

"The Earth started to rebel when the carbon in the atmosphere began to swell"-Donna Maltz. As the saying goes, man has continuously been learning to live in harmony with nature and the construction industry stands no exception to this. From preferring buildings made only of concrete and steel at the beginning of the last century, a gradual transition has been happening from highly polluting materials to building with more sustainable materials. The goal of this thesis is to contribute to this transition, where long-used timber structural members can be reused by adopting an appropriate design strategy.

Taking up this project would not have been possible without the support and help of Jan-Willem Van de Kuilen, who trusted me with this and hence I would like to sincerely thank him for providing me with this opportunity. I would like to express my deepest gratitude to Abhijith Kamath for the continuous motivation he kept providing me with, his initial push that got me out of the negative headspace that I was in and got me working, the countless meeting and discussion hours he spent with me, the initiative and eagerness he kept showing for my thesis to progress through several phases until the end, without which I couldn't have possibly worked through and completed my thesis. I value the input from Geert Ravenshorst to improve the quality of my thesis. I am also thankful to Alice Cicirello, Michele Mirra, Rita Esposito and Francesco Messali for their valuable input during different stages of my thesis. I would also like to thank all the lab staff who helped me with the experiment tests, especially John Hermsen, Fred Schilperoort and Ruben.

I am thankful to my friends back in India as well as in Europe for their timely support, company and enjoyable moments. For those who have always been there for me, I am very grateful to my parents and Gowtham, who have always been there for me and have given me the chance to grow both personally and professionally. I would like to thank Arjun and Karthikeyan for their unconditional support throughout the course of my master's programme and for the insightful discussions we had. Finally, I would like to thank Lokesh who stood by and encouraged me. Without all your support, this wouldn't have been possible.

Ganesh Shri Raam Kalaichelvi Senthil Kumar
The Hague, January 2023

Abstract

Given the desire to construct more structures using sustainable building materials, demand for wood and other bio-based building materials has risen dramatically over the decade. While timber itself is a carbon-neutral material and can sometimes even be carbon-negative, reusing wooden structural members made that have been in service for several years can widen the approach to structural design using wood. In the extensive network of rivers and canal systems that the Netherlands has, the banks are often covered with sheet-pile walls and a majority of these are made of timber. Tropical hardwood, especially Azobé (*Lophira alata*), due to its high biological resistance to decay, is used to make these sheet-piles. However, when exposed to the groundwater table for a long period of time, the wood undergoes decay due to bacteria destroying the cellulose slowly, while the lignin remains constant, and over decades the large cellulose molecules are replaced by water making the walls weaker.

In this study, the characteristic mechanical properties of Azobé sheet-piles that have been in service for 57 years have been found, so that they can be assigned with an appropriate strength class and reused. Destructive, quasi-destructive and non-destructive tests have been performed on the sheet-pile boards to understand the correlation between them and to also ascertain to what level tests on timber specimens that do not affect their usability can be reliable. Since the knowledge of how visual grading can be performed on used, decayed structural timber, especially hardwood specimens is limited, a methodology has been developed in line with NEN-EN 14081-1 (2019) along with the definition of a visual decay score. The results from the RPD tests are quantified in terms of the resistographic measure value to identify whether, in tropical hardwood, is there any effect in the drilling direction and whether this value can qualitatively or quantitatively describe the actual mechanical strength of the sheet-pile boards. The stress-wave tests and the four-point bending test are used to calculate the strength and stiffness of the boards, which determine the characteristic values, that are also based on their wet density (at which the tests are conducted). The results obtained are also analyzed for occurring patterns in terms of the location of the board in the sheet-pile wall (top or bottom), testing configuration (E-side or W-side-up) and variation in thickness within the boards due to decay.

The bending test performed on the boards is modelled numerically in multiple iterations with curved-shell, layered-shell and 3D brick elements also varying the respective material models to find which one of them is best suitable to model bending of timber. The load-sharing mechanism observed when grouping multiple timber specimens has been simulated numerically to predict the characteristic load-sharing factor of the sheet-pile wall system.

Contents

Preface	iii
Abstract	v
Nomenclature	xii
List of Figures	xv
List of Tables	xvii
1 Introduction	1
1.1 Background	1
1.2 Research questions	2
1.3 Thesis outline	2
2 Literature Review	5
2.1 Hardwood as a sheet-pile material	5
2.1.1 Wood and hardwood	5
2.1.2 Azobé or ekki	6
2.1.3 Degradation types	7
2.1.4 Timber sheet-piles and their exposure zones	7
2.1.5 Structural loading and behaviour	7
2.2 Experimental testing methods - NDTs and SDTs	8
2.2.1 Visual inspection	9
2.2.2 Acoustic test	10
2.2.3 RPD	11
2.3 Experimental testing methods - DTs	12
2.3.1 Four-point bending test.	12
2.3.2 Grain angle measurement	13
2.3.3 Moisture test	13
2.4 Numerical modelling	14
2.4.1 Material model	14
2.4.2 Load sharing	14
2.4.3 Timber in DIANA	15
2.5 Summary	15
3 Experimental analysis - Method	17
3.1 Experiment outline	17
3.2 Material and setup	17
3.2.1 Cutting and pretreatment of sheet-piles	17
3.2.2 Weights and dimensions	19

3.3	Visual evaluation	20
3.3.1	Identification of visual characteristics	20
3.3.2	Visual Decay Score (VDS)	22
3.4	Stress-wave test	22
3.4.1	Equipment	22
3.4.2	Dynamic MOE calculation procedure	25
3.5	Resistance Penetration Drilling (RPD) test	25
3.5.1	Input variables	25
3.5.2	Testing and processing of data	26
3.5.3	Resistographic Measure (RM) calculation	27
3.6	Four-point bending test.	27
3.6.1	Test setup	28
3.6.2	Configurations and testing process	29
3.6.3	MOR calculation procedure	29
3.6.4	Force-displacement graph data processing	30
3.6.5	Global static MOE calculation procedure	32
3.7	Local MOE	33
3.7.1	Test setup	33
3.7.2	Local MOE calculation procedure	34
3.8	Grain deviation angle measurement.	35
3.9	Moisture test	35
3.9.1	Test setup	35
3.9.2	Calculation procedure	36
3.10	Compression test.	36
3.10.1	Test setup	37
3.10.2	Calculation of compression strength and MOE in compression	38
4	Experimental analysis - Results and Discussion	39
4.1	Overview of the results	39
4.1.1	Strength class allocation	40
4.1.2	Interpretation of the data	42
4.2	Distribution of acquired data	44
4.2.1	Dimensions and physical attributes	44
4.2.2	Non-destructive test results	45
4.2.3	Destructive test results	46
4.3	NDTs and DTs relation	47
4.3.1	In comparison with softwood and hardwoods	49
4.3.2	Correlation with density	50
4.4	RPD test - drill locations	51
4.5	Four-point bending test configurations	51
4.5.1	Impact of W and E side testing	54
4.6	Top vs Bottom boards	55
4.6.1	Individual parameters	55
4.6.2	Correlative parameters	59

4.7	Influence of geometry	60
4.7.1	Tongue and Grooves	60
4.7.2	Variation in thickness	60
4.8	Comparison of data from lasers and the load cell.	61
4.9	Compression test results	62
5	Numerical analysis	65
5.1	Outline	65
5.1.1	Idealization	66
5.1.2	Discretization	67
5.2	FE modelling - Individual sheet	67
5.2.1	Model-1	68
5.2.2	Model-2	69
5.2.3	Model-3	71
5.2.4	Results	72
5.2.5	Discussion	74
5.3	FE modelling - Sheet-pile wall system.	74
5.3.1	Characteristic bending strength	74
5.3.2	Using brick elements	75
5.3.3	Load-sharing factor.	76
5.3.4	Recommendation.	77
6	Conclusion and Recommendation	79
6.1	Research questions	79
6.2	Limitations	81
A	Appendix - A	83
A.1	Visual decay scores	83
A.1.1	VDS1	83
A.1.2	VDS2	84
A.1.3	VDS3	84
A.1.4	VDS4	85
A.2	Data entry sheet	86
A.3	Bending test failure patterns	88
B	Appendix - B	91
B.1	Samples with MC lower than FSP	91
C	Appendix - C	93
C.1	Things that could go wrong	93
C.2	Safety precautions	94
C.3	Test procedure	94
D	Appendix - D	99
D.1	RPD test	99
D.2	Four-point bending test	103
D.3	Compression test.	107

E	Appendix - E	109
E.1	Parametrization	109
E.2	Results	109
F	Appendix - F	111

Nomenclature

Abbreviations

AZ	Azobe
DT	Destructive Test
EN	ENglish
FSP	Fibre Saturation Point
LS01	Laser Sensor 01
LVDT	Linear Varialbe Differential Transformer
MC	Moisture Content
MOE	Modulus of Elasticity
MOR	Modulus of Rupture
MTG	Mechanical Timber Grader
NDT	Non Destructive Test
NEN	NEderlanse Norm
PNH	Province North Holland
QDT	Quasi Destructive Test
RM	Resistographic Measure
RPD	Resistance Penetration Drilling
SDT	Semi Destructive Test

Symbols

α	Slope of grain [°]
β_v	Volume change percentage per percentage MC [-]
ω	Moisture Content [%]
ρ_k	Characteristic density [kg/m ³]
$\rho_{mc12\%}$	Density at 12% moisture content [kg/m ³]
ρ_{wet}	Density at wet state [kg/m ³]
σ_{xx}	Axial stress component acting parallell x-axis
σ_{xy}	Shear stress component acting in the xy plane
$E_{m,mean}$	Characteristic mean bending stiffness [MPa]

$f - d$	Force-displacement
f_c	Compression strength [MPa]
$f_{m,k}$	Characteristic bending strength [MPa]
k_h	Depth adjustment factor [-]
k_l	Span adjustment factor [-]
$k_{b,mc}$	12% MC adjustment factor for bending strength [-]
k_{mc}	12% MC adjustment factor for MOE [-]
m_k	Characteristic 5 th percentile value
m_{mean}	Characteristic mean value
LSF	Load Sharing Factor [-]
MOE _c	MOE in compression [MPa]
MOE _d	Dynamic MOE [MPa]
MOE _{s,g}	Global static MOE [MPa]
MOE _{s,l}	Local static MOE [MPa]
MOR	Modulus of Rupture or Bending strength [MPa]
P ₅	5 th percentile value [-]
S/T	Span to thickness ratio [-]
VDS	Visual Decay Score [-]

List of Figures

1.1	Flow chart of the research approach	3
2.1	Typical cross-section of hardwood and softwood illustrating their annual/growth rings (Sandquist, 2011)	6
2.2	(a) Principle of the loading and boundary conditions of a sheet-pile wall supported by an anchor wall. Source: Van de Kuilen & Van Der Linden (1999) (b) Schematic representation of the global structure indicating the exposure zones. Source: Nowak et al. (2019)	8
2.3	Conceptual representation of non-destructive testing method. Source: Niemz & Mannes (2012)	9
2.4	Global MOE determination test setup Source: NEN-EN 408 (2010)	12
2.5	Position of the moisture test slices. Source: NEN 13183 (2002)	14
3.1	Flowchart of the experimental testing process	17
3.2	Schematic representation of the sheet-pile wall on site	18
3.3	Azobé sheet-pile as taken out from the soil	18
3.4	Typical W (a) and E (b) sides of the tested boards	18
3.5	Measurement location of the boards' physical dimensions	19
3.6	Typical cross-section of the timber board	20
3.7	Types of decay at different locations on each board (a) W side (b) E side: striped decay (c)E side: decay holes (d) E side: thickness wise decay of the groove (e) E side: thickness wise decay of the tongue	21
3.8	Decay stripes and their physical attributes	21
3.9	Stress wave test setup	22
3.10	Timber grader MTG equipment	23
3.11	Screenshot of the MTG timber grader application during testing	24
3.12	Screenshot of the MTG timber analyser application	24
3.13	RPD test setup	25
3.14	IML RESI PD-400 RPD testing equipment	25
3.15	(a) Drilling head (b) Drill needle	26
3.16	RPD test - drilling locations	26
3.17	Typical RPD test output graph	27
3.18	Schematic representation of the test setup	27
3.19	(a) Four-point bending test setup (b) Input interface of the testing application	28
3.20	Output interface of the testing application	28
3.21	Types of bending caused due to testing the boards using different configurations	29
3.22	Typical force-displacement graph generated directly from the result data	29
3.23	Typical force-displacement graphs (a) with local scattering and exponentially smoothed out (b) without local scattering	31
3.24	Processing the force-displacement data from experiments for $MOE_{s,1}$ calculation	32
3.25	Local MOE testing setup	33
3.26	Test setup for the determination of Local static MOE	34
3.27	Typical force-displacement graph obtained from the local MOE data	34
3.28	Fibre deviation angle measured on a bending tested board	35
3.29	Moisture testing oven maintained at a temperature of 103°	35
3.30	(a) Sample to be moisture tested cut from the board ready for the weigh-in (b) Moisture tested samples	36
3.31	Schematic representation of the compression test setup	37
3.32	Compression test setup	38

4.1	Distribution of the global static MOE in comparison to the literature	43
4.2	Distribution of the bending strength in comparison to the literature	44
4.3	Histogram - (a) length, (b) width (c) wet density and (d) 12% MC density of the boards	45
4.4	Histogram - (a) Thickness (b) VDS, (c) Dynamic MOE, (d) RM%	46
4.5	Histogram -(a) Global static MOE, (b) bending strength, (c) grain angle deviation and (d) moisture content	47
4.6	(a) Visual decay score vs Global static MOE (b) Visual decay score vs Bending strength	48
4.7	(a) Dynamic MOE vs Global static MOE (b) Local static MOE vs Global static MOE	48
4.8	(a) Bending strength vs Dynamic MOE (b) Bending strength vs Global static MOE	48
4.9	(a) Resistographic Measure vs Global static MOE (b) Resistographic Measure vs Bending strength	49
4.10	Bending strength vs Dynamic and Global MOE in reference to results from Ravenshorst (2015)	49
4.11	Local vs Global static MOE in reference to results from Ravenshorst (2015)	50
4.12	(a) Global static MOE vs Density _{wet} & Density _{12%} (b) Moisture content vs Density	50
4.13	(a) Resistographic measure vs Density (b) Bending strength vs Grain angle deviation	51
4.14	Resistographic Measure at various drill locations	51
4.15	Visual Decay Score: Configuration wise	52
4.16	Dynamic MOE: Configuration wise (a) Histogram (b) Box plot	52
4.17	Global static MOE: Configuration wise (a) Histogram (b) Box plot	52
4.18	Bending strength: Configuration wise (a) Histogram (b) Box plot	53
4.19	Dynamic MOE vs Global static MOE - Configuration wise	53
4.20	Bending strength vs Global static MOE - Configuration wise	54
4.21	Normalised value of each parameter	55
4.22	Boxplot - Ratio of W to E side RM values at different locations within each board	55
4.23	(a) Visual decay score vs Global static MOE (b) Dynamic MOE vs Global static MOE - sorted by side facing upwards during four-point bending test	55
4.24	(a) Resistographic measure vs Global static MOE (b) Bending strength vs Global static MOE - sorted by side facing upwards during four-point bending test	56
4.25	Top vs Bottom - Visual Decay Score	56
4.26	Boxplot distribution Top vs Bottom boards - (a) Dynamic MOE (b) Global static MOE	57
4.27	Top vs Bottom - Dynamic MOE	57
4.28	Top vs Bottom - Resistographic Measure	57
4.29	Top vs Bottom - Global static MOE	58
4.30	Configuration wise global static MOE - Top vs Bottom (a) Config I (b) Config II (c) Config III (d) Config IV	58
4.31	Top vs Bottom - Bending strength	59
4.32	(a) Boxplot distribution Top vs Bottom boards - Bending strength (b) Ratio of top to bottom counterpart boards	59
4.33	(a) Visual decay score and (b) Dynamic MOE vs Global static MOE - Top and bottom boards	59
4.34	(a) Resistographic measure and (b) Bending strength vs Global static MOE - Top and bottom boards	60
4.35	Cross-sections of the sheet-pile boards (a) assumed for calculation (hatched) vs ideal (dotted) (b) with ideal tongue and grooves (c) decayed (d) decayed and missing groove	60
4.36	Minimum, maximum and mean thickness of each board	61
4.37	Thickness variation within each board	61
4.38	Static MOE value calculated from different displacement measuring devices	62
4.39	Compression force-displacement plot for the specimen PNH40	62
4.40	(a) Compression strength vs Compression MOE (b) Compression strength vs Bending strength	63
4.41	(a) Resistographic measure vs Compression MOE (b) Resistographic measure vs Compression strength	63
5.1	Process involved in the determination of the LSF	65
5.2	Flowchart for conversion of the experimental model for numerical usage	66

5.3	(a) Finite element model and (b) Finite element mesh of Model-1	68
5.4	(a) Finite element model and (b) Finite element mesh of Model-2	70
5.5	Stress distribution at failure for a timber specimen subjected to three-point bending test. The real stress distribution (Left) and the bending strength are calculated using the formula 5.1 (Right). Source: Ravenshorst (2015)	70
5.6	(a) Finite element model and (b) Finite element mesh of Model-3	71
5.7	Load-displacement curve of the numerical models	73
5.8	Longitudinal stress distribution at mid-span in the Azobé board when the vertical prescribed displacement is (a) 12mm (b) (b)20mm (c)50mm	73
5.9	Calibrated $f - d$ curves of the board used for LSF determination in comparison with the experimental results (E- Experimental, N- Numerical).	75
5.10	Sheet-pile wall system of 5 boards based on model-3D	75
5.11	Detail of the tongue and groove joint modelled in the 3D sheet-pile wall system	76
5.12	Stress distribution at the mid-span for five sheet-pile wall system PQQQP just before tensile brittle cracking	76
A.1	PNH52-1 (a) Side W (b) Side E	83
A.2	PNH152-1 (a) Side W (b) Side E	84
A.3	PNH97 (a) Side W (b) Side E (c)Longitudinal section showing the striped decay	84
A.4	PNH34 (a) Side W (b) Side E (c)Part of groove in side E decayed and chipped off	85
A.5	PNH113 (a) Side W (b) Side E	85
A.6	PNH36 (a) Side W (b) Side E	86
A.7	PNH94 (a) Side W (b) Side E (c)Decay holes on side W (d) Decay holes on side E	86
A.8	Typical filled-in data entry sheet per specimen	87
A.9	Four-point bending test failure patterns	88
A.10	Cross grains visible after failure	89
B.1	All samples in comparison with samples with $MC < FSP$ (a) Bending strength vs MOE (b) MC vs 12% MC density	91
E.1	Experimental vs numerical force-displacement curve (a) W, (b) S	109
E.2	Force-displacement plot of different parametrized configurations	110
E.3	Contour plot of the stress along x-direction for SWWWS configuration showing the cross-section stress distribution of each board	110
F.1	RPD curves - drill at ideal location vs through a hole (PNH92-1)	111
F.2	RPD curves - drill at ideal location vs through a cavity (PNH87)	111

List of Tables

2.1	Elements/ factors that cause different types of degradation in wood. Source: Nowak et al., (2019)	7
2.2	List of semi and non-destructive tests available to test structural wood	8
2.3	Efficiency criteria of NDTs and SDTs with respect to timber assessment. Source: Riggio et al. (2014)	9
3.1	Specification of different levels of decay stripes	20
3.2	Parameters that determine the VDS of tested boards	22
3.3	Dynamic MOE calculation example	25
3.4	RPD testing equipment – part and input specifications	26
3.5	Four-point bending test configuration of a set of boards from each Azobé sheet-pile	29
3.6	MOR calculation example	30
3.7	$MOE_{s,global}$ calculation example	33
3.8	$MOE_{s,local}$ calculation example	35
3.9	MC% calculation example	36
3.10	Compression strength and stiffness calculation example	38
4.1	Overview of the test results - 1	40
4.2	Overview of the test results - 2	40
4.3	Properties of the tested boards adjusted to 12% MC	41
4.4	Characteristic values of the sheet-piles and the strength class	42
4.5	Comparison with results from literature	42
5.1	Finite element type	68
5.2	Material properties assigned in the FE model	69
5.3	Characteristics of iterative scheme	69
5.4	Finite element type	70
5.5	Material properties assigned in the FE model-2&3	71
5.6	Finite element type	72

Introduction

1.1. Background

Timber has historically been a versatile construction material, especially in the form of structural elements, and over the past few centuries, the emission of greenhouse gases by common construction materials like concrete and steel has led to the emphasis on using wood for its environmental friendliness. Employing wood in highly corrosive environments has been in practice for a long time and wood being used in pile foundations for weak soil can be dated back to the 12th century in most of the historical buildings in Venice (Abrami, 2005) and 16th century in the Netherlands for buildings as well as quay walls (Sass-Klaassen et al., 2008). Also, in the Netherlands, there are almost 7000km of stream banks that are protected, and 3500km of those are composed of timber sheet piling (Kamath, 2022). Hardwood, when compared to its counterpart, softwood, has been proven to be much more durable and resistant when exposed to extreme environmental conditions.

Azobé is a tropical hardwood species that is commonly used in the construction of sheet-piles, which are long, thin structural elements that are driven into the ground to provide support for streams, canal or river banks, cofferdams, and other structures. When compared to sheet-piles made of steel, hardwood ones stand out as an environmentally friendly alternative especially when the height of the unsupported soil is around 1 m. In essence, these sheet-piles are multiple strips of hardwood joined together and held in place in the form of a soil-retaining surface. The timber sheet-piles work by supporting the active part of the soil from losing sliding over while exerting load on the passive part of the soil as explained through figure 3.2. These sheet-piles can be cantilevered by fixing their bottom length onto the ground or can also be anchored to the active part of the soil.

Although highly durable and decay-resistant, the thin geometry of the sheet-piles results in more surface area of the boards (compared to a thicker beam with the same cross-sectional area). The high surface area results in relatively higher exposure to aggressive environmental conditions compared to a thicker specimen with a similar cross-sectional area. When exposed to such conditions for a long period of time, the Azobé sheet-piles may undergo decay and progressively lose their structural integrity over time. The aim of this thesis is to evaluate the serviceability of sheet-piles that were in use since 1966 in the North Holland province.

The load-carrying capacity of the sheet-piles will have to be determined in order to evaluate them, and the application of load on these sheet-piles, either numerically, analytically or experimentally needs to be in line with their loading pattern in-site. The initial aim is to explore how this capacity can be determined in the most effective way possible and to also identify what type of degradation timber wooden sheet-piles have undergone. This would lead to the development of a methodology for testing and evaluating the timber sheet-piles.

The most recent relevant research available is by Novak et al. (2019), which mainly explores the possibility of how much non-destructive tests can be relied upon to analyze decayed pine wood sheet-piles. Anyhow, Sousa et al. (2017) discuss in detail the prediction of the mechanical properties of timber

structural elements by only using non-destructive tests. With regard to Azobé and its mechanical properties, Van de Kuilen & Blass (2005) conducted experimental tests on several types of structural elements made of Azobé to analyze their mechanical properties. Though not with decayed sheet-pile boards, Van de Kuilen and Van Der Linden (1999) studied new unused Azobé sheet-piles by four-point bend-testing and also by calibrating the results with numerical models for their load-sharing factor.

1.2. Research questions

The primary question is: Can the decay in tropical hardwood that affects its load-bearing capacity when used as a sheet-pile material be predicted using non-destructive methods? How necessary are the destructive tests? To accompany this question, questions that can detail the process involved to find a solution to the above question are listed below.

Literature review

1. What are the types of decay and decay patterns observed in used Azobé sheet-piles?
2. How can the boards be assigned a score based on the decay, how can this score be related to the mechanical strength?
3. Can RPD analysis be a reliable method to understand the decay?
4. What is the residual strength and stiffness of the sheet-piles that have been in service?
5. Can the Azobé sheet-piles be reused, and how can they be graded?
6. How accurately can a sheet-pile subjected to bending be numerically modelled in terms of the material model, geometry and boundary conditions?
7. What is the applicability of the material model in LSF analysis?

1.3. Thesis outline

The research focuses on its primary objectives as mentioned in section 1.2. The experiments will be done in accordance with the relevant NENs and for the numerical analysis, the research by Van de Kuilen and Van Der Linder (1999) to find the characteristic bending strength experimentally and to verify it with numerical modelling will be taken as a basis.

In figure 1.1, a research methodology is described in order to accomplish the goal and respond to the research questions for the thesis. To offer a solution, various strategies are required. The next paragraphs detail the various strategies.

In Chapter 2, the study and findings from various kinds of literature that deal with topics directly and indirectly related to wood have been discussed. In section 2.1 the basic characteristics of wood, its anatomy and its relevance as a structural material are explained, also parallely drawing the differences between the more conventional softwood and the material under investigation, hardwood. In section 2.1.3, the different types of decays that can occur in wood that is exposed to different environmental conditions and how this specifically relates to the current application, sheet-piles is focused on along with how the structural system works in a sheet-pile wall system made of wood. The chapter also discusses with reference to NENs and other research, how each test to assess mechanical strength can be performed. Section 2.4, the literature study of modelling wood in FEA and the process of determination of load-sharing factor is performed. The findings from the chapter lead to the following sub-questions:

1. What are the types of degradation that hardwood can go through and how are each of these relevant in the case of sheet-piles?
2. How is decay analyzed and modelled in structural elements made of hardwood?
3. Which physical or mechanical properties are relevant when evaluating sheet-piles?
4. What are the non-destructive, semi-destructive and destructive tests applicable to obtain these attributes?

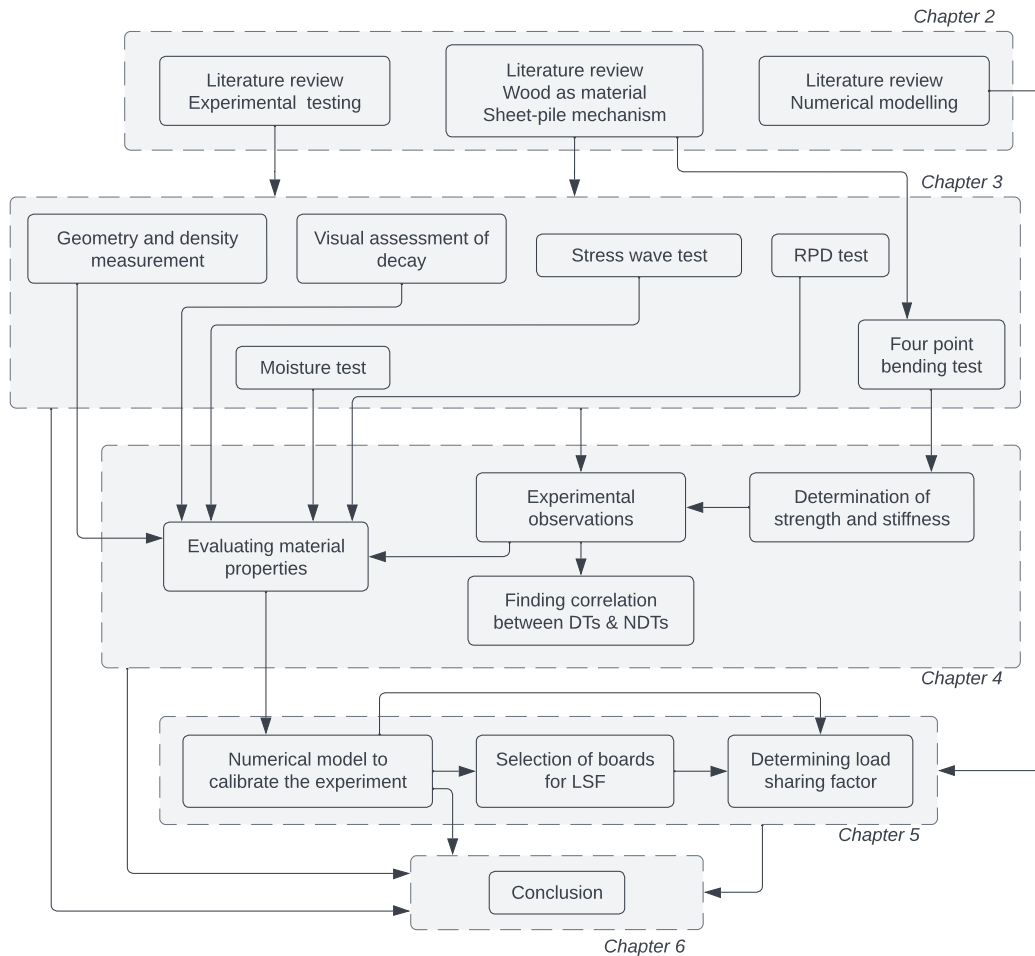


Figure 1.1: Flow chart of the research approach

Chapter 3 explains in detail the various steps involved in each experimental test that was performed to study the decay and to find the mechanical strength of the sheet-pile boards. The step-by-step process in the processing of the data obtained from each of these experimental tests is also elaborated on in the chapter. The procedure involved in each experiment provides data that can be analyzed to fulfil the research questions and the following sub-questions:

1. How can the results from the four-point bending tests justify the failure mechanism occurring in timber sheet-piles that were cantilevered in-site?
2. Is there a pattern that can be observed in the decay of different zones in each sheet-pile?
3. Can the clear correlation that is observed between bending strength, and static and dynamic bending modulus in unused hardwood sheet-piles be expanded to decayed ones?
4. By studying the relationship between the destructive and non-destructive tests, can the methodology to predict the load-carrying capacity of sheet-piles be simplified to performing semi and/or non-destructive only?

In chapter 4, the analysis and discussion of the results from experimental tests are presented along with the strength class allocation based on the characteristic strength, stiffness and density value of the sheet-pile boards. The correlation between the destructive and non-destructive tests has also been checked. Several bases for comparison are drawn from the results obtained, like the influence of the testing configuration, the influence of whether the board belonged to the top/ bottom part of the sheet-pile and how much the variation in the thickness within each board due to decay and these comparisons are analysed and discussed.

The load-sharing factor determination process is explained in detail in chapter 5. The pros and cons of adopting different material models that take into account different aspects of the behaviour of timber are explained using different iterations of numerical models. The load-sharing factor has been approximated and the feasibility of such a study is also presented. The results of the experimental tests form the basis and eventually the input for the numerical models presented in the chapter. The recommended process that involves Monte Carlo simulation is also explained in detail. The sub-questions that are addressed in the chapter are:

1. How can the outcomes from the experiments be applied to the numerical model and what connections exist between the outcomes of the experiments and the numerical model?
2. By combining past literature that numerically analyzed sheet-piles with the experimental and numerical results from this project, can the load-sharing factor in a sheet-pile wall system be studied?
3. In a sheet-pile wall system with sheet-piles of significant difference in strength and stiffness, how significant is their arrangement? Does the location of the mechanically weaker sheet-pile matter?

The thesis has been concluded in chapter 6 by comparing the strength classes of freshly sawn Azobé with that of the sheet-pile boards tested in this study. The scope and limitations of the different experimental tests conducted in this investigation and also the numerical models developed for the load-sharing factor analysis are presented.

2

Literature Review

In this chapter, the testing methods available for timber, specifically hardwood specimens that are also suitable for sheet-piles are discussed. The loading mechanism in sheet-piles and experimental investigation carried out to study timber that had been in service for several years are reviewed along with the findings. In addition, numerical models relevant to the bending behaviour of timber and the numerical investigations performed on the load-sharing factor of sheet-pile walls are also presented in detail.

2.1. Hardwood as a sheet-pile material

2.1.1. Wood and hardwood

Timber has proven to be a durable and versatile construction material throughout human history, addressing different types of demand such as structural, aesthetic, eco-friendly, etc. (G. J. P. Ravenshorst, 2015). Owing to such versatility, one such application of structural timber is on the bank of rivers, backwaters, deltas, etc., and places where the ground water table is high, or where the structural wooden parts are completely exposed to water. Almost all the historic buildings in Venice are constructed using short and closely spaced wooden piles (Ceccato et al., 2013). Wooden piles are extensively used in most of the ancient buildings for foundation, especially in the Scandinavian countries and in many parts of the Netherlands (Nowak et al., 2019). Wood undergoes bacterial decay when constantly exposed to water and also when placed in an air-water interface and this decay can be better understood by studying their structural degradation (R. K. Klaassen & Creemers, 2012).

Seed plants which eventually grow into trees, form the primary part of every terrestrial ecosystem, and can botanically be classified into two general categories, gymnosperms and angiosperms, based on whether the seeds in the ovary of a flower are naked or inside a cone, respectively (Barker & Owen, 1999). Gymnosperms and angiosperms grow out to yield hardwood and softwood, respectively and they distinctly vary in terms of their physical and mechanical properties. In general, for comparable densities, hardwoods offer better mechanical resistance and are less susceptible to decay when compared to softwoods. This can be related to the higher carbon content in the softwoods (Chaouch et al., 2010).

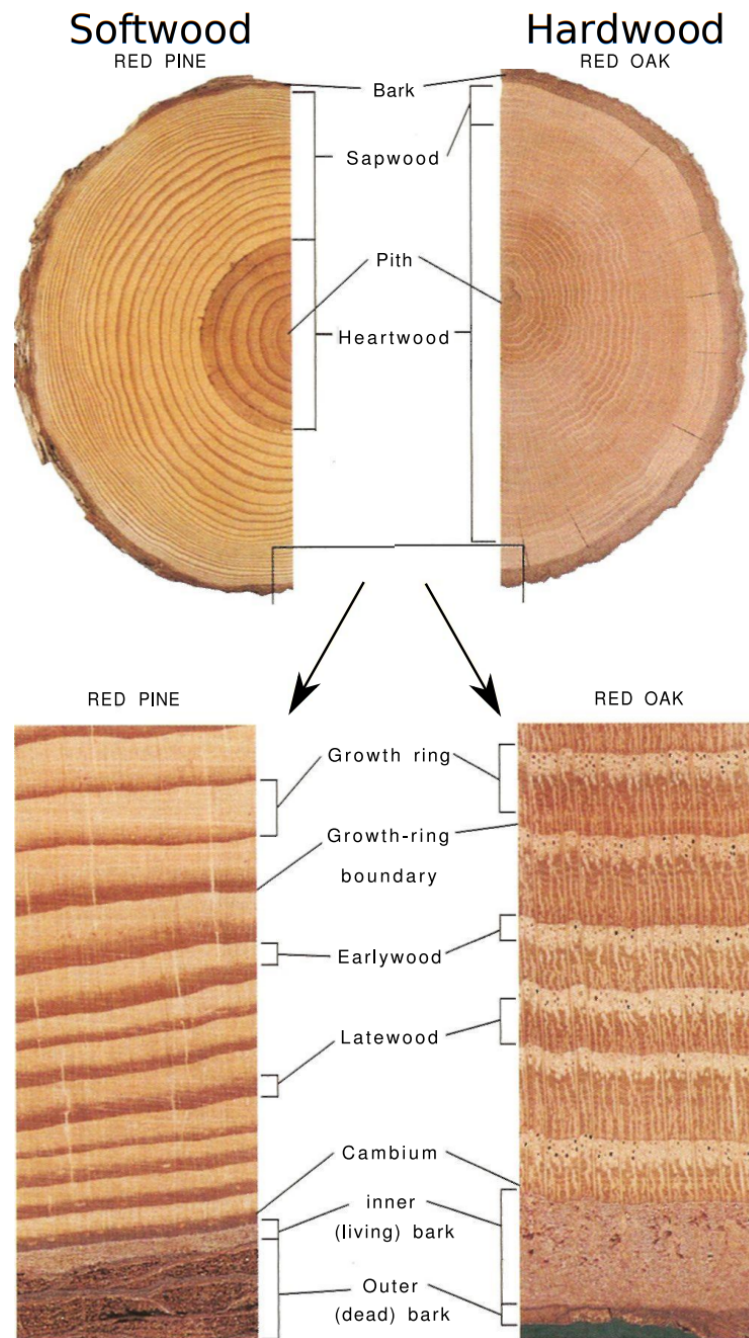


Figure 2.1: Typical cross-section of hardwood and softwood illustrating their annual/growth rings (Sandquist, 2011)

2.1.2. Azobé or ekki

With good mechanical performance and better natural durability when compared to softwoods, in the Netherlands, Germany, UK, and Belgium, hardwood is used when the structural member is exposed to severe environmental conditions (Van de Kuilen & BlaSS, 2005). Since the Second World War, in the Netherlands, the prominent hardwood species used for such applications is Azobé (*Lophira alata*), also known as ekki. Azobé is dark red/ brown in colour with interlocking grains and is mainly found in the tropics of the West African region. Though Azobé is not completely immune to marine borer attacks, its heartwood, unless affected by local conditions is immune to the attack. The species shows high resistance to acidic conditions and weathering (Wood Handbook, 2010).

2.1.3. Degradation types

Over time, timber undergoes degradation due to several external factors and Azobé is no exception. These external factors can be grouped and classified based on the process involved in the reconversion of the wooden material into CO₂ and H₂O as shown in table 2.1 (Nilsson & Rowell, 2012).

Table 2.1: Elements/ factors that cause different types of degradation in wood. Source: Nowak et al., (2019)

Type of degradation	Elements/ Factors causing degradation
Weather	UV radiation, water (rain, dew, acid rain), heat
Biological	Fungi, bacteria, insects, termites
Chemical	Oxidation and reduction, hydrolysis, free radical reactions
Mechanical	Wind, dust, snow, hailstorm, abrasion
Interaction with water	Swelling & shrinking, freezing, erosion

2.1.4. Timber sheet-piles and their exposure zones

The timber sheet-pile wall investigated in the current study is made of Azobé sheets that are connected to each other using tongue and groove joints. Since the sheet-piles are continuously exposed to water as well as saturated soil, the hazards leading to the deterioration in their structural serviceability could broadly be classified as varying water levels, excessive loading, and decomposition of wood in water (Nowak et al., 2019). Since the water level and the loading conditions are almost similar throughout the year, decomposition due to moisture exposure could be the main cause of the decay of the sheets. These sheets are partially exposed to the atmosphere as well. The decay occurs when the fungi and bacteria slowly destroy the cellulose layer and replace them with water while the lignin remains intact (K. Klaassen et al., 2015).

2.1.5. Structural loading and behaviour

The sheet-piles in action are loaded by the active and passive parts of the soil before the water starts exerting its pressure. As shown in figure 2.2a, the loading of sheet-piles can be conceptualized taking the loads and support from the soil and water into account (Van de Kuilen & Van Der Linden, 1999). To study the decay in sheet-piles, understanding the potential zones that are exposed to different environmental conditions is important. From the study conducted by Nowak et al., (2019), timber sheet-piles that were taken out from their service environment after 70 years showed a significant difference in cross-sectional dimensions and quality when compared to the original condition. The timber section can be observed with different parts of it under distinctly different environmental conditions: fully embedded into the ground and sandwiched between active and passive parts of the soil, exposed only to water, and exposed to varying levels of water and air. Based on these conditions, each sheet-pile can be divided into three zones (Nowak et al., 2019) as shown in figure 2.2b.

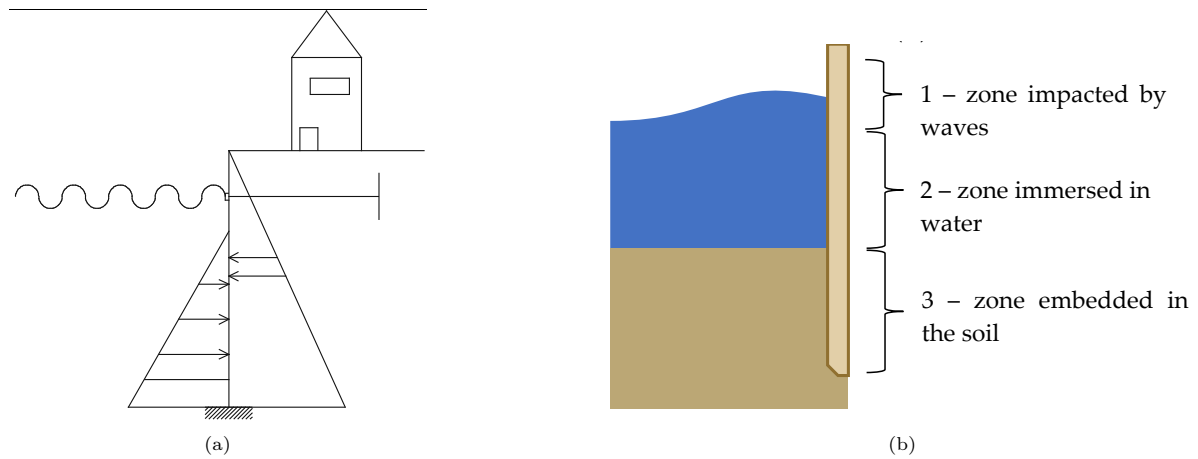


Figure 2.2: (a) Principle of the loading and boundary conditions of a sheet-pile wall supported by an anchor wall. Source: Van de Kuilen & Van Der Linden (1999) (b) Schematic representation of the global structure indicating the exposure zones. Source: Nowak et al. (2019)

2.2. Experimental testing methods - NDTs and SDTs

When developing a methodology to assess the quality of wood subjected to different environmental conditions, quantifying their technical condition, and relating them to the global structure becomes necessary. Material testing for wooden specimens can broadly be classified into three categories: destructive tests (DT), semi-destructive tests (SDT) and non-destructive tests (NDT) (Tannert et al., 2014). Both non-destructive and destructive methods should be utilized to gather comprehensive data on the values of the physical and mechanical characteristics of wood. The information obtained this way is sufficient for further static load evaluations of the structural members or the entire structure if the findings of the two testing methods are confirmed to correlate. Various types of semi-destructive tests and non-destructive tests are listed in table 2.2, along with their classification methods (Riggio et al., 2014), (Tannert et al., 2014), (Dackermann et al., 2014), (Kasal & Tannert, 2011).

Table 2.2: List of semi and non-destructive tests available to test structural wood

Organoleptic Methods	Acoustic radiation and vibration-based Methods	Radiographic Methods	Semi Destructive Methods
Visual evaluation	Stress wave with time-of-flight method	X-ray CT	Drilling resistance
Acoustic evaluation	Ultrasonic tomography	Gamma rays	Core drilling
Fragrance evaluation	Ultrasonic echo		Pin pushing
	Ground penetrating radar		Needle penetration
	Near-infrared spectrometry		Screw withdrawal
			Tensile strength testing micro specimens
			Janka Hardness test

As a result of the fact that a single parameter is typically insufficient to accurately represent the condition of an object or substance, multisensor approaches, or the combination of numerous measuring methods, are the preferred options (Niemz & Mannes, 2012). When testing timber, simple sound transmission measures, for instance, hardly ever pick up smaller flaws like tiny knots or cracks (Dackermann et al., 2014). Most automated production processes nowadays combine a variety of measurement tools to determine whether the goal parameters, which are calculated using mathematical techniques, are in compliance with the recommended values. These techniques are typically too complex, production

method specific and difficult to be applied to the evaluation of objects that undergo ageing, hence their usage is restricted to a select few unique situations (Niemz & Mannes, 2012). Figure 2.3 illustrates the essential idea of NDTs and their different combinations.

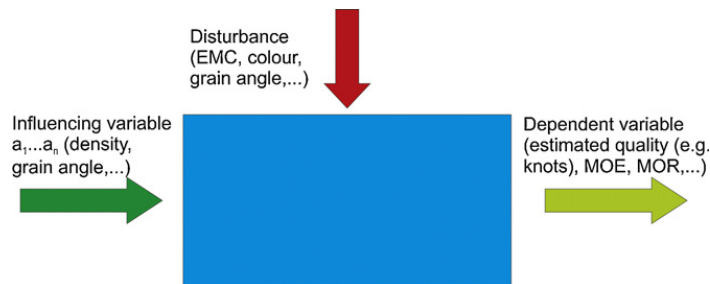


Figure 2.3: Conceptual representation of non-destructive testing method. Source: Niemz & Mannes (2012)

Two categories of non-destructive and quasi-non-destructive testing exist, global testing (such as visual inspection, ultrasonic, and stress wave techniques), and local testing (such as drill resistance, core drilling, and hardness testing). Based on the main aspect under consideration, table 2.3 provides an overview of different NDT and SDT methods as well as a matrix for determining which methods are most appropriate for certain projects or needs. No single method is appropriate for every project, and some methods only provide sparse data for a particular factor. Table 2.3 highlights the significance of combining several ways to produce information pertinent to the aspects of concern and address specific tasks (Riggio et al., 2014).

Table 2.3: Efficiency criteria of NDTs and SDTs with respect to timber assessment. Source: Riggio et al. (2014)

Method	Locate deterioration	Quantify deterioration	Assess/ Determine stiffness
Visual evaluation	Limited	Limited	
Stress wave	Limited	Limited	Limited/ Estimate
Ground penetrating radar	Limited		
Near-infrared spectrometry	Limited		
Drilling resistance	Yes	Yes	Limited
Core drilling	Yes		Estimate
Pin Pushing	Yes	Limited	
Needle penetration	Limited		Limited
Screw withdrawal	Limited		Limited
Tension micro specimens			Estimate
Janka Hardness test	Limited		Limited

2.2.1. Visual inspection

Visual inspection and grading are typically the initial stages in the assessment of aged timber structures. It includes observing the specimens macroscopically to study the decay patterns. This kind of technique can be used systematically, but in general, it yields crucial data regarding the background and current state of the material. When visually assessing timber structures that have evidently undergone decay, the percentage of bio-deterioration can be calculated according to the NEN 1311 (1997) standard that recommends measuring the dimensions of each rectangle that encloses the degraded part or the stain caused by insects or fungi.

The timber beam specimens used in the experimental study performed by (Ceccotti & Togni, 1996) had undergone thorough evaluation including the following steps:

1. Providing a chart showing all the beams' faces, serving as a sort of "map" of the distribution of decay and defects.

2. Predicting internal and invisible anomalies.
3. Assessing the critical section and the remaining portion that is still operational.

The methodology developed by Anagnostopoulou & Pournou (2013) to assess timber conditions in historic buildings also included a similar procedure but was more detailed. The method included calculation of the percentage of surface decay by mapping the decayed area on graph paper and elaborating them using AutoCAD, followed by classification of the obtained percentage values in a seven-point grading system according to the E7-90 standard. The decayed sheets also need to be checked if their tongues and grooves are still intact and if yes, their dimensions need to be cross-checked with the NEN 5493 (2010) standard.

2.2.2. Acoustic test

Basics and theory

The way sound travels through wood is directly impacted by changes to its mechanical and physical qualities (Dackermann et al., 2014). This idea forms the foundation of one of the oldest and still most used methods for spotting inner damage in trees, wood, and timber structures. The process of stress wave propagation in wood is directly influenced by its mechanical and physical characteristics. Stress waves generally move more quickly through clear, high-quality wood than through degraded, low-quality wood. The internal state of a wood specimen can be fairly precisely assessed by measuring the wave transmission time across or through the fibres in the specimen (Wang et al., 2004).

By striking the surface of the timber with an item (usually a hammer), sound waves are produced that can be used to detect flaws like deterioration and inner cavities. Alternatively, other sound waves can also be produced by generating the wave inside an external device and then allowing the wave to pass through the specimen by keeping the device in contact with the specimen. By analyzing the velocity of these sound waves that propagate within the tested material, one can assess the qualities of wood using acoustic testing techniques like ultrasonic and stress wave techniques. The technique can be used to calculate specific mechanical properties of a material, including its elasticity modulus, and to find internal structural discontinuities (Nowak et al., 2019).

An easy and effective measuring method for determining the internal soundness and condition of structural elements as well as stiffness characteristics for structural analysis is stress-wave propagation measurement. To accurately estimate the structural performance of in situ elements and detect both internal and exterior damage, this approach needs the right measurement strategy and approach. In the specific case of assessing timber boards that are subjected mainly to bending along the length, rather than stress-wave testing at different locations along the length, one measurement along the length would be meaningful (Lechner et al., 2014). Under ideal measuring conditions and geometry of multiple specimens, the higher velocity of the stress-wave would always relate to higher stiffness (Ross et al., 1999). The dynamic bending modulus of elasticity (MOE_d) can empirically be related to the measured velocity of the stress wave based on the one-dimensional theory. The calculated dynamic MOE, even though should be theoretically valid only for homogeneous and isotropic materials, in the study by Dackermann et al. (2014), it was found to be appropriate to describe the wave behaviour in timber, thereby proving its applicability for timber specimens.

Several kinds of devices that measure the properties of the propagating waves exist. Usually, an impact hammer that is instrumented with a sensor (such as an accelerometer or force sensor) or a regular hammer that has a separate sensor that is placed at the impact site will be used to strike one side of the examined specimen. The sensor emits a start signal to a timer at the moment of impact. An additional sensor, located straight across from the side of the impact area, detects the arrival of the stress wave and provides a stop signal to the timer when it reaches the opposite side of the timber specimen. The measuring device thus calculates the time of flight or the frequency of the stress wave. The velocity of the wave can be estimated and utilized to evaluate the internal physical conditions using the measured times and the calculated distance between the hit place and the second sensor (Dackermann et al., 2014).

Types

Stress wave and acoustic wave tests can be performed in two different ways: directly and indirectly (Nowak et al., 2019). The direct method entails sending a signal from the transmitting probe to the

receiving probe while positioning the probes on either side of the sample being evaluated. With the indirect method, the signal is registered as reflected and hence there is no need to install probes on the sample's opposing sides hence is also called the echo method. Since only unilateral access is required, this method's field of applicability can be much wider compared to the direct method. During the echo test, the impact hammer can be a hammer without any sensor attached to it while on the other side of the impact, a device that detects the wave frequency is placed in position.

Interpretation of results

For the stress wave method, the velocity of the propagating sound wave, V can be defined as:

$$V = L * f \quad (2.1)$$

where L is the distance that the stress wave will have propagated between the measuring points and f is the frequency of the wave which is dependent on the time taken to cover the distance. Using the velocity of the propagating stress wave, the dynamic modulus of elasticity, MOE_d can be calculated from the formula:

$$MOE_d = V^2 * \rho \quad (2.2)$$

where MOE_d is the dynamic modulus of elasticity, V is the velocity of the induced wave and ρ is the mass density. The sound wave propagation speed for wood without substantial structural faults is 3500-5000 m/s along the grain (Dackermann et al., 2014). Values that deviate from this range usually indicate internal discontinuities in the material structure (Wang et al., 2004).

2.2.3. RPD

Theoretical background

The relatively weak correlation between the measured non-destructive parameters and the actual material strength for strength forecasts is a disadvantage of NDT. Between destructive and completely non-destructive methods of strength assessment, SDT fills the gap. Small parts of the specimens are frequently removed during SDTs while preserving the integrity of the member to determine elastic and strength characteristics (Tannert et al., 2014). Resistance drilling is one of the common NDTs that involves evaluating the status of structural timber components by analyzing the relative density profiles of wood (Tannert et al., 2014), (Dolwin et al., 1999), (Gard & Van de Kuilen, 2018), (Wang et al., 2005). This test allows the user to look for signs of decay, insect damage, fissures, invisible beams, and concealed components. Local measurements are made while following the path of a drill bit with a small diameter. Different species and even different trees within the same species may exhibit different levels of penetration resistance depending on the pattern of growth and the amount of extractives, resins, and reaction wood (Dolwin et al., 1999). It may also differ between various areas of the tree. Heartwood and response zones could potentially have an impact on it.

Two forces: pressure and torsion force, are required to drill through the wood. Pressure force guarantees that there is friction between the drill head and the wood, allowing the drill to cut the wood when torsional force is present, and hence the former plays a key role (Gard & Van de Kuilen, 2018). The direction of drilling determines the amount of energy required to shear the wood's fibres. Only a small portion of the energy needed to cut a fibre perpendicular to the grain is used when cutting a fibre parallel to the fibre direction. As a result, it makes sense to always drill exactly perpendicular to the direction of the grain in order to prevent interpretation errors.

Resistographic measure calculation

The resistance measured for the compression and torsional forces by the testing device can be quantified in terms of the Resistographic Measure (RM). RM can be defined as the ratio of the area of the resistance curve in drill resistance vs depth graph obtained from the experiment (Feio et al., 2005) as shown in equation 2.3. In a similar fashion, the Feed Measure (FM) can be calculated using the formula 2.4 (Nowak et al., 2019). The FM and RM values are usually highly correlative and when used to compare with other test results, either of these parameters can be used, preferably the resistographic measure (Sharapov et al., 2019).

$$RM = \frac{\int_0^h RA \cdot dh}{h} \quad (2.3)$$

$$RM = \frac{\int_0^h FM \cdot dh}{h} \quad (2.4)$$

where,

$\int_0^h RA \cdot dh$ is the area under the drill resistance curve;

h is the drilling depth;

$\int_0^h FM \cdot dh$ is the area under the feed resistance curve.

2.3. Experimental testing methods - DTs

2.3.1. Four-point bending test

The effect of bending on the pile sheets exposed to different levels of environmental conditions plays a crucial role in the location of failure of the sheet-pile. Also based on the NDTs and SDTs, it would become prominent that interface between zone-1 and zone-2 would be crucial to check for bending test. The sheet-piles can be analysed by flatwise four-point bending test through which their bending strength and modulus of elasticity can be measured along with the tongue and groove profiles (Van de Kuilen & Van Der Linden, 1999). It is important that the specimens are tested with moisture content above their fibre saturation point and the loading was continued until failure occurred so that the plasticity that occurs in the boards can be studied.

For the determination of the global bending modulus of elasticity of the Azobé sheet-piles, the following checks and procedures from NEN-EN 408 (2010) must be followed:

1. The length of the testing board should be at least 19 times its thickness.
2. The span with which the board is tested and the distance between one of the supports and the nearest loading (a) point must be within the range of $18T \pm 3T$ and $6T \pm 1.5T$, where T is the thickness of the board as shown in the figure 2.4.

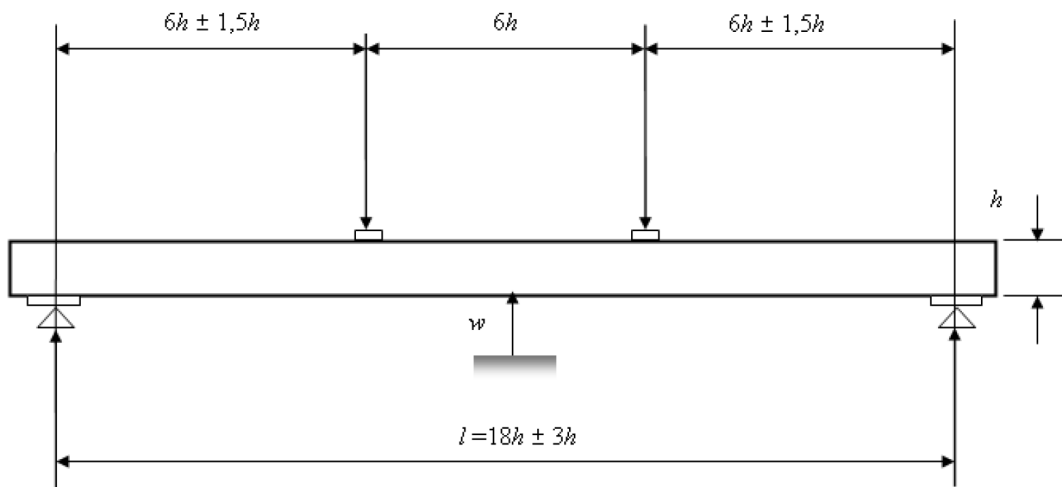


Figure 2.4: Global MOE determination test setup Source: NEN-EN 408 (2010)

3. The loading equipment must be able to measure the load accurately to 1% of the load applied to the specimen.
4. The loading rate should not be greater than 3/1000 times the thickness of the board.
5. The deformation w must be determined with an accuracy of 1% at the centre of the span from the centre of the tension or compression face.
6. Once the load and displacement data is acquired, the longest portion between $0.1F_{max}$ and $0.4F_{max}$ yields a correlation coefficient of at least 0.99. This range should cover a minimum range between $0.2F_{max}$ and $0.3F_{max}$.

7. For F_2 , w_2 and F_1 , w_1 being the maximum and minimum force and displacement values in the selected force-displacement range, respectively, G being the shear modulus of the specimen, the global modulus of elasticity can be calculated from the equation 2.5. Since the strength class allocation is performed based on NEN-EN 384 (2022), the shear modulus G can be considered to be infinite.

$$MOE_s = \frac{3al^2 - 4a^3}{2bh^3 \left(2 \frac{w_2 - w_1}{F_2 - F_1} - \frac{6a}{5Gbh} \right)} \quad (2.5)$$

where,

MOE_s is the static modulus of elasticity in bending;

a is the distance between one of the supports and the closest loading point;

l is the span between the supports;

b is the width of the beam;

h is the depth of the beam.

8. The bending strength can be calculated from the equation 2.6 with an accuracy of 1%.

$$f_m = \frac{3Fa}{bh^2} \quad (2.6)$$

where,

f_m is the bending strength of the tested beam;

F is the peak force value that can be applied on the beam that is tested.

2.3.2. Grain angle measurement

The slope of the grain is the primary factor affecting the bending strength of tropical hardwood timber. Although for softwood, the most governing strength-reducing parameter is the knot ratio, for tropical hardwoods, the most important strength-reducing characteristic is the slope of grain (G. Ravenshorst et al., 2020). The slope of the grain can be defined as the grain angle's deviation from the longitudinal axis on the plane of bending.

Although a precise threshold value is specified in the grading regulations, it is challenging to visually analyse the global slope of grain in these hardwoods. For beech, which is a hardwood, though it was difficult to determine the slope of grain during the grading process, Ehrhart et al. (2018) were able to measure the drying cracks that follow the slope of grain normally. This proves that a better indication of the grain angle deviation is provided by the grain slope determined after testing. However, it still cannot adequately characterise the Hankinson relationship. It is recommended by Ravenshorst et al. (2020) that in addition to the visual grading, that is stated by the NEN-EN 384 (2022) specifically for softwoods which involves measuring the knot size and of the density of the specimens, for hardwoods, the slope of grain is a necessary parameter that can explain the strength reduction.

2.3.3. Moisture test

In timber, MC (Moisture Content) stands for the ratio of water content to wood content. The MC can be determined in two different ways: direct and indirect. Most of the indirect methods belong to the NDT type while the direct method falls right under the DT type. Some of the indirect methods to determine MC are the resistance method, capacitance method, and hygrometric method (Riggio et al., 2014). Though MC of structural timber can be measured by means of indirect methods, they have their own limitations and in general when the MC test is not performed on-site or when the specimen is no longer required in intact condition for further evaluation after the MC test has been performed, the direct method must be followed. For the direct method, the MC of the timber specimen is described as the weight of water in wood expressed as a proportion of the weight of material that has been dried in an oven.

According to this NEN-EN 13183-1 (2002) in which the procedure for the direct method is stated in detail, a test slice is cut from the specimen for which the MC must be assessed as shown in figure 2.5, measured for its weight with an accuracy of 0.1 g and then dried inside an oven at $(103 \pm 2)^\circ\text{C}$ until there is less than 0.1% variation in mass between two subsequent weigh-ins timed apart by two hours.

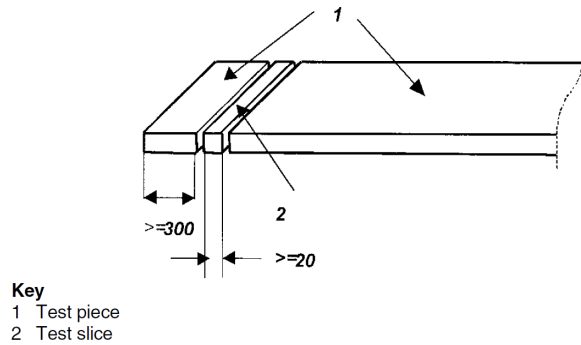


Figure 2.5: Position of the moisture test slices. Source: NEN 13183 (2002)

The standard also recommends not using test slices that contain special resins and features like bark, knots, or resin pockets. Using the weight of the test slice before the test and after being oven-dried, the MC % can be calculated using the formula 2.7.

$$MC\% = \frac{Weight_{test} - Weight_{ovendry}}{Weight_{ovendry}} * 100 \quad (2.7)$$

2.4. Numerical modelling

In order to study the uniaxial bending behaviour of any material, the stress distribution along the depth of the beam over the cross-section has to be studied in detail. The distribution is dependent directly on the tensile and compressive behaviour of the material (Turnbull & Crocker, 2014). The anisotropy of natural wood can result in several failure modes, unlike steel or concrete where a single criterion is adequate to define material failure at least under specific support and loading conditions. The behaviour of wood especially as a material used for sheet-piles, according to Van de Kuilen & Van Der Linden (1999), can be modelled with distinct compressive and tensile strengths, plasticity, softening as well as a cracking criterion, all of these defined orthotopically.

Tresca and Von Mises criteria are the simplest concepts that can describe the plasticity of simple isotropic materials. Extensions of these yielding conditions were developed by Hill (1948) specifically for orthotropic materials and this condition was further modified by Hoffman (1967) by describing different yield strengths in tension and compression. In essence, Hill's criterion can be considered to be a generalization of the Von-Mises criterion to account for the material's anisotropic plasticity (Xu et al., 2009).

2.4.1. Material model

Van de Kuilen & Van Der Linden (1999) used the Hoffman yield criterion in combination with a crack criterion, assuming that the tensile and compression strengths are identical in both directions perpendicular to the grain. It was feasible to model distinct compression and tensile strength values along the grain using this supposition. The Hoffman yield criterion resulted in overestimation of the uniaxial strengths when these specific criteria were not taken into account (Van der Linden et al., 1994).

The use of Hill's criterion to model the anisotropic bending behaviour of timber is supported by multiple other pieces of literature. To numerically model the role of shear stress in the bending strength of clear wood specimens, Kocazan et al. (2017) tested the feasibility of multiple failure criteria. Hill's criterion proved to be suitable for the case of bending. In the numerical modelling to verify the experimental tests to assess dowel-type timber joints, even though Hill's criterion overestimated the modulus of elasticity of the specimens (Xu et al., 2012), the modified Hill-Hoffman criterion proved to be feasible, especially to take into account the compressive stress distribution.

2.4.2. Load sharing

Load sharing factor can be defined as the ratio of the characteristic bending strength of a set of specimens to the characteristic bending strength of the combined system made by joining the specimens

together (Van de Kuilen & Van Der Linden, 1999). The load-sharing factor boosts the specimen's design strength by accounting for two effects: first, the decreased likelihood that a weaker member or part will be positioned where the stresses are particularly great; and second, the positive connection between strength and member stiffness. This positive correlation enables a stiffer member to carry a higher proportion of the applied load. When compared to concentrated loads, for uniformly loaded systems, the load-sharing effect is less evident.

To study the load sharing factor, in Van de Kuilen & Van Der Linden (1994),(1996) carried out an experimental sheet-pile wall test followed by a numerical analysis that involved a Monte Carlo analysis to find the characteristic load sharing factor.

2.4.3. Timber in DIANA

The three characteristics required for timber to be modelled numerically are its stiffness in the elastic region, yielding strengths in tension and compression along the respective orthotropic directions, and tension softening curve (Van de Kuilen & Van Der Linden, 1999). Although not specifically for timber, the FEA software DIANA offers a range of material models with orthotropic plastic and softening attributes (Ferreira & Manie, 2022). To model the orthotropic plasticity, the available models in DIANA 10.5 are Hill anisotropy with anisotropic yielding that is equivalent to the modified Hill-Hoffman criterion and Rankine-Hill anisotropy which is based on multisurface plasticity and combines the anisotropic Hill criterion for compression with Rankine's yield criterion.

2.5. Summary

Decay in hardwood is an inevitable process, and the causes can vary hugely based on their application. In sheet-piles, the hardwood used undergoes decay to a different extent at different zones along their length. This extent of decay can systematically be studied based on how they affect the mechanical strength by several methods that can leave the specimen that is being tested completely or partially usable or unusable. Non-destructive tests have multiple advantages and are relatively easier to perform on the sheet-piles compared to destructive ones. It is possible to establish the relationship between these destructive and non-destructive tests. Most of these tests need to be performed by following the guideline provided in the NENs and since the sheet-piles have already been in service, relevant literature that supports the usage of alternative methods can also be relied upon. For visually analysing timber that have been in service, although Ceccotti & Togni's (1996) work on the visual decay analysis provide a basis on how detailed the analysis can be performed, to understand, other X-ray and CT tests provide a detailed 3 dimensional map which is more accurate, although the latter being time-intensive in comparison with the former. The results from these tests can be analysed to form a basis for performing numerical analysis. It is possible to accurately predict the load-sharing factor of hardwood sheet-piles through numerical methods by performing a Monte Carlo simulation.

Experimental analysis - Method

This chapter describes the experimental aspects and the details of the destructive, non-destructive and semi-destructive tests, in the sequential order in which they were performed. Azobé (hardwood) sheet-piles that were in service since 1966 were tested and several experiments were performed on them to acquire data on their physical and mechanical properties. The detailed process involved in the conversion of the data obtained from the experimental tests into analysable results is also presented along with the possible analysis methods that can be employed.

3.1. Experiment outline

Based on the sets of experimental tests explored from the literature, suitable methods that can assess the reusability of the sheet-piles by providing as detailed information about the wood as possible were chosen and sequentially performed as shown in figure 3.1. The experimental process can broadly be split into three major parts: setting up and preparing the sheet-piles for the experiments to be performed on, non-destructive and semi-destructive tests, and destructive tests.

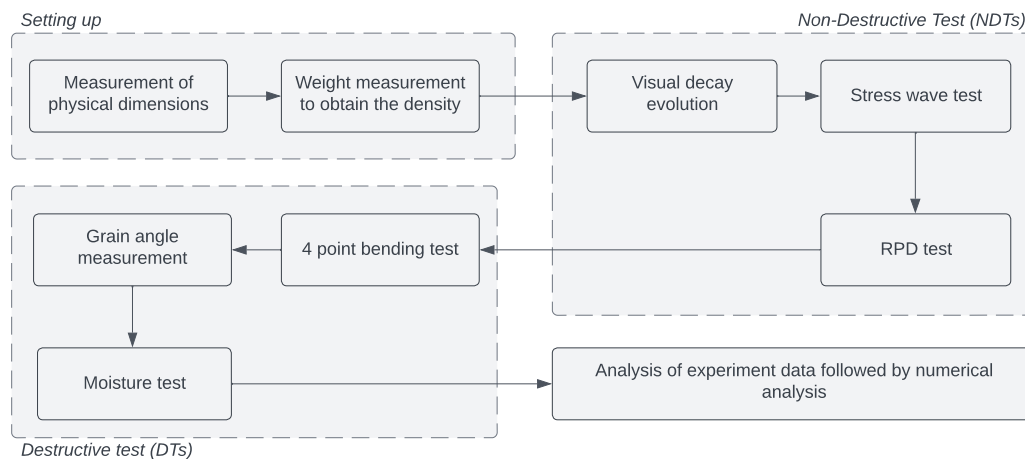


Figure 3.1: Flowchart of the experimental testing process

3.2. Material and setup

3.2.1. Cutting and pretreatment of sheet-piles

The sheet-piles obtained from the site were approximately 2.6 m long with varying widths and had been in service since 1966. A simplified interpretation of how the sheet-piles in-service support the active and passive parts of the soil is shown in figure 3.2. In order to subject different zones of the sheet-pile

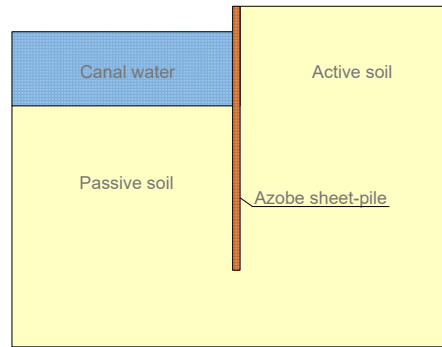


Figure 3.2: Schematic representation of the sheet-pile wall on site

to different bending configurations, which alternatively induced tensile and compressive stresses on the two sides of the sheet-piles that were exposed to the active soil and water along with passive soil, they were cut into two approximately 1m long boards while the end pieces were discarded as represented in figure 3.3. These configurations are explained in detail in section 3.6.2 The top part of the sheet-pile was named after the Province North Holland as PNH X -0 and generally referred to as the top board, while the bottom part of the same sheet-pile was named PNH X -1 and referred to as the bottom board. As shown in figure 3.4, each board consisted of two contrast-looking flat surfaces: one that was facing the canal along with the passive soil, hence looking relatively smooth and was termed as the water-side (W side) and the other that was directly in contact with the active soil, possessing decayed patterns throughout, was termed as the earth side (E side).

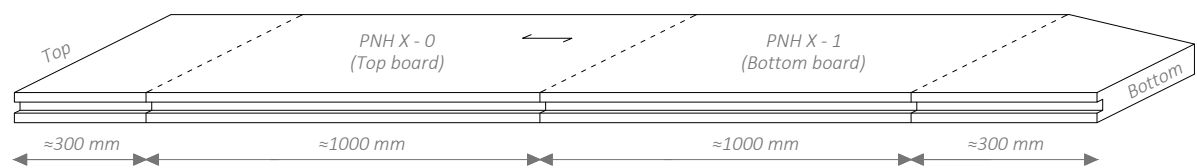


Figure 3.3: Azobé sheet-pile as taken out from the soil



(a)



(b)

Figure 3.4: Typical W (a) and E (b) sides of the tested boards

When the sheet-piles were subjected to loading on site, 95% of their length was immersed below the groundwater table and hence the Moisture Content percentage (MC%) in the wood was expected to always stay above the fibre saturation point. However, large structural timbers typically have MC

that varies depending on the element's length and cross-section. The MC of the sheet-pile in use, when partially exposed to air, was a parameter that varied over time because the moisture in the wood always tried to attain equilibrium with the relative humidity of the air around it. Changes were expected to happen in response to seasonal and daily change (Riggio et al., 2014). The top and bottom boards of the sheet-piles were soaked in water for at least ten days before they were tested. This way, the boards were expected to have MC above their fibre saturation point since that would be representative of the moisture condition that the sheet-piles were in on-site. The water that was used to soak the boards in was mixed with cleaning vinegar (6% Acetic acid) to bring the pH level of the water down to ≈ 3.5 . Hardwood's mechanical behaviour is unaffected under acidic environments (Bongers & Beckers, 2003), and this acidic level ensured no growth or presence of *Legionella pneumophila* and *Salmonella* bacteria that could have caused any health hazards in the working environment.

3.2.2. Weights and dimensions

To calculate the density of the boards, including their own moisture content, the soaked sheets were taken out from the water tank and kept aside until the excess water completely stopped dripping from the boards surface. The board was then weighed using a scale whose least count was 5 g.

The physical dimensions: Length (L), Width (B), were measured with an accuracy of 0.5 mm and Thickness (T) with an accuracy of 0.1 mm. The length of the board was measured using a tape measure along two locations: the left and right sides of the W face of the board, and the width was measured along three locations: top, middle, and bottom of the board. The width of the board was measured on the W face of the board and includes the width of the groove and did not include that of the tongue as shown in figure 3.5. Not much variation was noticed between the length and width values recorded at the above-mentioned locations for each board. However, the thickness was measured at three locations: top, middle, and bottom of the board using a digital vernier caliper with a least count of 0.1 mm, and in some of the boards, a significant difference between values from different locations of the same board was observed. The density was calculated using the physical dimensions and the weight of the board. It is important to note that this value of density (ρ or ρ_{wet}) is calculated using the weight measured during the testing process of each board.

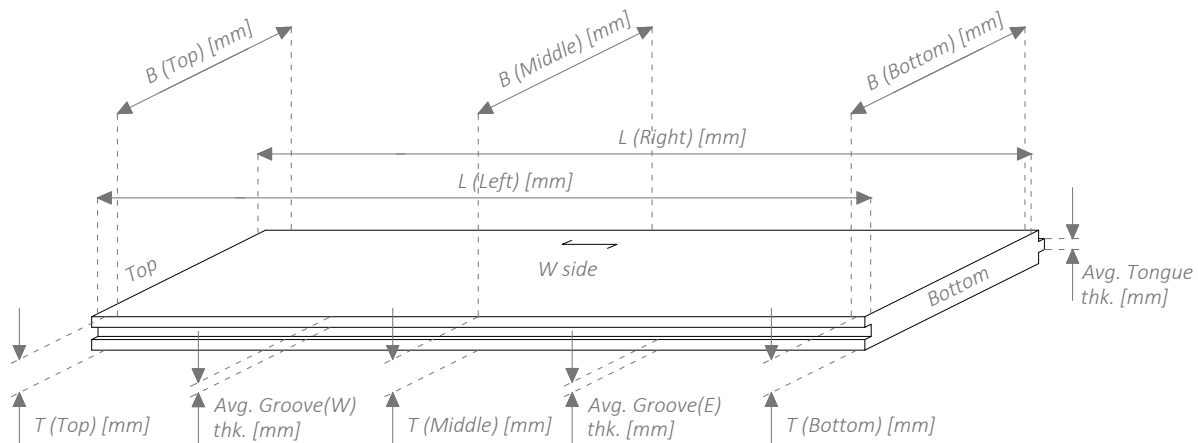


Figure 3.5: Measurement location of the boards' physical dimensions

Owing to the decay stripes on the E face, the thickness was measured from the general outer surface that included the depth of the decay stripes as well, as shown in the figure 3.6. When the volume was calculated using such a thickness measurement, the volume was overestimated compared to the actual value, which has been discussed in section 4.7.

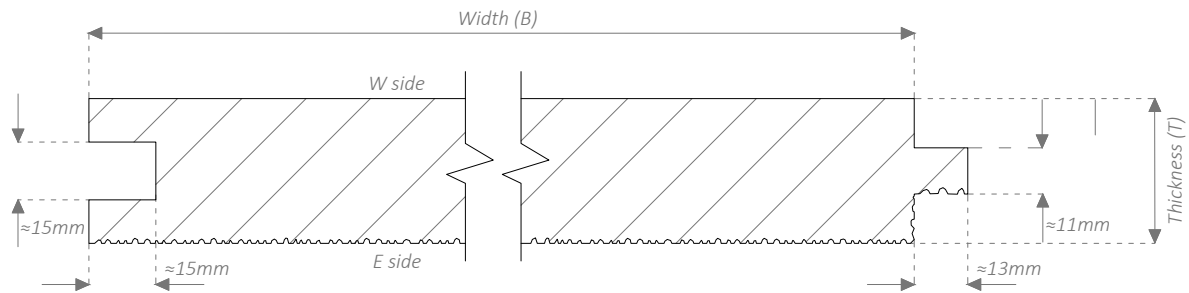


Figure 3.6: Typical cross-section of the timber board

3.3. Visual evaluation

3.3.1. Identification of visual characteristics

To simplify the process of assessing the reusability of the boards, they can visually be characterized and sorted, and this data can later be checked for correlation with the actual physical and mechanical characteristics obtained from testing the boards. The method used by Ceccotti & Togni (Ceccotti & Togni, 1996) was adapted for the evaluation of decay only at the superficial level. Though a detailed chart using CAD was not created, the distribution of different types of decay was plotted by hand in the data entry sheet, which would decide the score awarded to each board. The boards were individually closely inspected for visual characteristics like knots, splitting of fibres or visible decay. Since almost all the boards have undergone decay, but to varying degrees, the level of degradation is taken note of. Based on all the 152 boards that were tested, all types of decay that can occur in a board (figure 3.7) are: surface-level decay that can appear as varying levels of stripes, decay holes on the board's surface that can span partially or completely through the thickness of the board, reduction in thickness and brittling of the projecting edges (tongue and groove). Based on the size and type of these visual decay characteristics, each board can be assigned a visual evaluation score and such a score can be compared with other numerical data that represent the boards strength.

Being hardwoods, knots were rarely observed in the boards, and splitting of the board or just the fibres could be a common phenomenon that occurred due to uneven moisture levels within their length or due to the boards having been repetitively exposed to alternating wet and dry conditions during transportation, storage and preparation for the experiment. However since this splitting occurred only at the ends of the board, they were included in the span of the bending test and hence their effect on the mechanical strength reduction was considered to be negligible. Meanwhile, with respect to the decay of the wood that could be identified visually, decay stripes were prominently noticed on the E face of all the boards as shown in figure 3.7b, the groove could be disintegrated or brittle towards the E side of the board (figure 3.7d), the tongue could be reduced in thickness along its side due to decay and could also be brittle (figure 3.7e), or decay holes that partially or completely pass through the boards could be visible on the E side (figure 3.7c). Regarding the decay stripes, based on the width and depth of the stripes measured as shown in figure 3.8, they were classified into shallow, medium deep, and deep decay stripes with specifications as shown in table 3.1.

Table 3.1: Specification of different levels of decay stripes

Decay Stripes type	Shallow	Medium	Deep
Depth [mm]	<1.3	1.3–2	>2
Width [mm]	<2	2–4	>4



Figure 3.7: Types of decay at different locations on each board (a) W side (b) E side: striped decay (c)E side: decay holes (d) E side: thickness wise decay of the groove (e) E side: thickness wise decay of the tongue



Figure 3.8: Decay stripes and their physical attributes

3.3.2. Visual Decay Score (VDS)

Deciding the VDS for each of the boards was done based on four different parameters: the type of decay stripes present, distribution of these decay stripes, presence and type of decay holes, and level of decay in the tongues and grooves of the boards. Table 3.2 explains the criteria that had to be met by each of the boards to fall under a visual decay score category. Especially for the level of decay in the tongues and grooves, their brittleness needed to be noted in addition to the thickness left after decay.

Table 3.2: Parameters that determine the VDS of tested boards

VDS	Decay stripes-depth	Striped decay distribution	Decay holes	Tongue/ Groove condition
1	Shallow or Medium	Sparse 25-75%	None	Intact
2	Medium & Deep	50% - 75% 25%	None	Groove slightly decayed but still retains its thickness
3	Medium or Deep	Throughout 50-75%	Few shallow holes	Groove along the E side decayed to 50% of its original thickness but still intact
4	Deep	50-75%	Multiple hole that even go through the thickness	Groove decayed and chipped away/ extremely thin and brittle

3.4. Stress-wave test

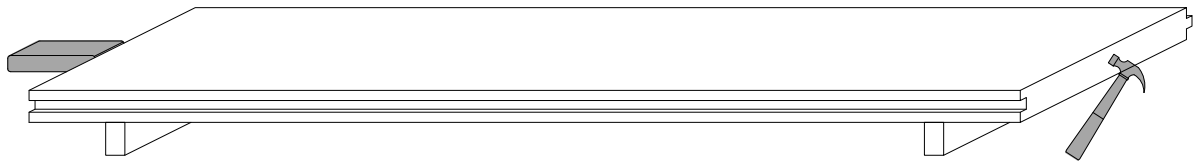


Figure 3.9: Stress wave test setup

According to Dackermann et al., (2014), the speed of sound along the grains corresponds to about one-fifth to one-third of the speed across the grain. Tests were performed along the grain in the longitudinal direction to understand the local bending behaviour of the boards, while tests across the grain were usually performed to find local flaws in the timber and were irrelevant in this case. Owing to the working conditions in the laboratory, acoustic tests requiring multiple accelerometers and a separate electronic device and impact hammer and one that requires minor drilling to insert the sensors were neglected, and eventually, stress wave tests using an electronic device with a built-in accelerometer became the optimal choice. The dynamic modulus of elasticity (MOE_d) obtained from the stress wave test could be checked for correlation with the static modulus of elasticity (MOE_s) obtained from the four-point bending test.

3.4.1. Equipment

The testing kits consisted of an impact hammer and an electronic Timber grader MTG device manufactured by Brookhuis Micro-Electronics BV, and is built-in with an accelerometer to record the frequency of any stress wave that impacts the sensor. The electronic device was portable and battery-operated, like most commercial stress wave measurement kits. By tapping one end of the board with a steel hammer, a low-frequency impulse was generated that travelled through the timber. The accelerometer inside the electronic device measures the amplitude and the time of the wave that is caused by the striking hammer, and this amplitude vs time plot is then processed by First Fourier Transformation (FFT) to obtain an amplitude vs frequency plot. This plot was displayed in real-time during the test in the timber grader software application on a laptop that was wirelessly connected to the electronic testing device as shown in figure 3.11. Before commencing the testing process, pairing between the



Figure 3.10: Timber grader MTG equipment

testing device and the laptop with the software application was performed. The device automatically numbered consecutive readings that it captured successively. The frequency-time graph was checked for a clear peak representing the characteristic frequency of the material through which it travelled. If a clear peak was not obtained, multiple striking attempts were performed using the impact hammer until a clear peak was observed. Peak from the frequency-time graph was analyzed by the application, and the corresponding frequency value was automatically displayed as shown in figure 3.10.

The characteristic frequency of the board that was subjected to the stress-wave test was recorded in two ways: by taking note of the peak frequency value displayed in the timber grader software application as shown in figure 3.11 and by taking note of the beam number that was automatically generated by the electronic device. This beam number was later used to generate the same graph that the timber grader can generate, but with specific time-intervals to precisely extract the location of the peak in frequency using the timber analyzer software application as shown in the figure 3.12 and the peak frequency was then be taken note of.

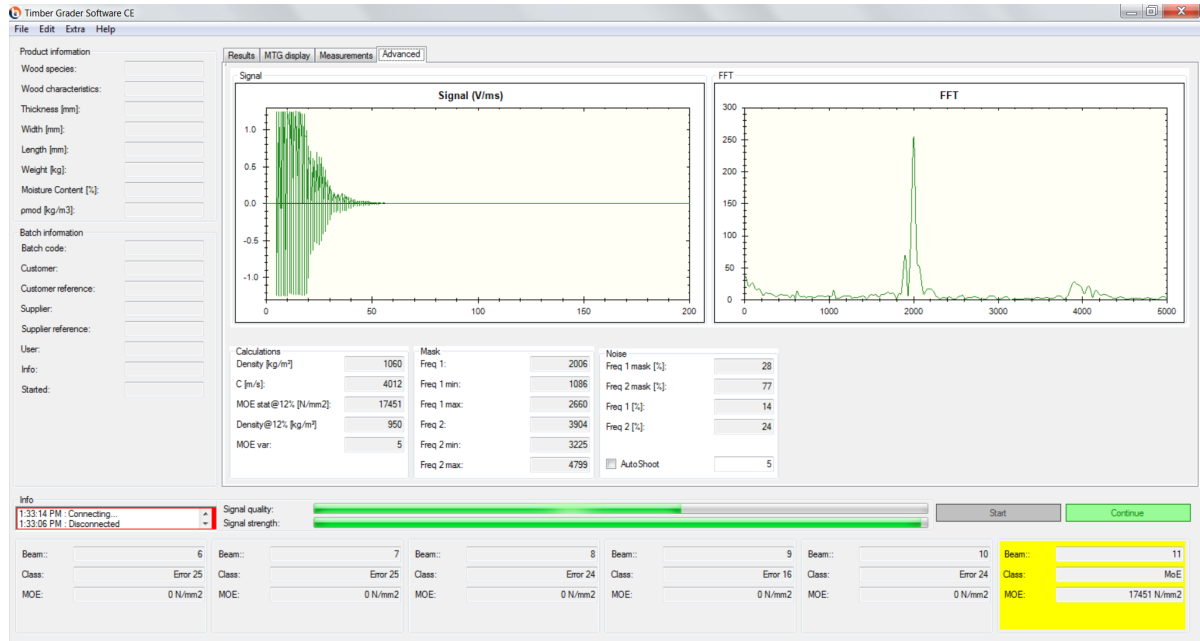


Figure 3.11: Screenshot of the MTG timber grader application during testing

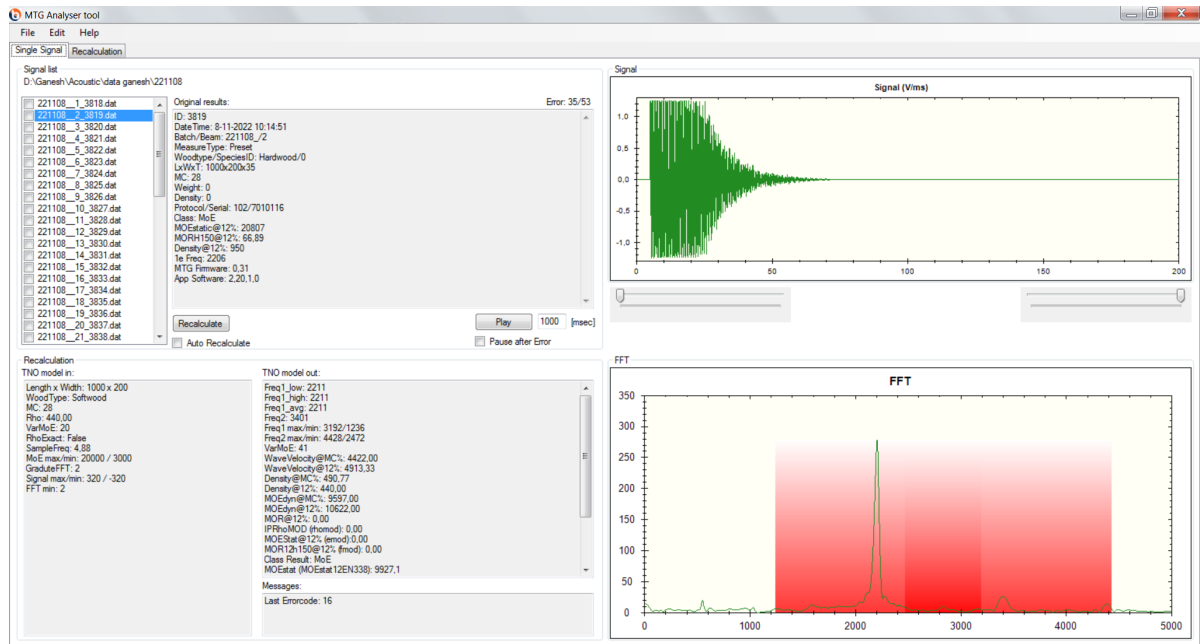


Figure 3.12: Screenshot of the MTG timber analyser application

3.4.2. Dynamic MOE calculation procedure

Based on empirical correlations between stress wave velocities and timber density determined using the one-dimensional theory, the MOE_d at the wet condition of the boards was calculated using the formula 2.2, and this could be useful in predicting actual mechanical properties. For velocity calculation, since the stress wave was assumed to travel straight along the length of the board itself and then bounce back to be detected by the sensor, the distance travelled by the board was taken as two times the total length of the board. For L and ρ being the length and wet density of the board, respectively, f being the frequency of the stress wave created due to the impact, and V being the velocity of the propagating stress wave, an example of calculating MOE_d is shown in table 3.3.

Table 3.3: Dynamic MOE calculation example

Length	Frequency	Density	Velocity	Dynamic MOE
L	f	ρ	$V = 2Lf$	$MOE_d = V^2 \rho$
1001 mm	2069 Hz	1161.72 kgm ⁻³	4142.1 ms ⁻¹	19800 MPa

3.5. Resistance Penetration Drilling (RPD) test

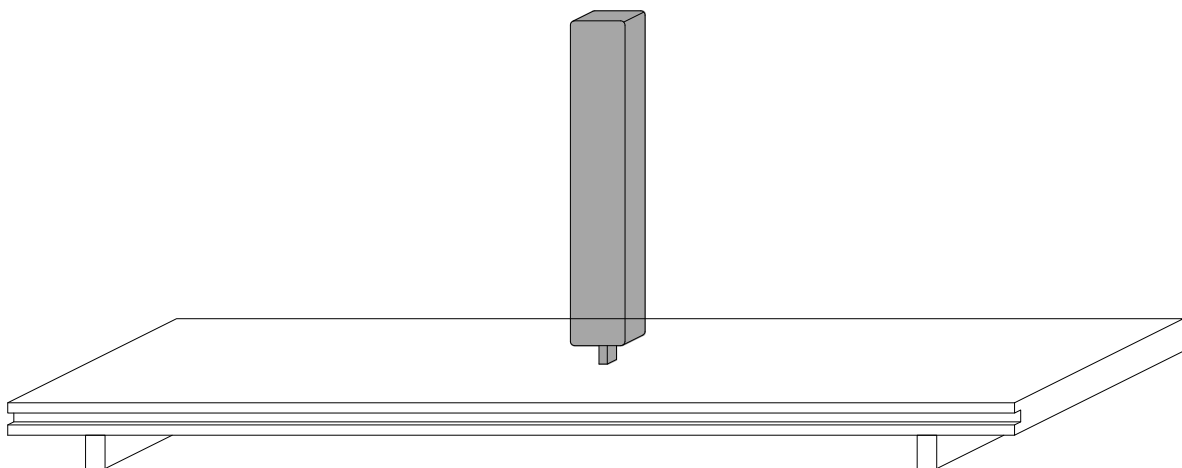


Figure 3.13: RPD test setup

The device used for RPD testing is the IML RESI PD-400, in which PD stands for Power Drill. The PD series performs simultaneous recording of drilling and the feed speed amplitudes, thereby efficiently detecting rots and local defects. At every 0.1 mm, the device records the measurement results as drilling and feed speed power-depth graphs, in which the drill and feed speed power are denoted in terms of their % amplitudes.

3.5.1. Input variables



Figure 3.14: IML RESI PD-400 RPD testing equipment

The drill needles must be thick enough to prevent deviations caused by the anatomical inhomogeneity of the Azobé boards yet small enough to capture tangential density differences and reduce damage to the inspected member. For dense tropical hardwood like Azobé, from Tannert et al., (2014), it was discovered that a 1.5 mm shaft diameter and a 3 mm tip were a good compromise that allowed users to drill through the dense wood material, without inflicting unacceptable harm to the sample. The device

had a feed speed range of 15 cm/min to 200cm/min and a drill speed range of 1500 r/min up to 5000 r/min. According to Gard et al., (2018), for unused Azobé piles of 300 mm x 300 mm cross-section, the optimal feed speed and drill speed were found to be 50cm/min and 5000 r/min respectively. In this case of used Azobé sheet-piles, since they are expected to be less dense compared to the unused ones and more localized flaws due to the decay and also aiming to eliminate the shaft friction as much as possible, the feed speed was chosen to be 25 cm/min while the drill speed was kept unchanged.

Table 3.4: RPD testing equipment – part and input specifications

Shaft diameter	Tip width	Feed speed	Drill speed
1.5 mm	3 mm	25 cmmin ⁻¹	5000 rmin ⁻¹



Figure 3.15: (a) Drilling head (b) Drill needle

3.5.2. Testing and processing of data

Experimental verification by Gard et al. (2018) showed that shaft friction that was caused due to the high density of Azobé hardwood played a dominant role in the displayed amplitude results in terms of both feed and drill speed. This suggested drilling of the hardwood boards preferably along the thickness. Also since the drilling direction or the side from which the drilling was begun played an important role, to obtain perceivable information about the boards with respect to their structural integrity, the boards had to be drill tested from either side of their thickness. Hence, to obtain reliable and detailed information from the boards, each one of them was drill tested at six locations as illustrated in figure 3.16.

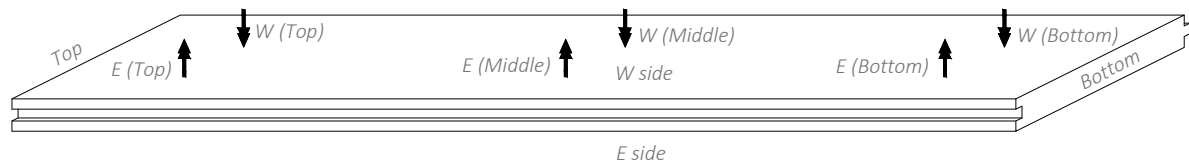


Figure 3.16: RPD test - drilling locations

The IML RESI PD-400 device that was used for testing recorded the amplitude percentage of feed and drilling speed at every 0.1mm. The thickness of the board at the location of drilling was calculated using the total count of these recordings. Based on the local thickness, the sequentially arranged feed and drilling amplitude data were tabulated against the total thickness percentage and then plotted. A typical graph with feed and drilling speed amplitude percentage plotted against the depth percentage at one of the drilling locations is shown in figure 3.17.

3.6.1. Test setup

To assess the strength of the boards by applying force on their flat surfaces and determining their beam properties in flatwise bending, a four-point bending setup as shown in figure 3.18 and 3.19a was designed. The setup consisted of two steel rollers of diameter 50mm placed at a centre-to-centre distance of 750 mm to support the Azobé board. The load cell that was capable of measuring the force applied during its vertical motion (F) in kN and was connected to a displacement sensor that records its vertical movement (S) in mm and branched from the centre of the beam span into two steel rollers of diameter 20 mm at a centre-to-centre distance of 256mm to load the Azobé board. Two lasers placed below the level of the supports at mid-span recorded the vertical displacement of the downward-facing surface of the board ($LS01$ and $LS02$) in mm. The entire setup was connected to a computer with a software application specially designed specifically to record all the measurement data (F , S , $LS01$ and $LS02$), and to simultaneously display the live values along with a basic force-displacement ($F - d$) graph as shown in figure 3.20. This data was later exported as *.dat* files with each boards data saved in a separate file. The option to modify the rate of displacement of the load cell was provided by the application through the interface shown in figure 3.19b.

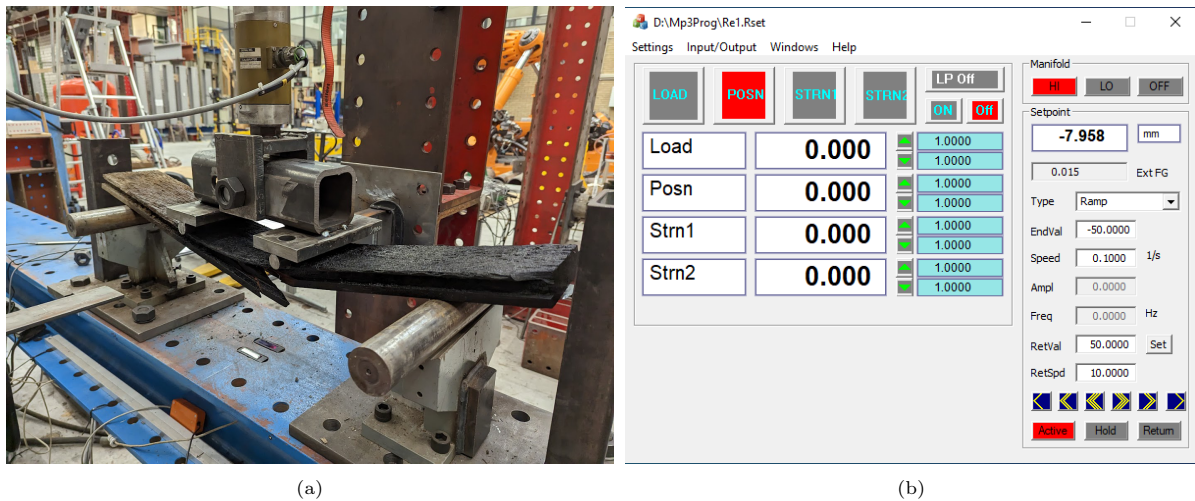


Figure 3.19: (a) Four-point bending test setup (b) Input interface of the testing application

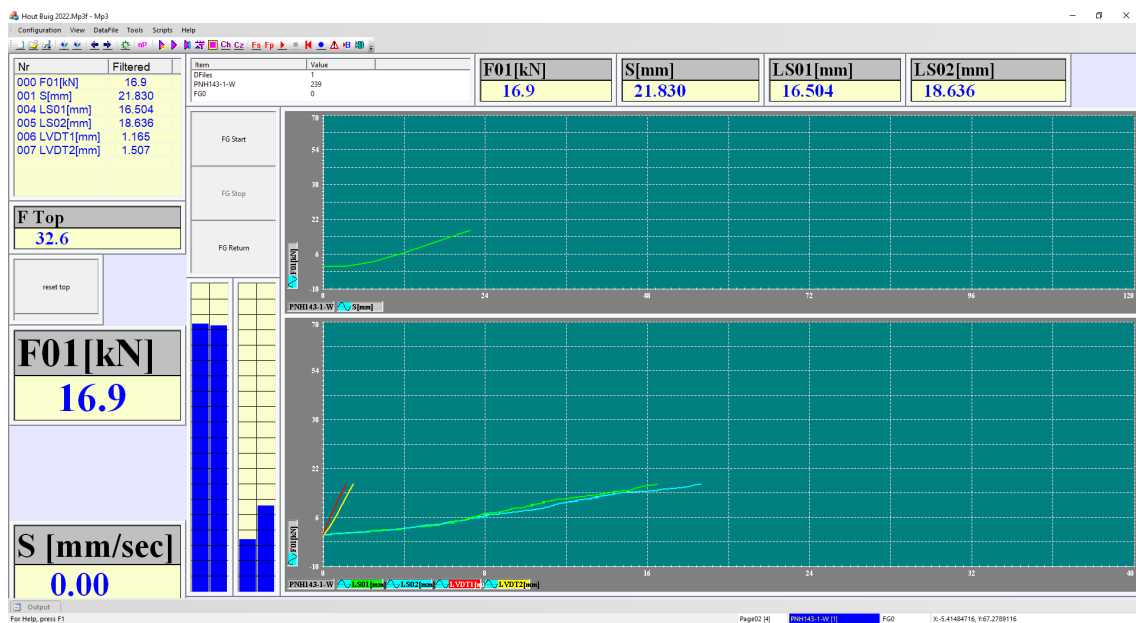


Figure 3.20: Output interface of the testing application

3.6.2. Configurations and testing process

Since every board had two distinctly looking faces (E & W), each set of top and bottom boards that form a single sheet-pile was four-point bending tested with one of the four configurations listed in table 3.5. When the sheet-piles are loaded on site, the top and bottom parts of the board may be subjected to different types of bending which causes tensile and compressive stresses on either its W or E side. By configuration testing an equal number of boards with each configuration, the effect of different bending patterns (figure 3.21) was analysed, with the aim to determine the weakest configuration. By differentiating sheet-piles with respect to their configurations and comparing their test results in section 4.5, the effect of such a testing method and the configurations was analyzed.

Table 3.5: Four-point bending test configuration of a set of boards from each Azobé sheet-pile

Configuration	I	II	III	IV
Top board vertically upwards side	W	W	E	E
Bottom board vertically upwards side	W	E	E	W

The wet Azobé board to be tested was placed on the support rollers while ensuring that the load cell was out of position and enough clearance was available. Then, the load cell along with its rollers was brought down to a position such that the loading rollers almost touched the Azobé board, but the F value remained to be zero. The displacement values that are being recorded (S , $LS01$ and $LS02$) were manually set to zero and the recording and loading were turned on. In addition to displaying the live values of the force and displacements, the application also displayed the force-displacement graph as shown in figure 3.20. Loading was stopped when the load value reached its peak and then dropped back to approximately 50% of the peak value. The recording of the force and displacement data was also subsequently stopped. The load cell was lifted back to its original location and the tested board was removed from the setup.

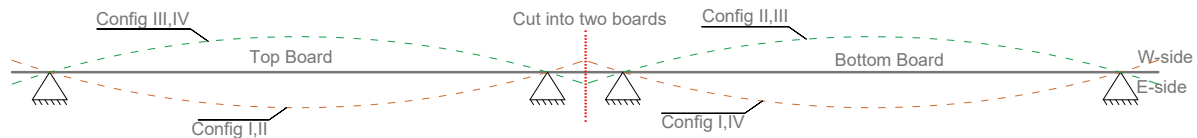


Figure 3.21: Types of bending caused due to testing the boards using different configurations

3.6.3. MOR calculation procedure

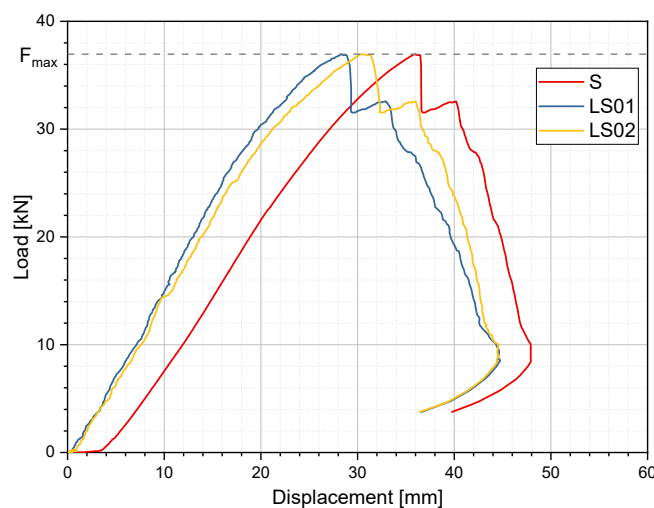


Figure 3.22: Typical force-displacement graph generated directly from the result data

Using the data obtained from the four-point bending test, for each board, a $F-d$ graph was generated as

shown in figure 3.17. From the data acquired, the bending strength of the Azobé board was calculated using the equation 3.2.

$$MOR = \frac{F_{max}ay}{2I} \quad (3.2)$$

where,

F_{max} is the maximum value of the force applied obtained from the result data as shown in figure 3.22; a is the centre-to-centre distance along the direction of the neutral axis of the board between one of the support rollers and the closest load roller;

y is the depth of the neutral axis of the board along its thickness from its farthest exterior surface;

I is the cross-sectional moment of inertia of the board with respect to the horizontal axis.

Table 3.6: MOR calculation example

Width	Thickness	Moment of Inertia	Max force	Support–Load distance	N.A depth	Bending Strength
B	T	$I = BT^3/12$	F_{max}	a	$y = T/2$	$MOR = F_{max}ay/2I$
186 mm	38.8 mm	9.0 E+5 mm ⁴	25.6 kN	245.5 mm	19.9 mm	65 MPa

3.6.4. Force-displacement graph data processing

To calculate the global static modulus of elasticity in bending (MOE_s), the force and displacement data that make the $F - d$ graph as shown in figure 3.22 was not directly usable due to local scattering occurring of the curves as shown in figure 3.23. This local scattering could be due to several reasons: the surface on which the lasers were pointed was not perfectly smooth especially when the boards were W-side-up tested, the friction that developed between the boards and either of the rollers (support or load) might have caused stuttery vertical movement of the boards along the vertical direction, resulting in the scatter. This problem was not solved at the experimental level and instead, a methodology was instituted to obtain the right slope values from the curves that possessed scatter. Since the data acquired consisted of readings recorded at fractionally small force and displacement intervals compared to the overall values, they needed to be checked for the scale of the local scattering, as this might affect the slope of the curves. Hence, the $F - d$ curves for $LS01$ and $LS02$ were checked for local scattering that could be detected visually in the graph. Figure 3.23 shows $F-d$ curves obtained from $LS01$ with and without local scattering. If case local scattering occurred, exponential smoothing was performed using a damping factor (α) such that in the elastic region of the curve, the slope of the longest range that visually looks straight with a slope variation of less than $\pm 5\%$ does not get altered by more than 5%. Figure 3.23a shows the elastic regime of an $F - d$ curve in which local scattering was evidently visible and was exponentially smoothed out with a damping factor of 0.1.

Once the visual local scattering was eliminated, based on the procedure given in NEN-EN 408 (2010), the $F - d$ curve between $0.1F_{max}$ and $0.4F_{max}$ were taken into consideration. The slope of the $F - d$ curves between this range were calculated and compared to each other if they agreed with how the curves visually compared with each other. If they agreed, the longest range in the LS -curves between $0.1F_{max}$ and $0.4F_{max}$ with a correlation coefficient greater than 0.99 was considered acceptable. The maximum and minimum values in such a range were taken as $F_1, S_1, LS01_1, LS02_1$ and $F_2, S_2, LS01_2, LS02_2$ values respectively. In case they did not agree, an alternative way to determine $S_1, S_2, LS01_1, LS01_2, LS02_1$ and $LS02_2$ was followed. In this method, the longest range in the elastic regime of the $LS01$ and $LS02$ curves in the $F - d$ graph that looked visually straight with an almost constant slope and was also representative of the slope between $0.1F_{max}$ and $0.4F_{max}$ was chosen, and each curves slope was determined. Within this range, it was also checked whether the correlation coefficient of the S -curve was greater than 0.99. If not, the chosen range is shortened until a correlation coefficient of 0.99 was achieved. The ratios of slopes of the LS -curves and the S -curve were determined for this range, and then the slope ratios along with the values of S at $0.1F_{max}$ and $0.4F_{max}$ (taken as the S_1 and S_2 values) were then used to calculate the $LS01_1, LS01_2, LS02_1$ and $LS02_2$. After determining these values, in order to double-check the processed result data, the region of the force-displacement curves considered

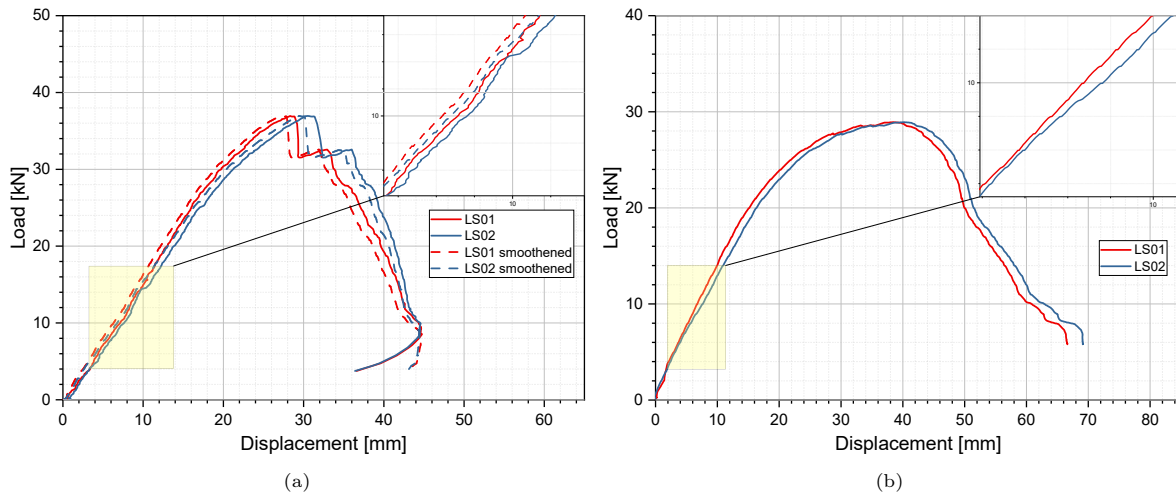


Figure 3.23: Typical force-displacement graphs (a) with local scattering and exponentially smoothed out (b) without local scattering

for the calculation was plotted in a separate graph. Their trendlines and corresponding equations were checked whether the ratio of the slopes of the former was in line with the Δ_w values (Δ_S , Δ_{LS01} and Δ_{LS02}). The complete procedure to obtain Δ_F and Δ_w (Δ_S , Δ_{LS01} and Δ_{LS02}) is sequentially represented as a flowchart in figure 3.24.

$$\Delta_F = F_2 - F_1 \quad (3.3)$$

$$\Delta_S = S_2 - S_1 \quad (3.4)$$

$$\Delta_{LS01} = LS01_2 - LS01_1 \quad (3.5)$$

$$\Delta_{LS02} = LS02_2 - LS02_1 \quad (3.6)$$

From the typical $f - d$ curves in figure 3.23, the LS01 has higher stiffness compared to that of LS02 and this pattern repeated itself for most of the boards. This could be due to the decayed part of the groove facing the E side contributing to lesser stiffness and hence the edge of the board with the tongue had higher stiffness, thereby resulting in a twist-like effect although not strikingly prominent because of the steel loading roller trying to stay in level and cancel it out.

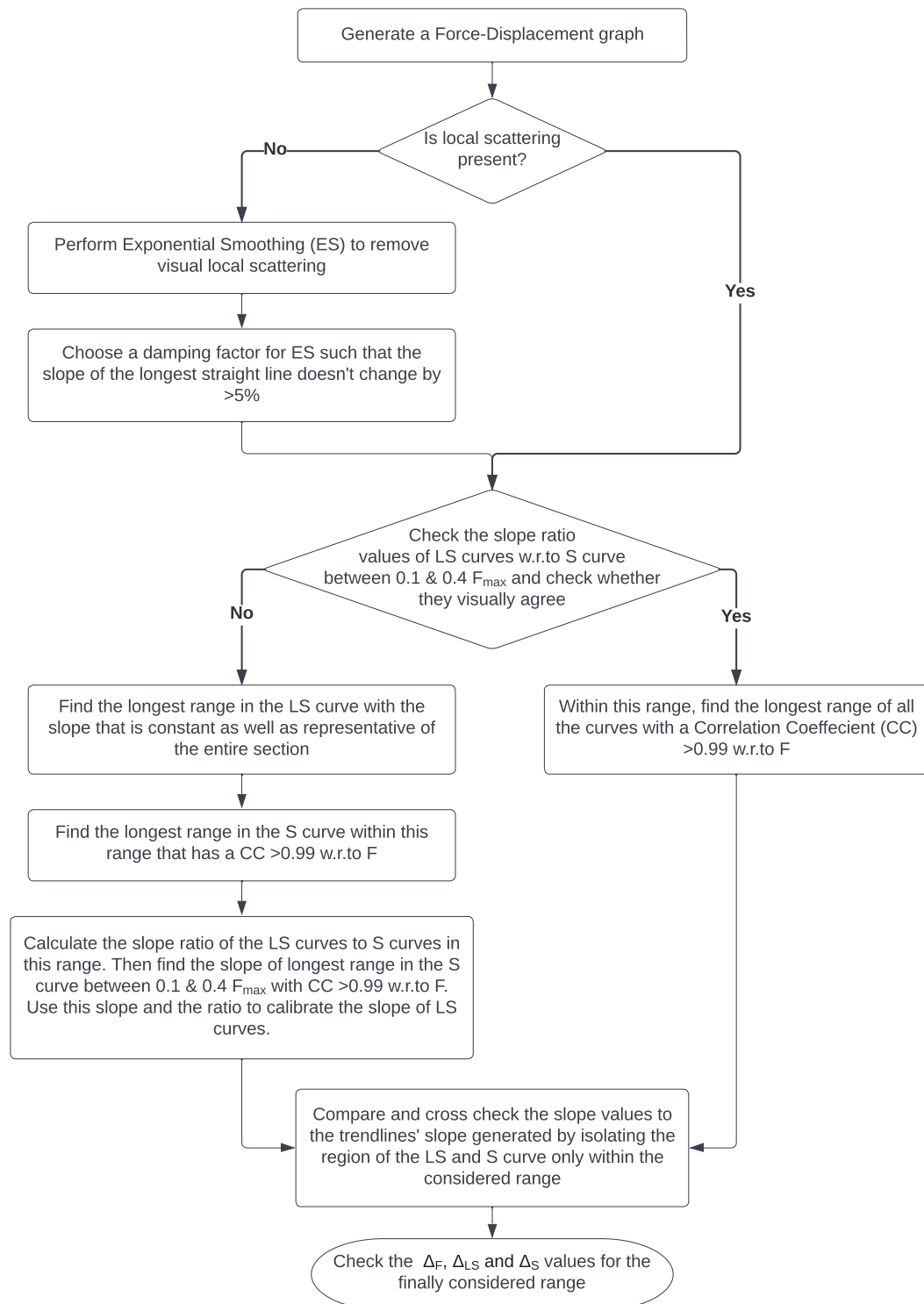


Figure 3.24: Processing the force-displacement data from experiments for $MOE_{s,1}$ calculation

3.6.5. Global static MOE calculation procedure

The value of $MOE_{s,g}$ was calculated for each of the displacement values, $w(S, LS01$ and $LS02)$ using the expression provided in NEN-EN 408 (2010) and modified as shown in equation 3.7. The final global static MOE ($MOE_{s,g}$) was calculated using equation 3.8 by calculating the mean of the stiffness values

from both lasers.

$$MOE_{s,g,w} = \frac{3al^2 - 4a^3}{2BT^3 \left(2 \frac{w_2 - w_1}{F_2 - F_1} - \frac{6a}{5GBT} \right)} \quad (3.7)$$

$$MOE_{s,g} = \text{Average}(MOE_{s,LS01}, MOE_{s,LS02}) \quad (3.8)$$

where,

F_2 , F_1 , w_2 and w_1 are obtained by processing the test data;

G is the shear modulus of the considered specimen and can be considered infinite when the above expression is used for strength class allocation procedure according to NEN-EN 384 (2022).

Table 3.7: $MOE_{s,global}$ calculation example

Δ_F	Δ_S	Δ_{LS01}	Δ_{LS02}	$MOE_{s,S}$	$MOE_{s,LS01}$	$MOE_{s,LS02}$
$F_2 - F_1$	$S_2 - S_1$	$LS01_2 - LS01_1$	$LS02_2 - LS02_1$	$MOE_{s,w} = \frac{3al^2 - 4a^3}{2BT^3 \left(2 \frac{w_2 - w_1}{F_2 - F_1} - \frac{6a}{5GBT} \right)}$		
10.7 kN	5.2 mm	4.00 mm	4.24 mm	11798 MPa	15373 MPa	14495 MPa

3.7. Local MOE

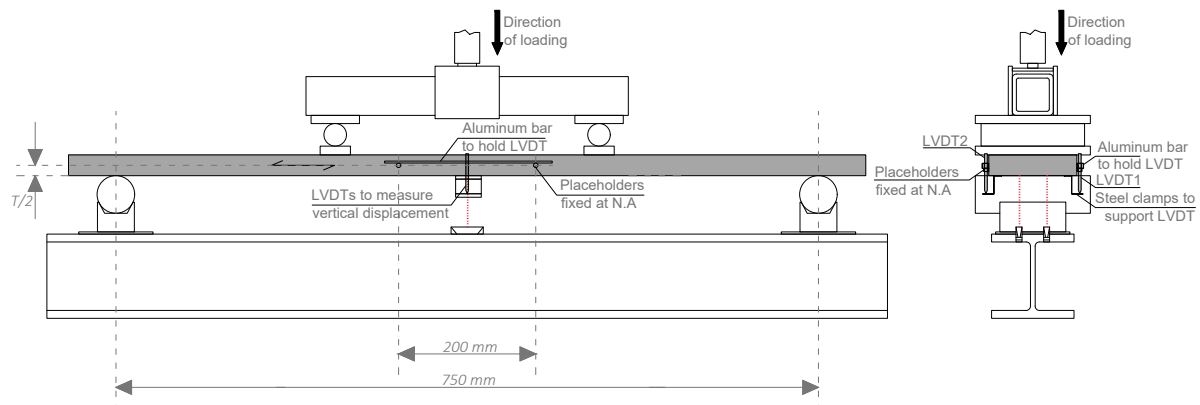


Figure 3.25: Local MOE testing setup

Though the global static MOE calculated using the setup as shown in figure 3.18 was sufficient in assessing the actual strength of each board, due to the decay during the service period, transportation and alternative dry and wet cycles that the boards go through, the boards' surface can be rough or the board itself could be geometrically irregular. This irregularity could cause discrepancies in the measurements recorded by the laser sensors. This error can be quantified and the measurements' correctness was cross-checked by calculating the local MOE which involved placing additional displacement measuring sensors that physically measure the displacement instead of using lasers. The local MOE mainly establishes the effect of the shear modulus G , which the global MOE does not take into consideration (G. Ravenshorst et al., 2014).

3.7.1. Test setup

The setup with which the four-point testing was performed was modified for the LVDTs to be placed at the mid-span so as to measure the vertical displacements between the span l_1 as shown in the figure 3.25. As specified in NEN-EN 408(2010) the central distance between the points of measurements of the displacement, l_1 had to be kept 5 times the thickness of the specimen tested and was taken as 200mm. The LVDTs were fitted into the slotted hole in an aluminium bar that spanned between this central span and relatively measured the displacement with respect to the bottom surface at the mid-span as shown in figures 3.25 and 3.26.

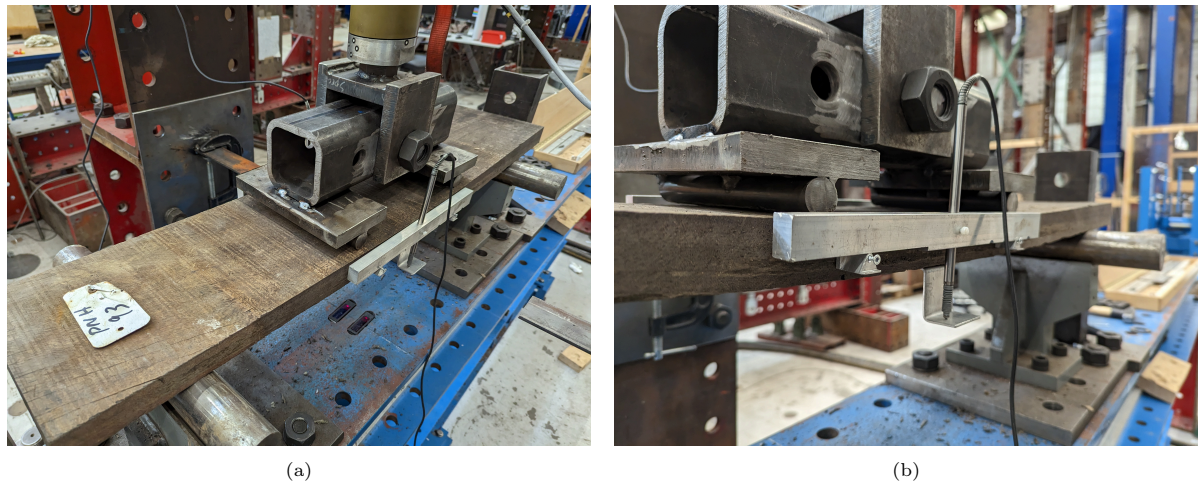


Figure 3.26: Test setup for the determination of Local static MOE

3.7.2. Local MOE calculation procedure

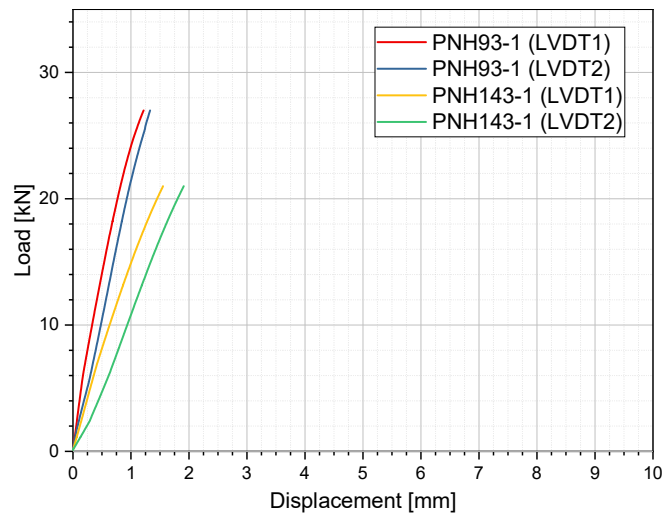


Figure 3.27: Typical force-displacement graph obtained from the local MOE data

In contrast with the force-displacement graph obtained from the lasers, the LVDTs generated a smooth-looking plot as shown in figure 3.27. This made the determination of the Δ_w with respect to the LVDT1 and LVDT2 much easier since the correlation coefficient was always much higher than 0.99 and almost equal one between the designated range of $0.1F_{max}$ and $0.4F_{max}$ part of the curve.

Based on NEN-EN 408 (2010), the value of $MOE_{s,l}$ was calculated for each set of the displacement values, w (LVDT1 and LVDT2) using the equation 3.9. The final $MOE_{s,l}$ was calculated as the mean of the value obtained from the two LVDTs.

$$MOE_{s,l,w} = \frac{al_1^2(F_2 - F_1)}{16I(w_2 - w_1)} \quad (3.9)$$

where,

F_2 , F_1 , w_2 and w_1 are obtained by processing the test data.

Table 3.8: $MOE_{s,local}$ calculation example

Δ_F	Δ_{LVDT1}	Δ_{LVDT2}	$MOE_{s,LVDT1}$	$MOE_{s,LVDT2}$	$MOE_{s,l}$
$F_2 - F_1$	$LVDT1_2 - LVDT1_1$	$LVDT2_2 - LVDT2_1$	$MOE_{s,w} = \frac{3al^2 - 4a^3}{2BT^3 \left(2 \frac{w_2 - w_1}{F_2 - F_1} - \frac{6a}{5GBT} \right)}$		Average
9.8 kN	0.52 mm	0.51 mm	11340 MPa	11600 MPa	11470 MPa

3.8. Grain deviation angle measurement



Figure 3.28: Fibre deviation angle measured on a bending tested board

The cracks and the failure patterns developed during the four-point bending test were measured for the grain angle slope. Since the boards were bend-tested flatwise, the grain angle deviation was measured on the tongue or groove side as shown in figure 3.28 using the angle measurement tool. The relation between the bending properties of the board and the measured grain angle deviation was checked for correlation in figure 4.13b.

3.9. Moisture test

3.9.1. Test setup

Figure 3.29: Moisture testing oven maintained at a temperature of 103°

After the grain angle was measured, each board was assessed to find a 40 to 80 mm strip that lay close to the crack/rupture formed due to the bending test and was made sure that the crack along the grains

did not pass internally through the strip. Each board was then marked for its strip, labelled, and then cut along the marking and across the thickness. Figure 3.30a is a typical strip cut from an ideal location of a board that had been subjected to all of the previously explained tests. The strips thus obtained were individually recorded for their mass with an accuracy of 0.1 g, and then placed in an oven that was maintained at a temperature of $(103\pm 2)^{\circ}\text{C}$. After approximately ten days, the strips were taken out and their weight was recorded and then placed back in their oven. Because the Azobé boards used in the experiment were soaked in water for enough days to reach their fibre saturation point, drying them to this extent caused evident cracking and chipping, turning them brittle. Hence some of the strips were not intact when they were taken out for weigh-ins. The parts that belonged to each strip were temporarily held together using a heat-resistant rubber band and then placed back in if additional weigh-ins were necessary. They were again checked for their weight after two hours and the difference percentage in their mass was calculated and checked if it was less than 0.1%. If not, the same procedure was followed until the difference in mass was less than 0.1%, and when the value was reached, drying was stopped and the final weight was taken note of.

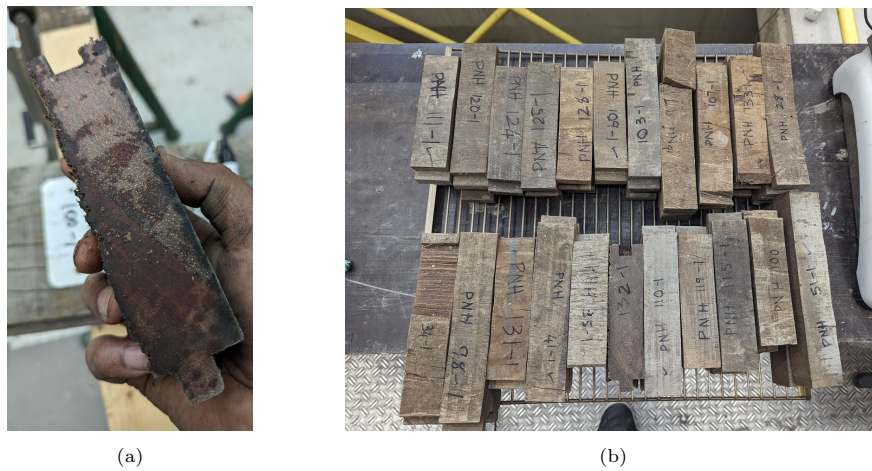


Figure 3.30: (a) Sample to be moisture tested cut from the board ready for the weigh-in (b) Moisture tested samples

3.9.2. Calculation procedure

Based on the formula provided in NEN-EN 13183-1 (2002), the *MC%* of each strip that was representative of the board itself was calculated using the formula 3.10.

$$\omega = \frac{m_1 - m_2}{m_2} * 100 \quad (3.10)$$

where,

ω is the *MC%* of the tested strip and hence the board itself;

m_1 is the mass of the strip before drying;

m_2 is the final mass of the strip after oven-drying.

Table 3.9: *MC%* calculation example

Weight before drying	Weight after drying	Moisture Content
m_1	m_2	$\omega = \frac{m_1 - m_2}{m_2} * 100$
344.0 g	237.9 g	44.6 %

3.10. Compression test

Out of the 152 boards that were tested through the sequence of tests mentioned above, for 20 boards, the cracked/ damaged part of the board or the ends where dry cracks had developed were neglected and

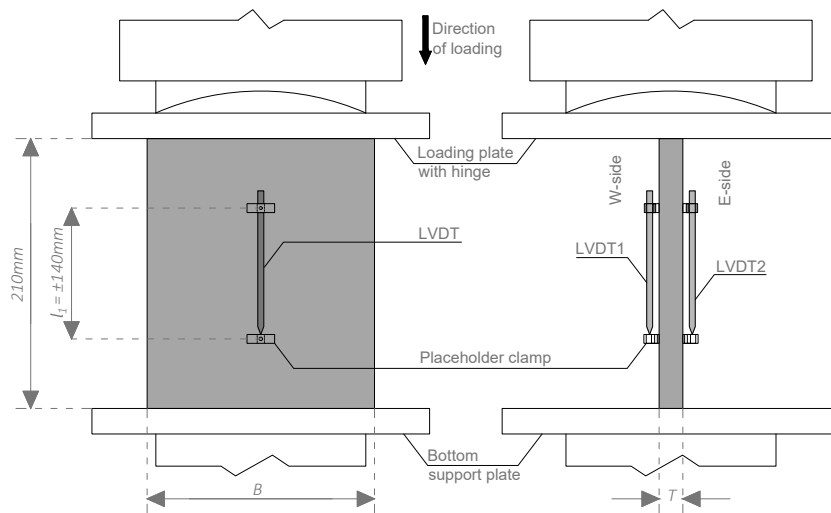


Figure 3.31: Schematic representation of the compression test setup

specimens that measured 210mm long which was approximately 6 times the smallest cross-sectional dimension were prepared for compression testing in a setup as shown in figure 3.31. According to NEN-EN 408 (2010), it was made sure the top and bottom edges were prepared to be parallel to each other.

3.10.1. Test setup

The test setup is shown in figure 3.32 and consisted of two flat square plates that were much larger compared to the cross-section of the specimens tested. The top plate was attached to a hinge which was in turn attached to a support beam while the bottom board was fixed to a loading cell. This ensured no additional bending is induced in the specimen. In addition to the vertical displacement measurements being recorded by the load cell based on its own movement, two LVDTs were placed on either surface of the specimen as shown in figure 3.32b. Each LVDT was fixed to the board using two brass clamps that were fixed to the specimen using screws at a distance of at least 140 mm. The loading rate was maintained at 0.01 mm/s according to NEN-EN 408 (2010). Essentially there were three displacement values being recorded for each specimen tested: the load cell's displacement (S) and the two LVDTs (L_1, L_2).



Figure 3.32: Compression test setup

3.10.2. Calculation of compression strength and MOE in compression

The data from the compression strength was observed to have no local scattering like that of global static MOE. This was expected during the test since LVDTs were used to measure the displacements in contrast to the laser sensors used in the four-point bending test. However, according to the $f-d$ curves, the portion of the curve between $0.1F_{max}$ and $0.4F_{max}$ is chosen such that the correlation coefficient is at least 0.99. Using this portion of the curve, the corresponding displacement values are chosen and then used for the calculation explained below. Based on the formula provided in NEN-EN 408 (2010), the compression strength and the modulus of elasticity in compression in the direction along the length of the board were calculated from the data obtained from the compression tests using the formulae 3.11 and 3.12.

$$f_c = \frac{F_{max}}{A} \quad (3.11)$$

$$MOE_c = \frac{l_1(F_2 - F_1)}{A(w_2 - w_1)} \quad (3.12)$$

where,

f_c is the compression strength of the specimen in the direction along its length;

F_{max} is the maximum value of the compressive force applied;

A is the cross-sectional area of the specimen;

l_1 is the gauge length as shown in figure 3.31;

$F_2 - F_1$ is the difference in the load in the selected portion of the $f-d$ curve;

$w_2 - w_1$ is the difference in the displacement in the selected portion of the $f-d$ curve.

Table 3.10: Compression strength and stiffness calculation example

F_{max}	A	Δ_F	Δ_{L1}	Δ_{L2}	f_c	$MOE_{c,L1}$	$MOE_{c,L2}$
	$B \cdot T$	$F_2 - F_1$	$L1_2 - L1_1$	$L2_2 - L2_1$	$f_c = \frac{F_{max}}{A}$	$MOE_c = \frac{l_1(F_2 - F_1)}{A(w_2 - w_1)}$	
377.7 kN	8288 mm ²	75.5 kN	0.08 mm	0.09 mm	46 MPa	13325 MPa	13383 MPa

4

Experimental analysis - Results and Discussion

This chapter discusses the results of the experimental tests in comparison with results from literature that are relevant to sheet-piles made of Azobé. The results obtained are also adjusted to the reference moisture content in the NENs which define the conditions and criteria for strength class allotment. The results are also analysed for their correlation with each other, especially between the destructive and non/semi-destructive tests. The impact of the four-point bend testing the boards with their two distinctly different-looking sides up or down is also analysed. The load-bearing properties of the set of boards that were initially cut from a single sheet-pile are analysed and compared to study and difference in the impact of different levels of decay along the length of the sheet-pile. The influence of the non-symmetrical decay with respect to the cross-section of the wood and the variation in thickness along the length of the board due to decay is also discussed. All the analysis and comparison also include a discussion of the limitations/shortcomings of the test involved or the parameters measured.

4.1. Overview of the results

The data obtained from various tests that were performed were collected, processed and then analyzed to understand the mechanical properties of the boards in the decayed state. A brief overview of the distribution of the result data is presented in tables 4.1 and 4.2. The distribution of data was segregated based on the four-point bending test configuration they were subjected to, followed by a summary of all four configurations presented with their average result values along with the covariances of each of the physical and mechanical properties. The relationship between the local and global MOE was found by plotting them and analysing their correlation as shown in figure 4.11. A factor of 1.16 was found as the ratio of the local to global static MOE for the 8 boards that were tested for their local MOE. The 12% MC density in the table 4.1 is the value calculated individually for each board as elaborated in section 4.1.1. For the calculation of the mean characteristic stiffness of each board, this factor 1.16 was used for the conversion from wet global to local static MOE.

Table 4.1: Overview of the test results - 1

Config.	No.	Length		Width		Thickness		S/T	Density _{wet}		Density _{mc12%}	
		[mm]		[mm]		[mm]			[kg/m ³]		[kg/m ³]	
		Avg.	CV	Avg.	CV	Avg.	CV		Avg.	CV	Avg.	CV
I	44	1000.7	0.6	194.6	21.3	37.1	4.5	20.1	1090	5.8	911	6.8
II	36	1000.9	0.6	189.5	20.3	36.8	4.1	20.3	1094	4.2	934	4.8
III	36	998.8	0.9	192.6	22.1	36.6	3.7	20.4	1081	3.5	925	5.7
IV	36	1000.8	0.5	193.8	25.7	36.8	3.1	20.3	1096	4.1	927	7.2
Overall	152	1000.3	0.7	192.7	22.2	36.9	3.9	20.3	1090	4.5	924	6.2

VDS		MOE _d		RM		MOE _{s,g}		MOR		MC	
[-]		[MPa]		[%]		[MPa]		[MPa]		[%]	
Avg.	CV	Avg.	CV	Avg.	CV	Avg.	CV	Avg.	CV	Avg.	CV
2.19	40.5	16244	20.2	25.2	9.8	11306	23.5	77.7	20.6	40	18.9
2.19	40	17242	17.3	25.0	7.6	11693	19.4	79.7	21.0	37	17.5
2.25	44	16930	15.2	24.5	10.2	11563	18.4	81.4	20.4	37	20.2
2.31	34.1	16822	18.3	24.9	10.4	11411	23.1	76.7	23.0	38	21.5
2.26	37	16782	17.9	24.9	9.5	11483	21.2	78.8	21.1	38	19.7

All Coefficient of Variations (CV) have % as their unit

Table 4.2: Overview of the test results - 2

No.	MOE _{s,l}		No.	f _c		MOE _c	
	[MPa]			[MPa]		[MPa]	
	Avg.	CV		Avg.	CV	Avg.	CV
8	11752	22.4	20	46	21.4	13272	26.4

All Coefficient of Variations (CV) have % as their unit

4.1.1. Strength class allocation

A reference moisture content of 12% and a reference height of 150 mm are utilised for the strength classes specified in NEN-EN 338 (2016). The results obtained from the experimental tests must be adjusted to reflect these reference values. According to Ravenshorst (2015), the MOE determined from the elastic range is not influenced by the size effect based on the Weibull theory. For the adjustment of density, MOE and bending strength, the equations formulated by Ravenshorst (2015) were adopted and used. The adjustment factors used in Ravenshorst's conversion process were obtained by generalising the tests performed on multiple species with different dimensions and in the calculation performed in this thesis, these same adjustment factors were used. The equations 4.1, 4.2 and 4.3 were used to adjust the density, MOE and stiffness to their 12% values respectively. The value of volume change coefficient β takes into consideration the effect of radial, tangential and longitudinal shrinkage and a species-independent average value of 0.5 was used.

$$\rho_{mc12\%} = \rho_{wet} \frac{1 + 0.01\beta_v (MC_{25} - MC_{12})}{1 + 0.01 (MC_{wet} - MC_{12})} \quad (4.1)$$

$$MOE_{mc12\%} = \frac{MOE_{wet}}{1 - k_{mc} \left(\frac{\min(MC_{wet}; 25) - 12}{13} \right)} \quad (4.2)$$

$$MOR_{mc12\%} = \frac{MOR_{wet}}{1 - k_{b,mc} \left(\frac{\min(MC_{wet};25)-12}{13} \right)} \quad (4.3)$$

where,

$\beta_v = 0.5$ is the percentage volume change per percentage MC;

$k_{mc} = 0.13$ is the 12% MC adjustment factor for MOE;

$k_{b,mc} = 0.15$ is the 12% MC adjustment factor for bending strength.

Table 4.3: Properties of the tested boards adjusted to 12% MC

	MOE _{dyn,mc12%} [MPa]	MOE _{s,g,mc12%} [MPa]	MOE _{s,l,mc12%} [MPa]	MOR _{mc12%} [MPa]	$\rho_{mc12\%}$ kg/m ³
Mean	19290	13200	15310	93	924
S.D	3446	2793	3240	20	58

In order to assign strength classes as per NEN-EN 338 (2016), it is assumed that all tested boards meet the requirements of NEN-EN 14081 (2019) and the characteristic values are calculated according to NEN-EN 14358 (2016). Once the mean and standard deviation for the adjusted density, strength and stiffness values (table 4.3) were calculated, the characteristic 5th percentile value, $m_{k,p}$ (parametric), $m_{k,np}$ (non-parametric) and the characteristic mean value, m_{mean} of each of these parameters were calculated according to NEN-EN 14538 (2016) by using the equations 4.5, 4.5 and 4.6. The characteristic values are calculated to give the 5th percentile lower tolerance limit with confidence, $\alpha = 75\%$. The characteristic mean value is calculated considering the effect of confidence intervals. The values of $k_s(n)$ and $k_{s,m}(n)$ for 152 boards that were tested account for 1.69 and 0.0544 respectively. The resulting characteristic values are presented in table 4.4. The tested sheet-pile boards fall under the hardwood strength class of D50 since their characteristic values of strength and density and the characteristic mean value of stiffness exceed the corresponding values of the strength class.

$$m_{k,p} = Mean - k_s(n) \cdot SD \quad (4.4)$$

$$m_{k,np} = y_{0.5} \left(1 - \frac{k_{0.5,0.75} CV}{\sqrt{n}} \right) \quad (4.5)$$

$$m_{mean} = Mean - k_{s,m}(n) \cdot SD \quad (4.6)$$

$$k_{0.5,0.75} = \frac{0.49n + 17}{0.28n + 7.1} \quad (4.7)$$

$$k_{s,m}(n) = \frac{0.78}{n^{0.53}} \quad (4.8)$$

where,

$y_{0.5}$ is the 5th percentile value obtain from the data set by interpolation;

$k_{0.5,0.75}$ is the multiplier for 5% tolerance limit with 75% confidence;

n is the number of result values;

CV is the coefficient of variation;

$k_s(n)$ is the 5th percentile conversion factor defined in NEN-EN 14538 (2016);

$k_{s,m}(n)$ is the mean conversion factor defined in NEN-EN 14538 (2016).

NEN 384 (2022) states that for timber beams subjected to a four-point bending test when the distance between the loading point and the closest support is different than 6 times the depth, the bending strength needs to be adjusted by dividing the factor k_l , whose formula is given in equation 4.9. The average value of k_l values to 0.98 and is almost equal to 1. Hence, in the current study, this effect is not considered which makes the calculated characteristic bending strength value more conservative by 2%. The standard also states that, for specimens with a depth less than 150 mm, the characteristic bending strength should be adjusted using the depth factor k_h which can be obtained using equation 4.10. The strength class of the sheet-piles drops to D45 due to the reduction in characteristic bending strength to a value of $f_{m,k}=47$ MPa, making it the governing strength parameter. However, it is also stated in NEN 384 (2022) that the maximum characteristic density needs to be 700 kg/m³ for the specimen

Table 4.4: Characteristic values of the sheet-piles and the strength class

	$f_{m,k}$		$E_{m,mean}$	$\rho_{m,k}$	
	$f_{m,k,p}$	$f_{m,k,np}$		$\rho_{k,p}$	$\rho_{k,np}$
Current study	60 MPa ¹	58 MPa ¹	15210 MPa	826 kg/m ³	815 kg/m ³
D50	50 MPa		14000 MPa	620 kg/m ³	
D45	45 MPa		13500 MPa	580 kg/m ³	

¹ Without applying depth and span correction

After applying depth and span correction, $f_{m,k,red}=47$ MPa

to experience the depth effect. Since the characteristic density of the decayed sheet-pile boards is 826 kg/m³, the non-reduced value of the characteristic bending strength is considered for strength class allocation.

$$k_l = \left(\frac{48h}{l + 5a} \right)^{0.2} \quad (4.9)$$

$$k_l = \left(\frac{48h}{l + 5a} \right)^{0.2} \quad (4.10)$$

where,

h is the depth of the beam;

l is the span of the four-point bending tested board;

a is the distance between one of the supports and the closest loading point.

4.1.2. Interpretation of the data

Table 4.5: Comparison with results from literature

Sample	No.	Width [mm]	Span [mm]	S/T [-]	MC ⁶ [%]	MOE _d [MPa]	MOE _{s,g} [MPa]	MOR [MPa]
PNH ¹	156	193	750	20.3	>FSP	16782	11483	78.8
V1 ²	39	300	5400	90	>FSP	17500	16300	78.5
N2 ³	40	150-176	750	25	>30	-	16450	104.8
O1 ³	15	118	1500	27	>30	-	19030	109.6
O2 ³	20	135-260	1500	30-25	>30	-	18490	109.4
O3 ³	22	153-283	1500	30	>30	-	17380	106.0
AZ1 ⁴	46	50	18±3h ⁵	18±3	>30	20700	17000	93.8
AZ2 ⁴	79	65	18±3h ⁵	18±3	>30	17700	13700	80.7
AZ3 ⁴	30	50	18±3h ⁵	18±3	>30	21200	18700	111.6

¹ Results of the current thesis

² Results from Van de Kuilen & Van Der Linden (1996) (1999)

³ Results from Van de Kuilen & Blass (2005)

⁴ Results from Ravenshorst (2015)

⁵ AZ1, AZ2 and AZ3 were tested edgewise with h value of 150, 150 and 110 mm respectively

⁶ The moisture content at which the sheet-pile was tested

In table 4.5, the results from the experiment are compared with relevant results from the literature pertaining to Azobé sheet-piles which were tested for their bending properties. The mean dynamic MOE value obtained from the experimental tests is equal to 96% of the dynamic MOE value obtained by Van de Kuilen & Van Der Linden (1999) for the individually flatwise bending tested samples, V1. This is in agreement with the factor of decrease of 95.5% with respect to the dynamic MOE of the Azobé samples used in Van de Kuilen & Blass (2005) that have not been mentioned in table 4.5, since

they were edge-wise tested. However, the global static MOE value compares to only 66% of the average global MOE of samples O1, O2 and O3 tested in Van de Kuilen & Blass (2005). This discrepancy between the decrease in dynamic and global static MOE was cross-checked by finding the local static MOE of a few boards. The findings confirmed the correctness of the global stiffness values and hence the discrepancy. The dynamic to global static MOE ratio of 1.46 is drastically different compared to the literature values that have a range of 1.03 to 1.29 for Azobé in general without considering the cross-section, span or boundary conditions range. This can be attributed to the difference in the method reported in calculating the global static MOE in the literature. In the four-point bending tests performed by Van de Kuilen & Blass (2005) the span-to-thickness (S/T) ratio is different compared to the thesis. The boundary conditions Van de Kuilen & Van Der Linden (Van de Kuilen & Van Der Linden, 1999) are such that the horizontal deflection of the sheet-piles is allowed to compensate for their vertical deflections of up to 1 m.

In the experiment conducted by Van de Kuilen & Van Der Linden (1999), the span-to-thickness ratio (S/T) was higher compared to the current study (table 4.5), resulting in much lesser bending strength. For sheet-piles with a comparable S/T ratio, the bending strength decrease of 26% was in relation to the 34% decrease in the static MOE, while not exactly the same. In the test performed by Van de Kuilen & Van Der Linden (1999), one of the supports was allowed for horizontal movement (which was usually 0.2 m max.) and this was to compensate for the high deflection at the mid-span (1 m), which could also be the reason for much lesser bending strength compared to the other samples from the literature.

The results from Ravenshorst (2015) while having been edgewise bending tested provide an overview of the range within which Azobé as a material can have its mechanical properties distributed. There is a difference in the relation of static and dynamic MOE compared to the literature and this can be pointed out towards the difference in the experimental setups. In conclusion, it is clear that the bending stiffness assessment cannot be based only on the results of the stress-wave test but still needs to be a combination of DTs and NDTs.

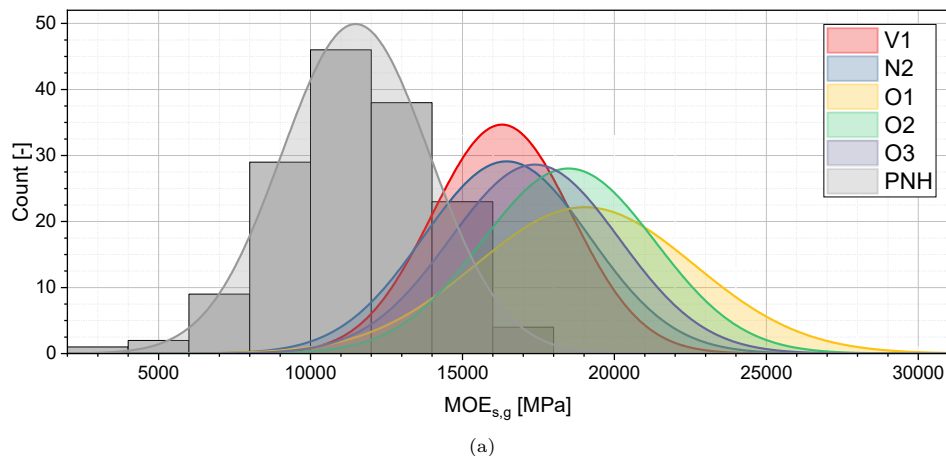


Figure 4.1: Distribution of the global static MOE in comparison to the literature

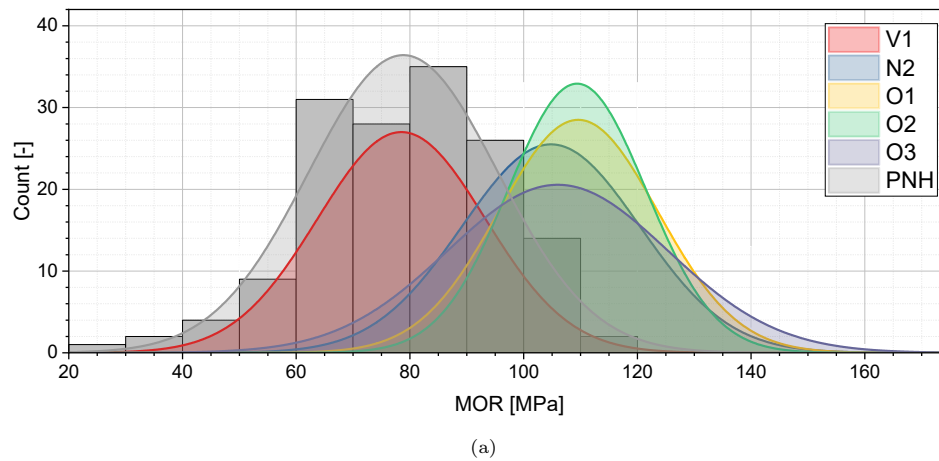


Figure 4.2: Distribution of the bending strength in comparison to the literature

4.2. Distribution of acquired data

All the result parameters obtained from the experimental tests are plotted as histograms to understand and analyze their distribution. Each histogram is tested for normality using the Shapiro-Wilk test (Shapiro & Wilk, 1965). The test involved checking if each sample came from a normal distribution and the null hypothesis is accepted for an alpha level of 0.05, below which the p-value should not lie for the dataset to be considered as normally distributed.

4.2.1. Dimensions and physical attributes

The distribution of the mean value of the physical dimensions such as the length, width and thickness calculated as shown in figure 3.6, is presented as histograms in figures 4.3a, 4.3b and 4.4a. The length of each board as shown in figure 3.3 is approximately equal to 1m, and the exact value is recorded and taken into account since it can play an important role in the calculation of MOE_d . From a larger set of available boards that were available for ease of handling, boards with lesser width were preferred, picked and then tested. The breadth distribution is shown in figure 4.3b and has concentrated towards the lower end. The p-value of the thickness is greater than 0.05 affirming its normal distribution.

The wet density of the boards, whose distribution is shown in figure 4.3c, has an average of 1090 kg/m^3 and is comparable due to the decay that the boards have undergone with the Azobé samples from Ravenshorst (2015) which had 1193 kg/m^3 and a decrease of 9.4% is observed in the sheet-piles under investigation. The wet density when adjusted to 12% based on the moisture content of the sliced samples has a distribution as shown in 4.3d with an average of 924 kg/m^3 . This value also has a similar relationship with the average 12% density for Azobé specimens used in Ravenshorst (2015) with 1019 kg/m^3 , which is a 10.3% decrease. No direct comparison of the density can be made with sheet-piles tested by Van de Kuilen and Blass (2005) since the data is not available when compared to the density of Azobé specimens that are not included in table 4.5, the 12% moisture content density appears to be much lesser than the average of 1129 kg/m^3 .

The tongues and grooves are composed of non-trapezoidal edges in cross-section. The dimensions of the tongue and grooves were observed to be in accordance with NEN 5493 (2010) for an average sheet-pile thickness of 36.9 mm. However several grooves that were facing the active part of the soil were as thin as 5mm and some of them were completely decayed or missing. It was also observed that the tongue was rectangular in shape and not trapezium and was on average more than 2 mm thinner compared to the gap between the groove which also complied with the specification stated by NEN 5493 (2010).

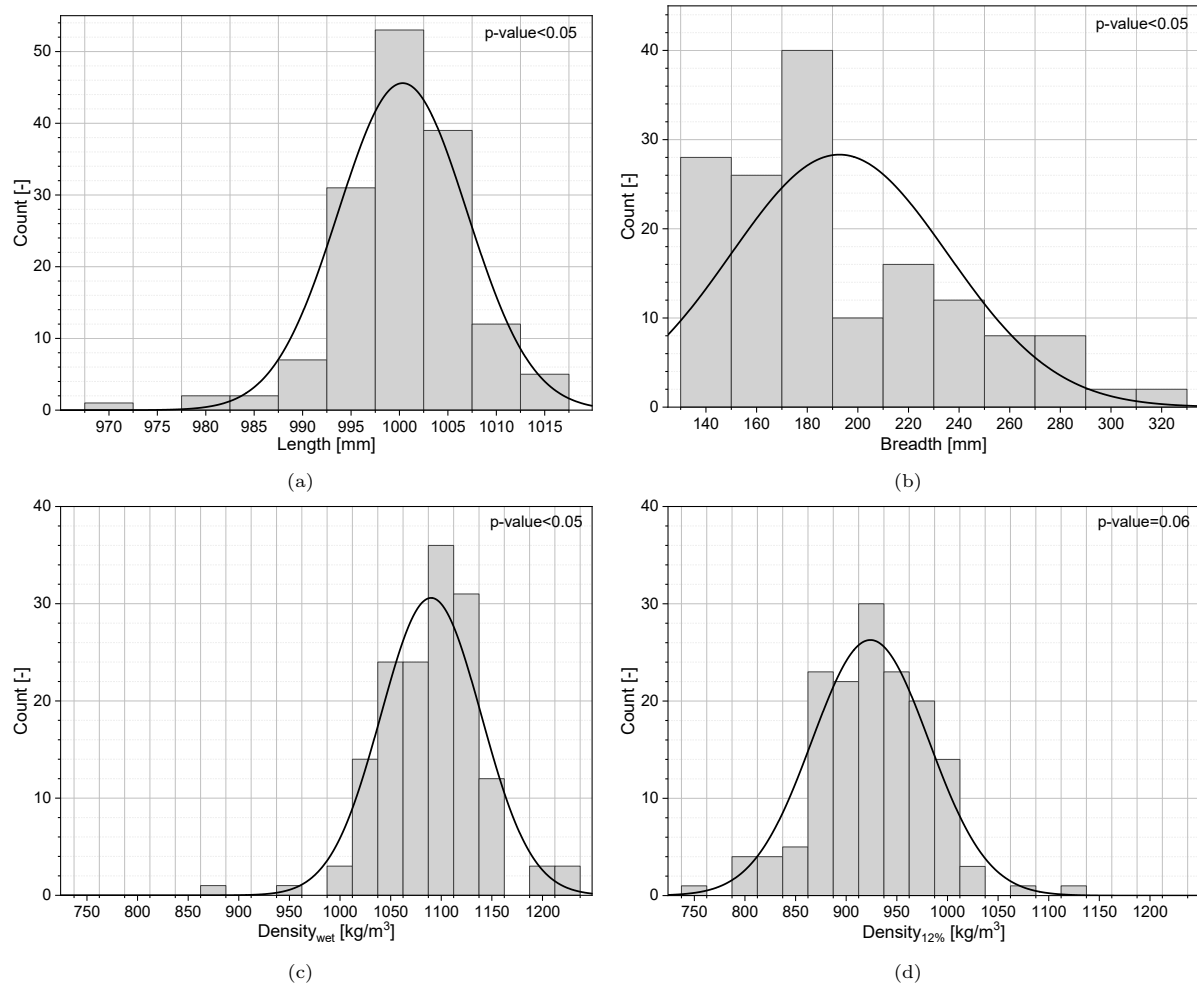


Figure 4.3: Histogram - (a) length, (b) width (c) wet density and (d) 12% MC density of the boards

4.2.2. Non-destructive test results

The distributions of the results from the non-destructive tests are shown in figure 4.4. A majority of the boards did not have decay holes, and even the ones that had did not have holes that passed through their full thickness, resulting in only 10 out of the 152 boards with a VDS of 4 (figure 4.4b). It is important to note that the distribution of MOE_d in figure 4.4c is calculated using the wet density and not the 12% density. All histograms except VDS in figure 4.4b have a $p\text{-value} > 0.05$ confirming their normal distribution. Although the VDS distribution has a $p\text{-value} < 0.05$, this is due to the values chosen for VDS allotment during the test, and they confirm with normal distribution as seen in figure 4.4b.

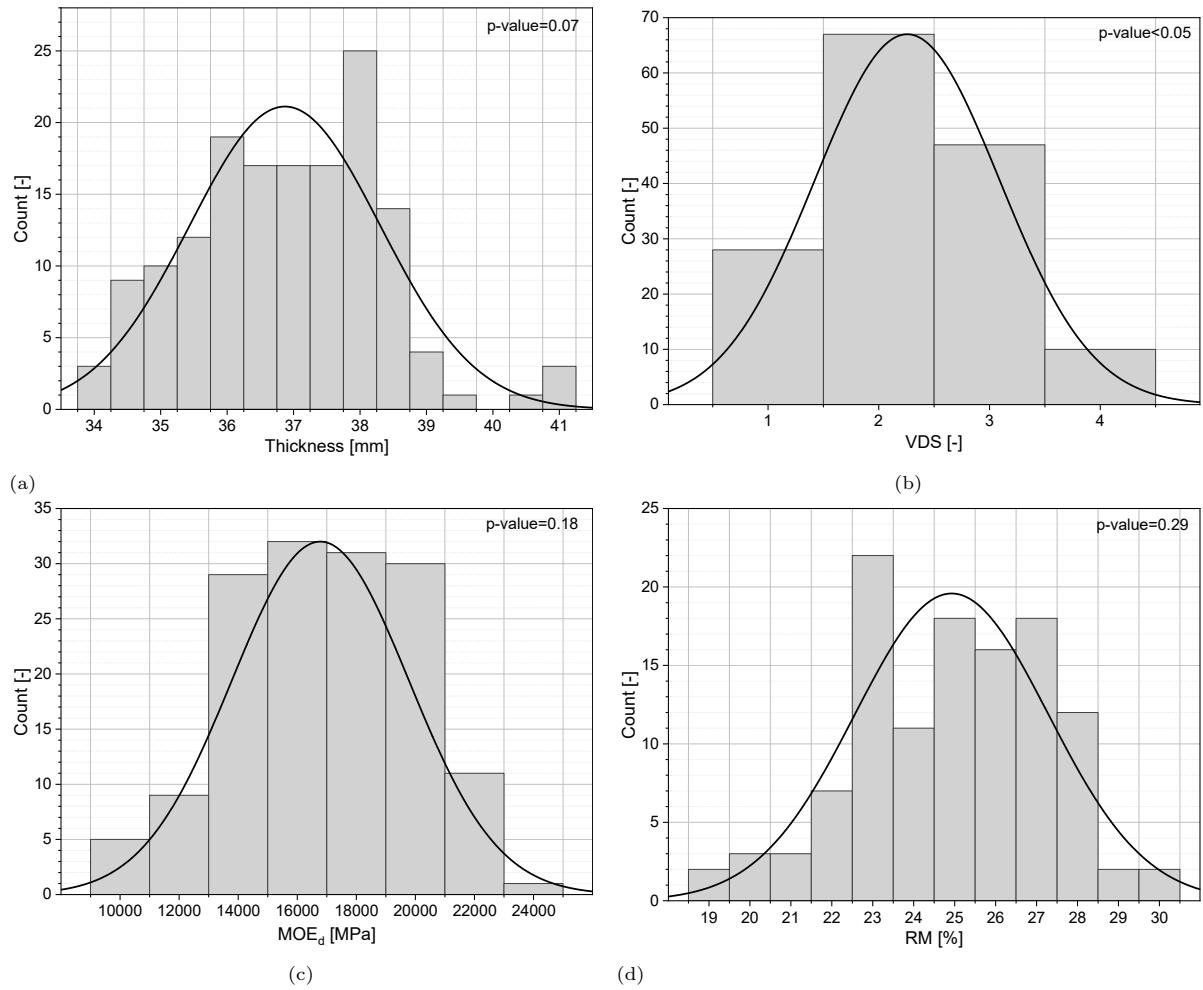


Figure 4.4: Histogram - (a) Thickness (b) VDS, (c) Dynamic MOE, (d) RM%

4.2.3. Destructive test results

In figures 4.5a and 4.5b, the histogram of the results from the four-point bending test is shown and their p-values 0.05 confirm their normal distribution. However, a clear peak is not observed in the bending strength distribution near the median and the peak occurring does not coincide with the median. During the four-point bending a regular cracking pattern was observed as shown in figure A.10, which affirms the spiral grain that generally occurs in Azobé (van de Kuilen et al., 1996). From the grain angle deviation distribution that is shown in figure 4.5c, no clear conclusion can be made. Though the histogram of MC does not follow normal distribution since $p\text{-value} < 0.05$ as shown in figure 4.5d, most specimens have a moisture content above the fibre saturation level of 28% except for 9 boards. The validity of results from these 9 boards is checked in appendix B, whether this data can be included for analysis.

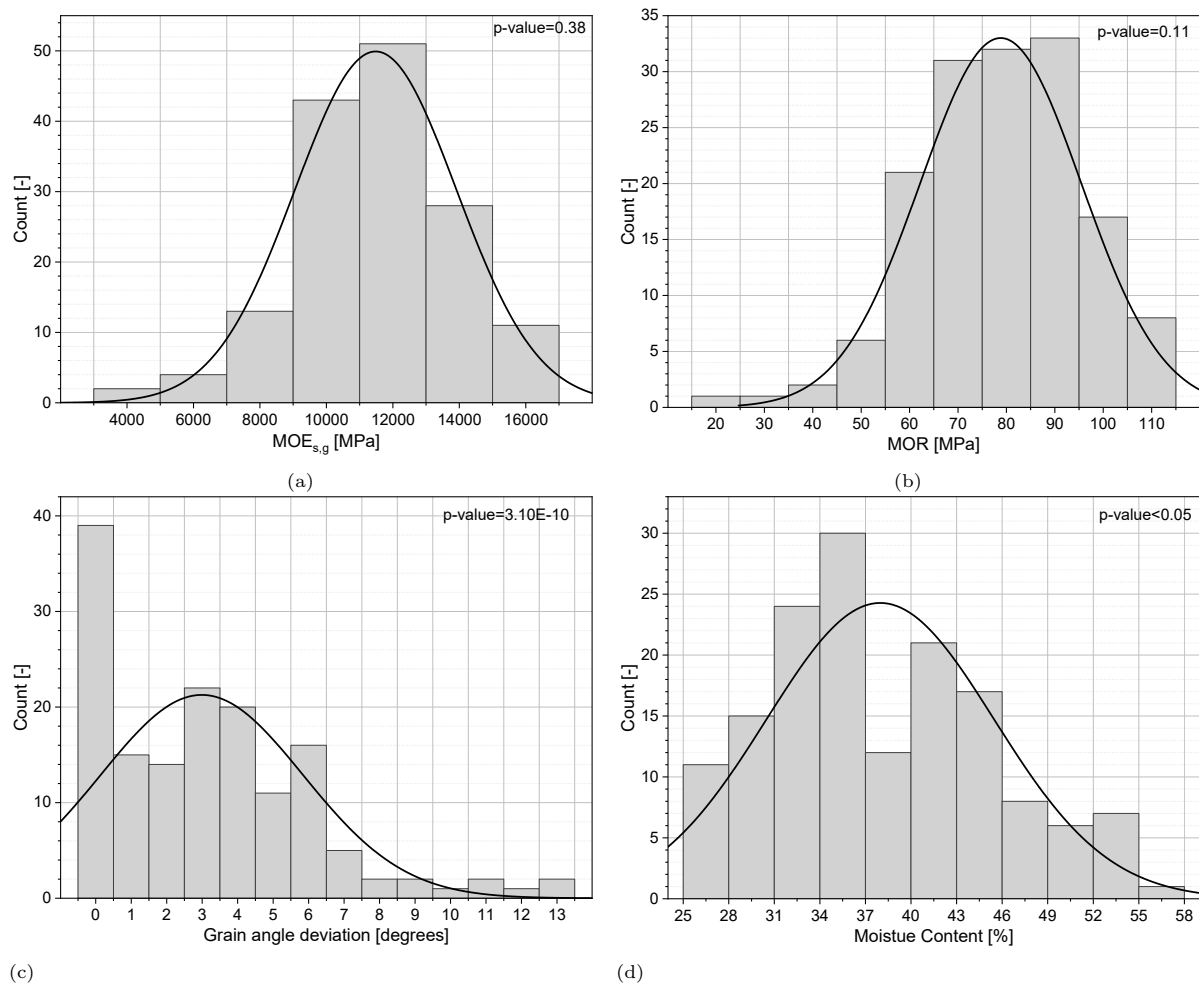


Figure 4.5: Histogram -(a) Global static MOE, (b) bending strength, (c) grain angle deviation and (d) moisture content

4.3. NDTs and DTs relation

In figure 4.6, the visual decay score is checked for correlation with the respective mechanical strength properties and even though a correlation between the VDS and $MOE_{s,g}$ can be seen, no correlation is seen with respect to the bending strength. Figure 4.7a shows a strong correlation ($R^2=0.48$) between dynamic and global static MOE. Except for section 4.1, in the current chapter, the strength properties calculated at their wet density are used instead of the 12% density to which these values were adjusted as explained in section 4.1.1. From the RM vs bending strength and stiffness plots (figure 4.9, no clear correlation ($R^2=0.07,0.11$) can be observed.

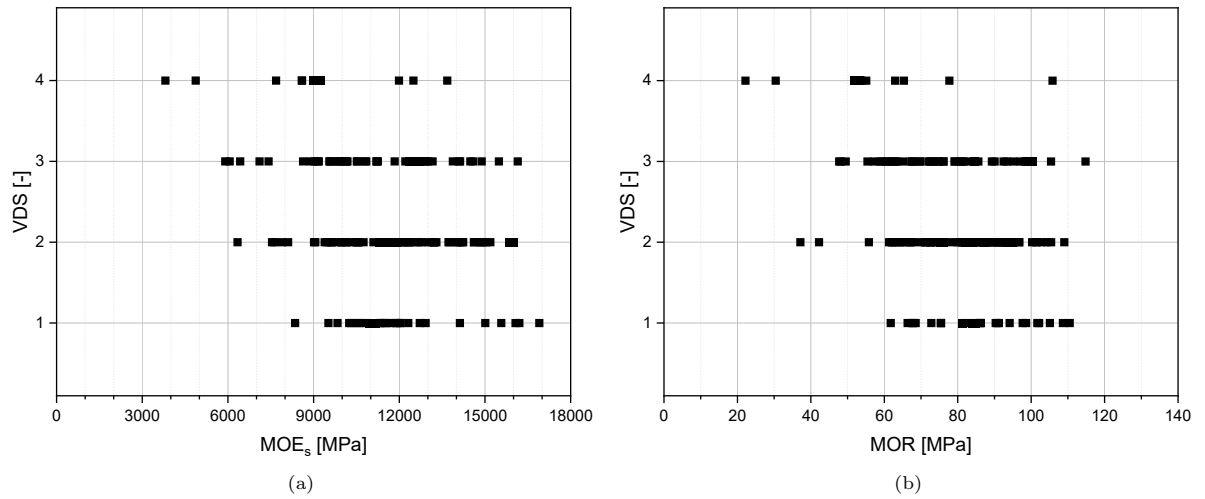


Figure 4.6: (a) Visual decay score vs Global static MOE (b) Visual decay score vs Bending strength

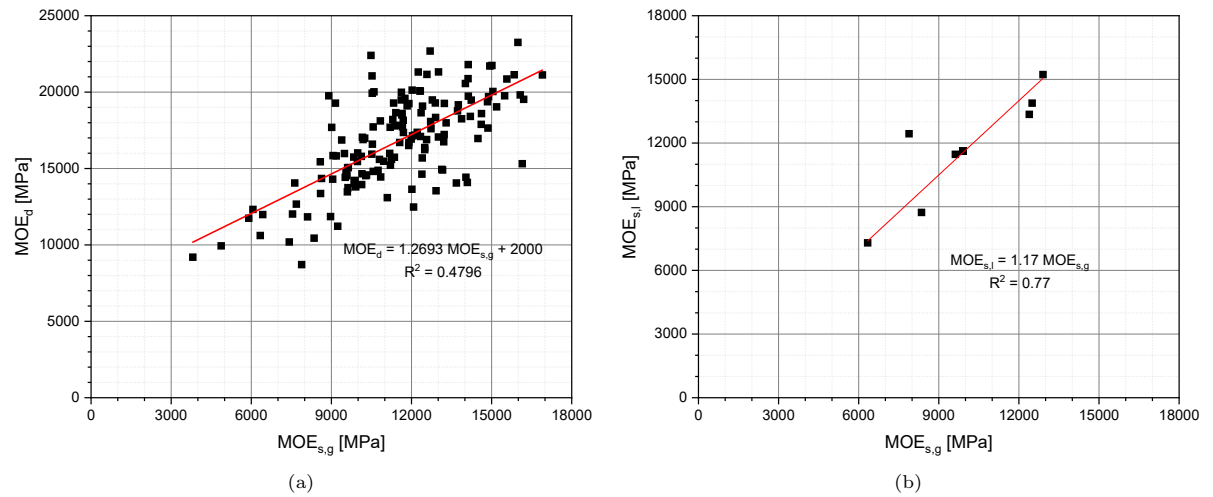


Figure 4.7: (a) Dynamic MOE vs Global static MOE (b) Local static MOE vs Global static MOE

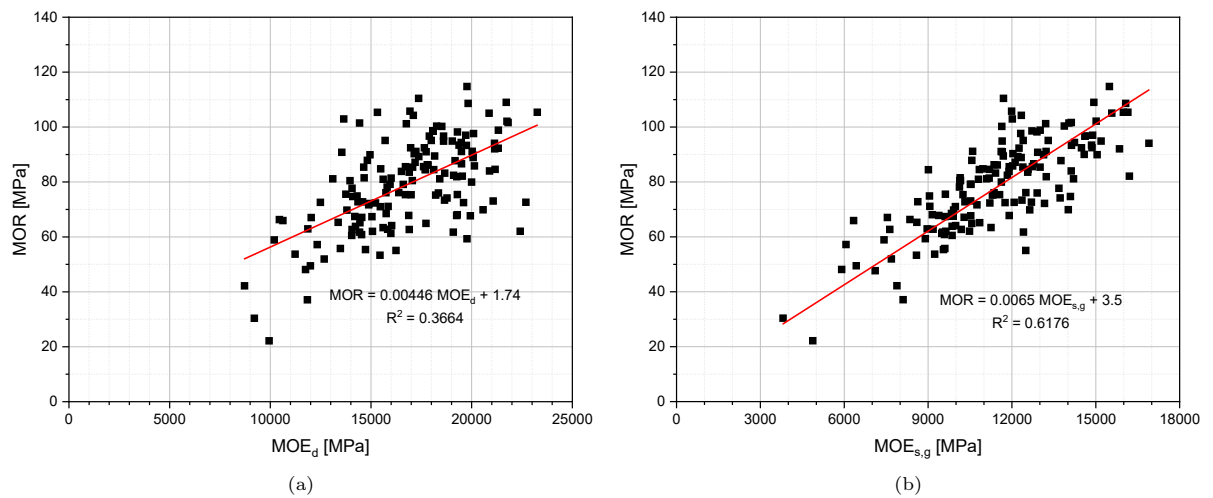


Figure 4.8: (a) Bending strength vs Dynamic MOE (b) Bending strength vs Global static MOE

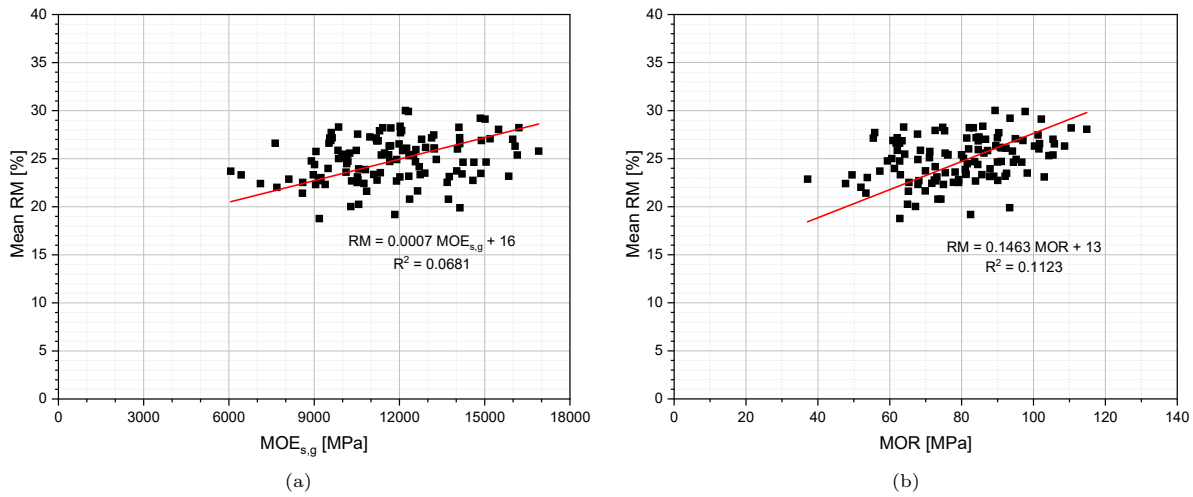


Figure 4.9: (a) Resistographic Measure vs Global static MOE (b) Resistographic Measure vs Bending strength

4.3.1. In comparison with softwood and hardwoods

The relation between the bending strength and MOE is compared with the results of Ravenshorst (2015) in figure 4.10. While in section 4.1, the values from the experimental tests were compared with literature that was specific and relevant to that of Azobé sheet-piles, figure 4.10 shows the relation of the bending strength and the dynamic and static MOE in comparison with timber in general (G. J. P. Ravenshorst, 2015). An elliptical scattering pattern of the overall dataset is observed, which was similar in shape to the scattering pattern observed by Ravenshorst (2015) for tropical hardwoods in general as shown in figure 4.10. However, there is a significant shift leftwards and bottomwards in both the x and y direction respectively. In figure 4.11, the values of the local and global static MOE are validated by relating them with each other and comparing them with results from Ravenshorst (G. J. P. Ravenshorst, 2015).

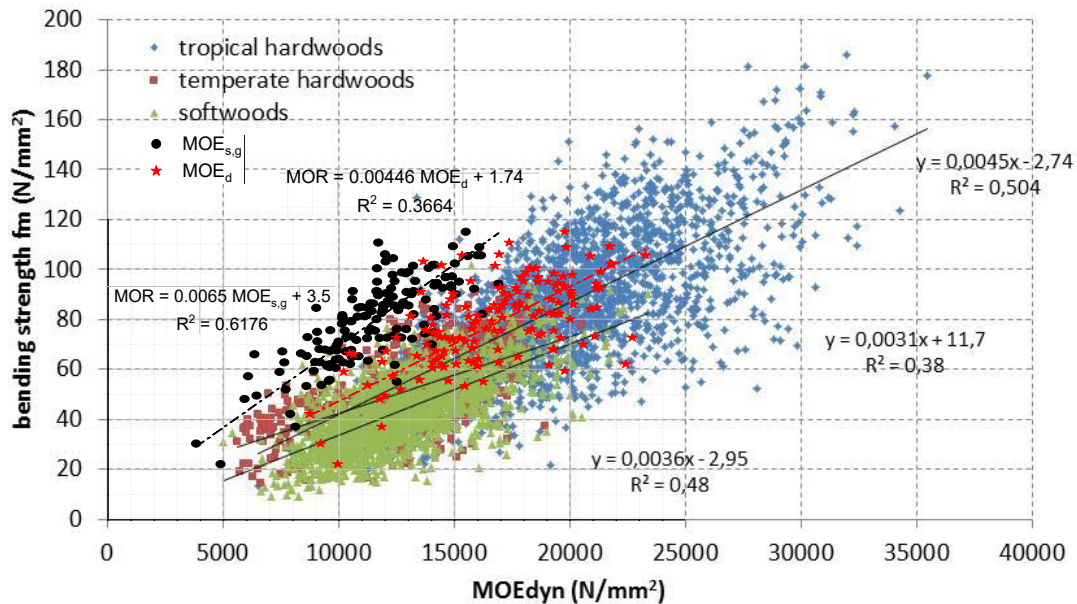


Figure 4.10: Bending strength vs Dynamic and Global MOE in reference to results from Ravenshorst (2015)

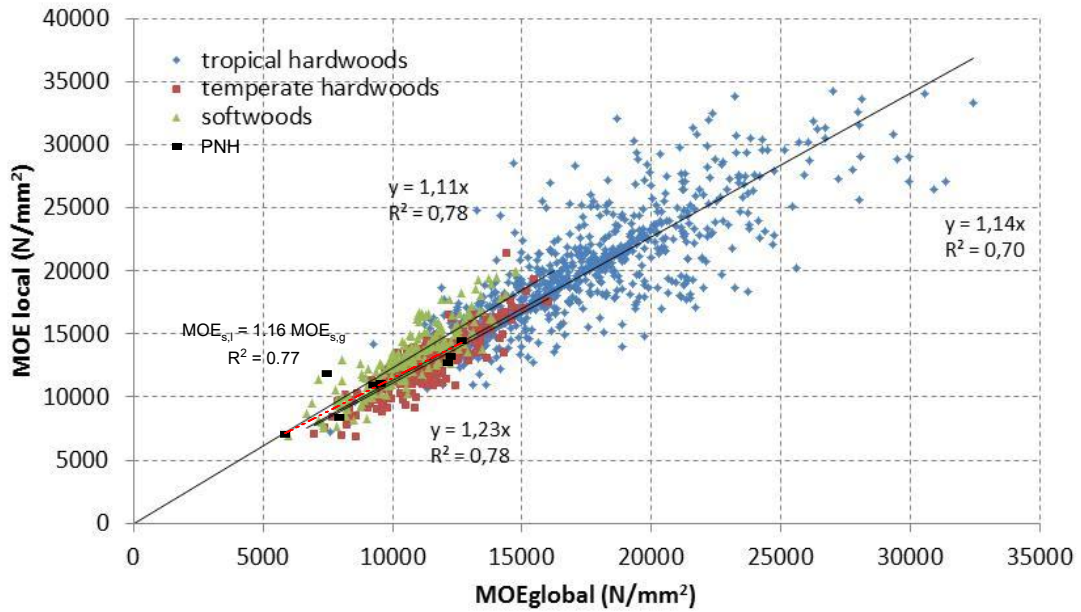


Figure 4.11: Local vs Global static MOE in reference to results from Ravenshorst (2015)

4.3.2. Correlation with density

Figure 4.12a shows the comparison of each board's wet and 12% MC density with its global static MOE. The wet density has low to no correlation with the mechanical stiffness ($R^2=0.09$) while the 12% density, while scattered more does not have any better correlation with the stiffness ($R^2=0.1$). As seen in figure 4.12b, there is a good correlation between the moisture content 12% density with an R^2 value of 0.415 and a negative slope. The relationship between the grain angle and bending strength is not in compliance with the Hankinson equation or with the findings established in Ravenshorst, (2015). The correlation between the RM and both the densities as shown in figure 4.13a is very low (0.25 for 12% MC and 0.20 for wet). This can be due to the limitation that drilling only 6 holes in each sheet-piles cannot accurately predict the overall density of the board. Gard et al. (2018) state that micro-drilling identifies the density gradient along the direction of the drilling and this is shown in appendix F.

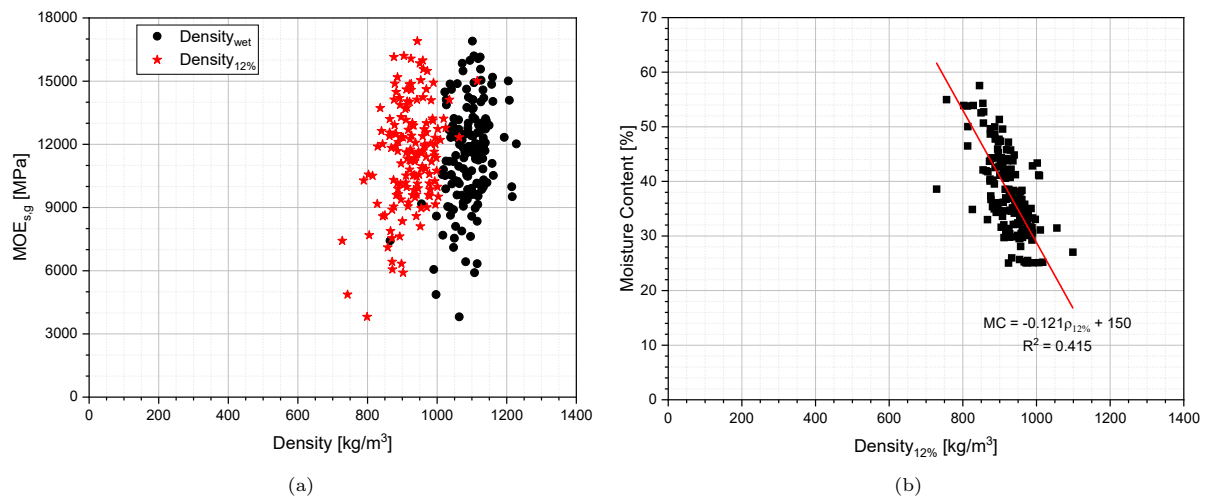


Figure 4.12: (a) Global static MOE vs Density_{wet} & Density_{12%} (b) Moisture content vs Density_{12%}

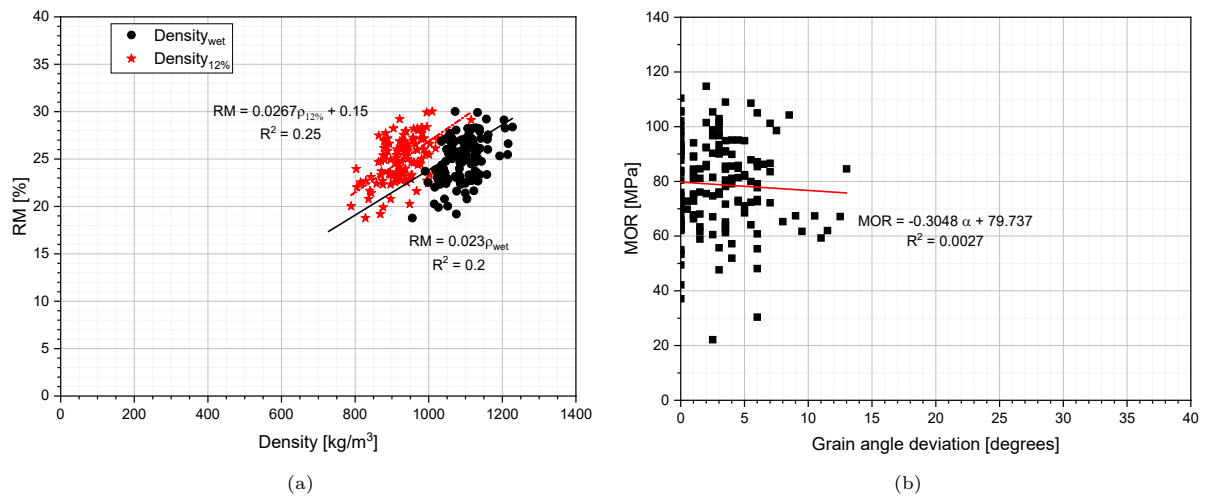


Figure 4.13: (a) Resistographic measure vs Density (b) Bending strength vs Grain angle deviation

4.4. RPD test - drill locations

As shown in section 3.5.2, the RPD test was carried out at six different locations, out of which each set of two drillings were different configurations of the same location, and the resistographic measure calculated based on equation 3.1 for each of these locations are checked for their distribution in the form of boxplot in figure 4.14. This distribution of the RM at individual locations is compared with each other, the mean of the three different locations: top (T), middle (M) and bottom (B) and with the overall average RM of each board. No conclusive pattern can be noticed in the distribution when comparing the drillings made from the W to E side and vice versa. Nevertheless, in general, the pattern where the median of the M value is clearly higher when compared to the closely lying medians of T and B can be observed in both drilling directions.

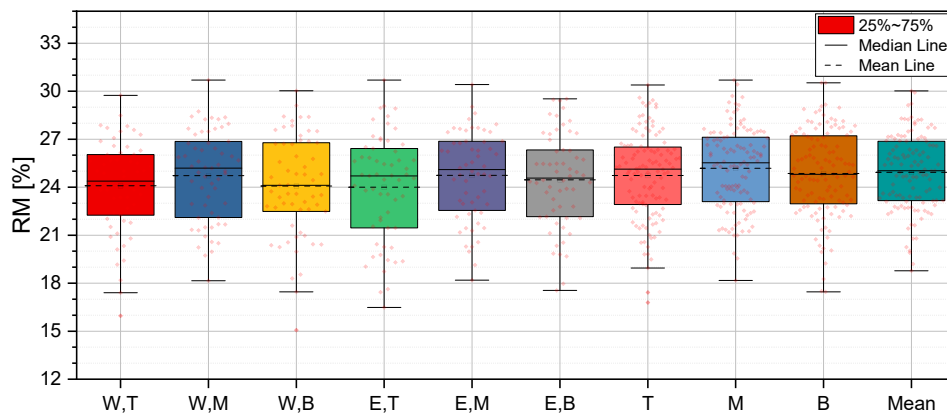


Figure 4.14: Resistographic Measure at various drill locations

4.5. Four-point bending test configurations

The four-point bending test is carried out in four different configurations as explained in section 3.6.2. Figures 4.17a and 4.18a show the variation in the distribution of results obtained from different configurations, while figures 4.15 and 4.16a draw a comparison between destructive and non-destructive tests. From an initial glance at the configuration-wise plots, no striking difference is seen between each configuration and the effect of using different configurations for bend-testing the boards is negligible. However, the possibility of configuration testing having an impact on the result is explored much further in section 4.5.1 and figure 4.30.

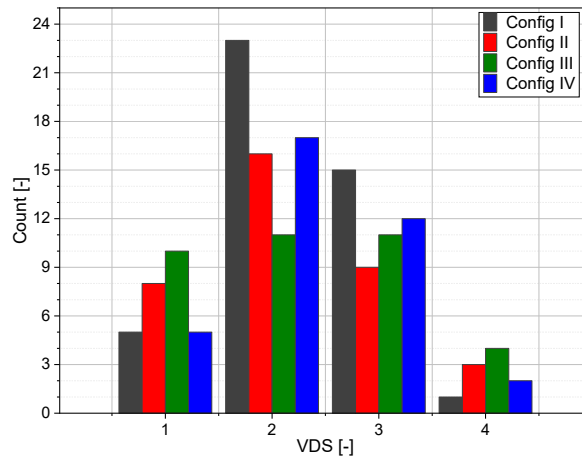


Figure 4.15: Visual Decay Score: Configuration wise

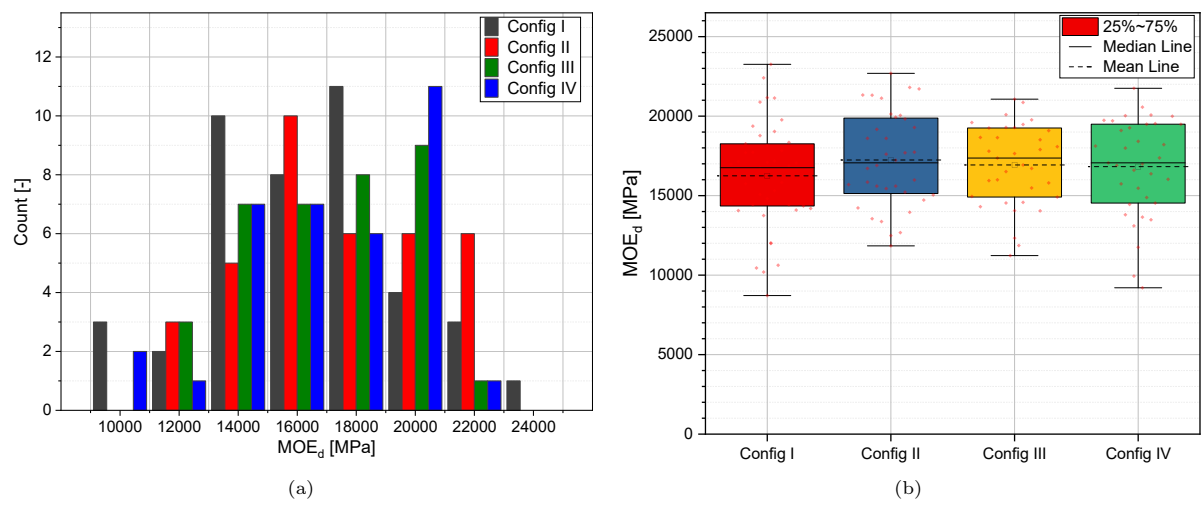


Figure 4.16: Dynamic MOE: Configuration wise (a) Histogram (b) Box plot

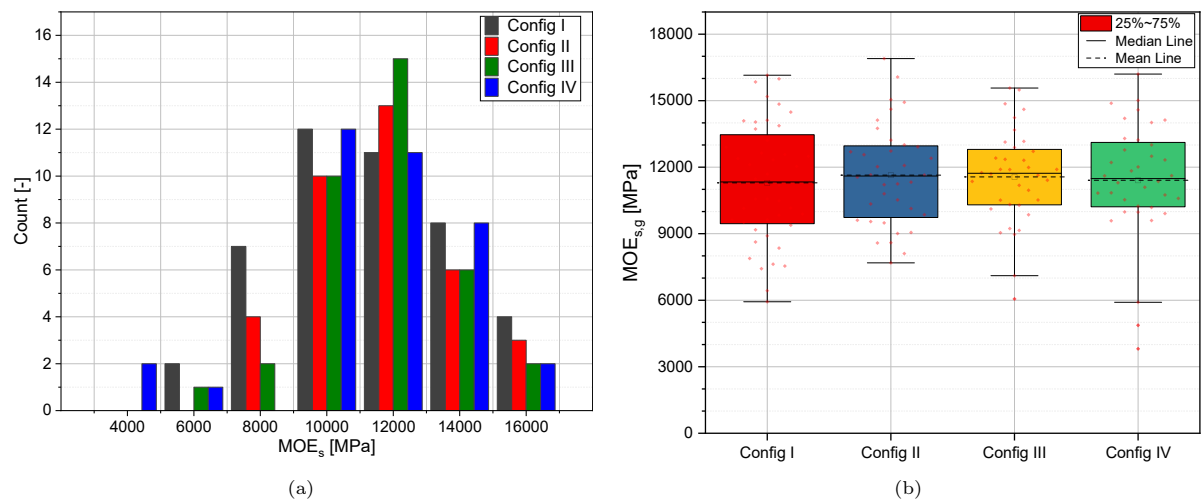


Figure 4.17: Global static MOE: Configuration wise (a) Histogram (b) Box plot

No clear conclusion was made when comparing the correlation between the strength and stiffness parameters configuration-wise as shown in figures 4.19 and 4.8b. However, a clear increase in the amount of scatter of config IV results was observed and this was not related to any specific property of

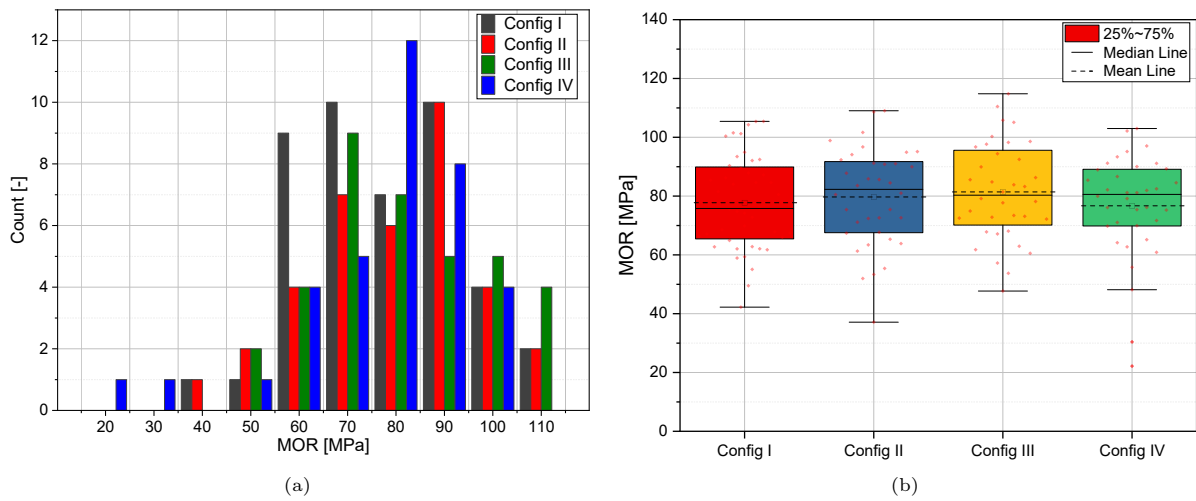


Figure 4.18: Bending strength: Configuration wise (a) Histogram (b) Box plot

the specific sheet-piles. Significantly increasing the sample size and testing more boards might show a prominent difference between these properties, if any.

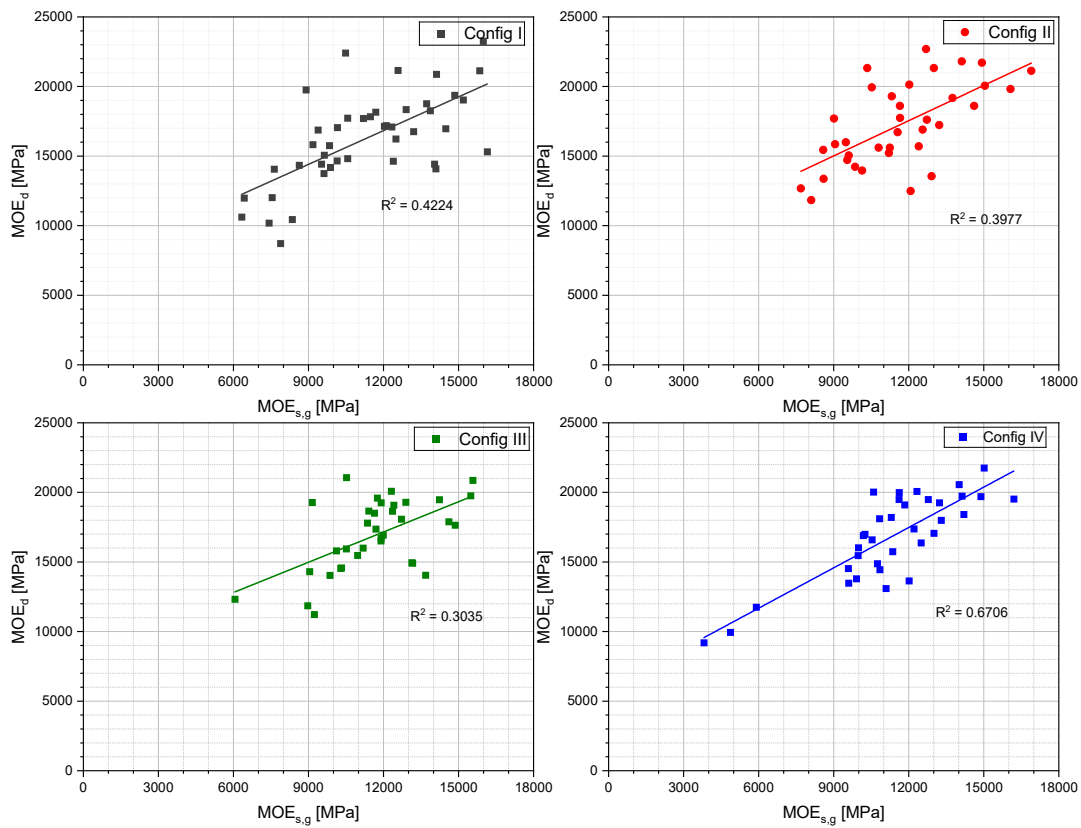


Figure 4.19: Dynamic MOE vs Global static MOE - Configuration wise

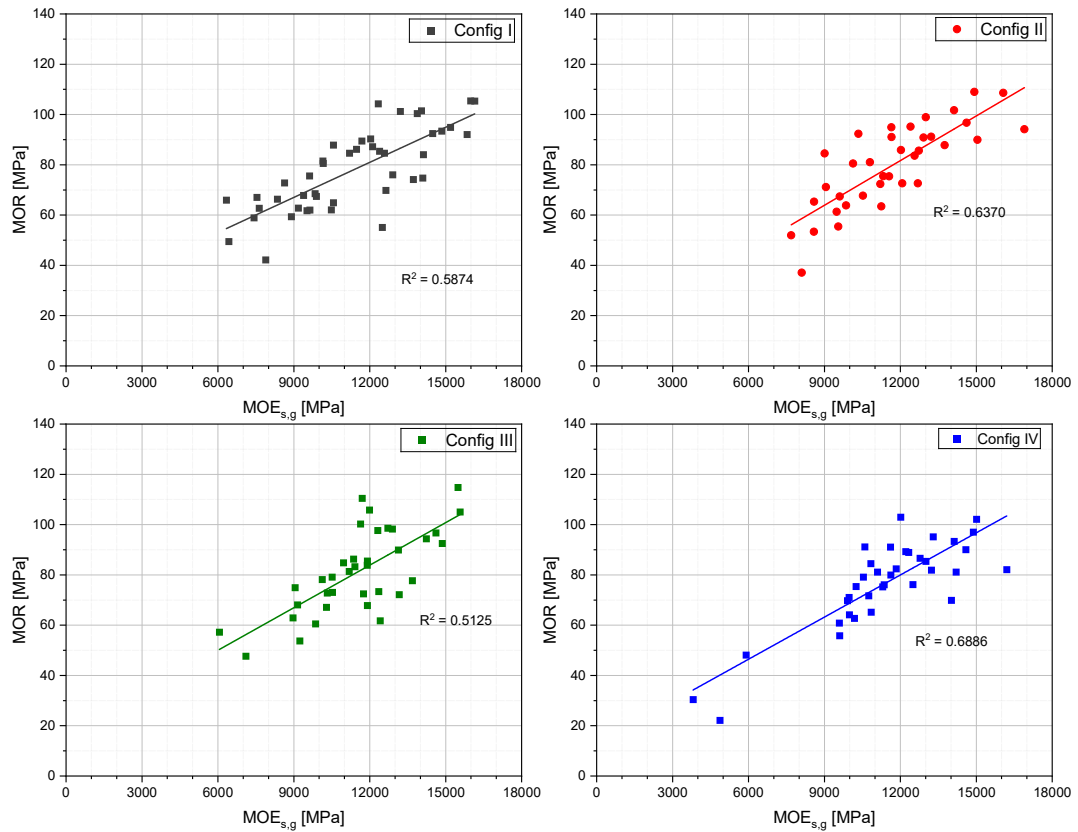


Figure 4.20: Bending strength vs Global static MOE - Configuration wise

4.5.1. Impact of W and E side testing

Although no clear conclusion could be drawn from the configuration testing of the boards, the impact the side of the board facing upwards during the bending test has on the resulting parameters was assessed. Initially, the overall mean value of each of the parameters assessed was used to normalise these parameters by dividing them by the mean itself. The boxplot distribution of such normalised data is presented in figure 4.21. It was observed that no significant difference between the W and E-side tested boards are seen, and in terms of the bending stiffness and the strength values, the W-side-up boards had lesser values compared to the E-side-up boards. This could be related to the E side being exposed to tensile stresses when the W side is up and the E side being decayed having lesser tensile strength, which is usually the decisive factor in the bending of timber. On the other hand, while looking at the scattering of different properties in figures 4.23 and 4.24, the trendlines of the W-side-up boards have slightly less slope or are shifted slightly on the leftwards or bottomwards which agrees to the distribution observed in figures 4.21 and 4.22.

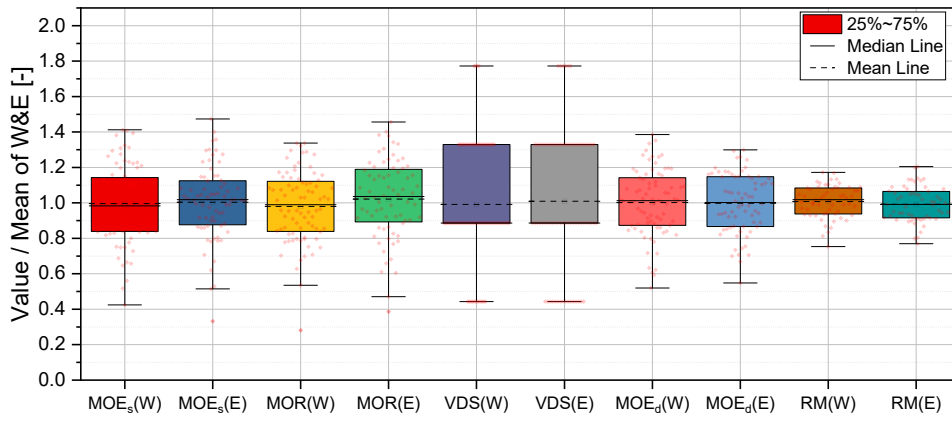


Figure 4.21: Normalised value of each parameter

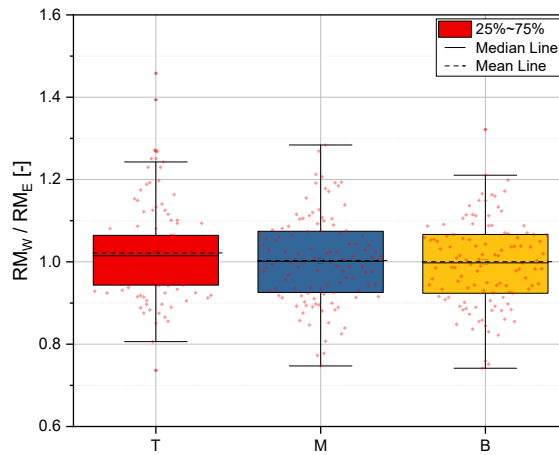


Figure 4.22: Boxplot - Ratio of W to E side RM values at different locations within each board

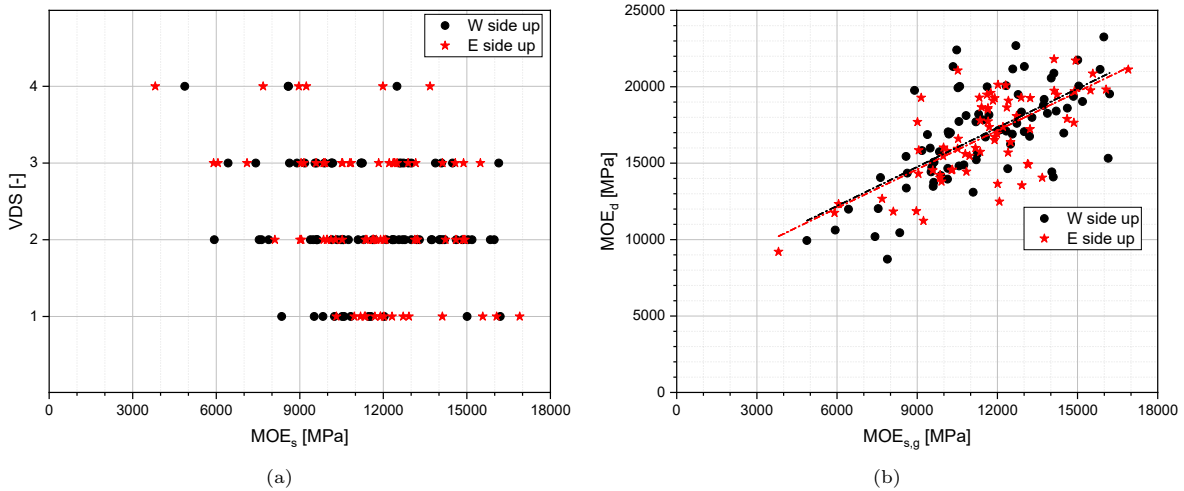


Figure 4.23: (a) Visual decay score vs Global static MOE (b) Dynamic MOE vs Global static MOE - sorted by side facing upwards during four-point bending test

4.6. Top vs Bottom boards

4.6.1. Individual parameters

In order to understand the decay that the full sheet-pile (top and bottom board together) has undergone, its relation to the load-bearing properties has to be analysed. Since each sheet-pile was cut into two

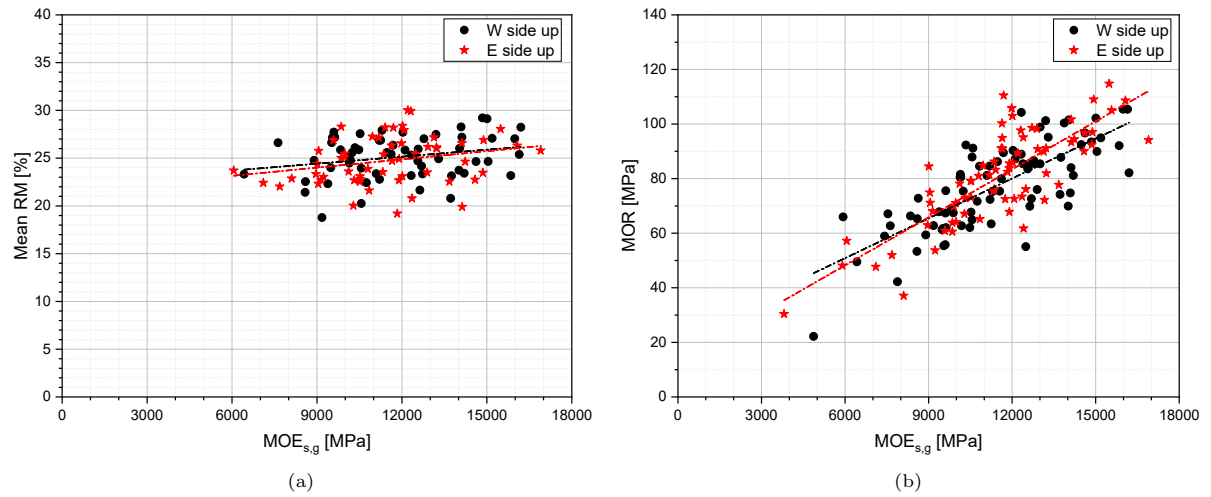


Figure 4.24: (a) Resistographic measure vs Global static MOE (b) Bending strength vs Global static MOE - sorted by side facing upwards during four-point bending test

boards initially and the top and bottom were distinctly named, by comparing their experimental test results (both DTs and NDTs), the effect of decay along the length can be found. From figure 4.25, it becomes clearly evident that in most of the sheet-piles, the top board has a better VDS compared to its bottom counterpart. However, when the mechanical strengths of the top and bottom are compared in figures 4.27, 4.29 and 4.31, this distinct superiority does not exist and the number of sheet-piles with stronger or stiffer top boards compared to the bottom and vice versa is almost equal. Even their distribution does not vary by >5% on average and the top boards are less stiff and less strong compared to the bottom ones as shown in figure 4.26 and 4.32a.

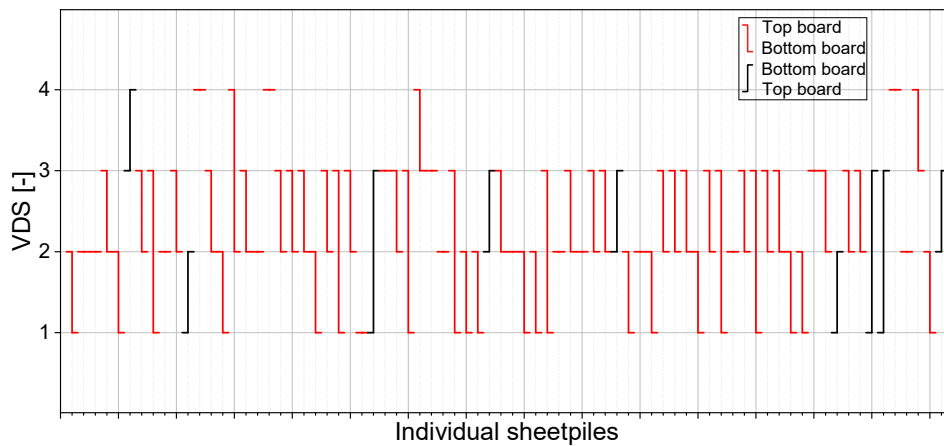


Figure 4.25: Top vs Bottom - Visual Decay Score

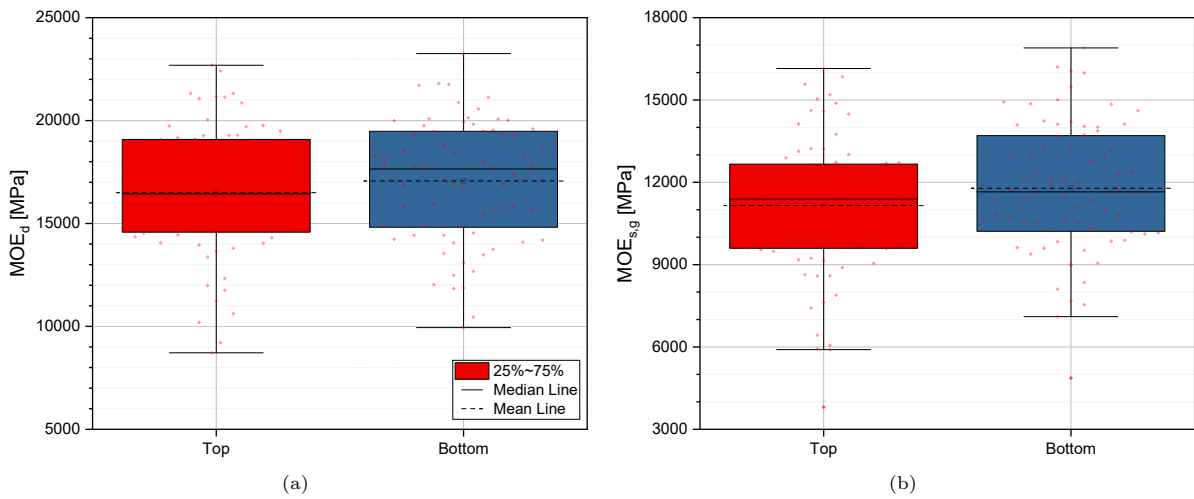


Figure 4.26: Boxplot distribution Top vs Bottom boards - (a) Dynamic MOE (b) Global static MOE

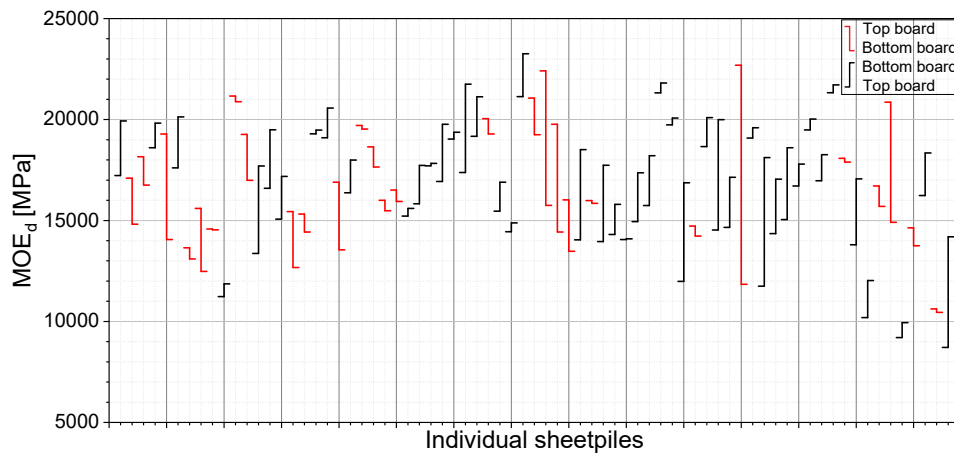


Figure 4.27: Top vs Bottom - Dynamic MOE

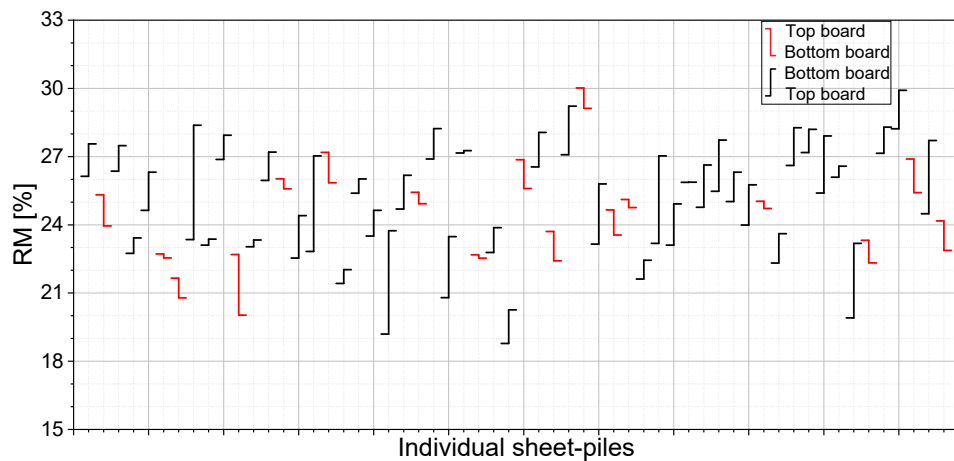


Figure 4.28: Top vs Bottom - Resistographic Measure

In figure 4.30, the impact of configuration testing with respect to the difference between the top and bottom boards is analysed as this comparison would be most relevant and in case any difference would occur, it would be evident in this analysis, but no significant difference between any configuration is observed. It can be concluded that, with respect to the top and bottom boards of each sheet-pile, the

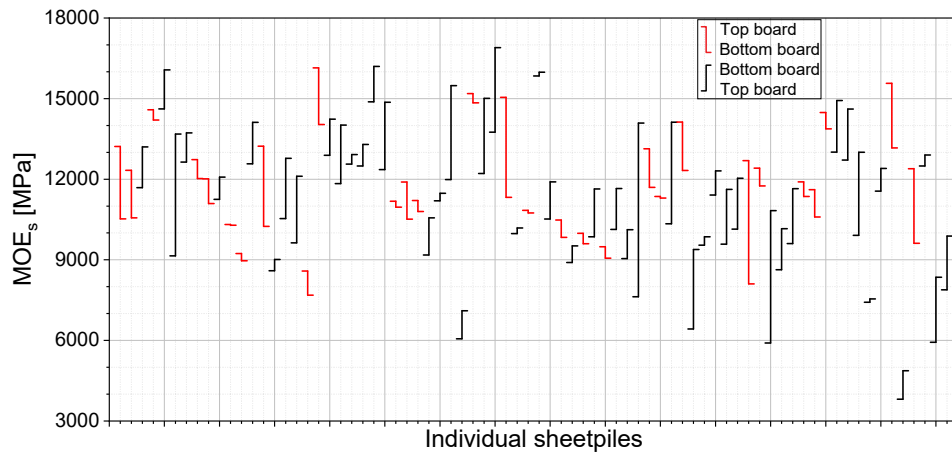


Figure 4.29: Top vs Bottom - Global static MOE

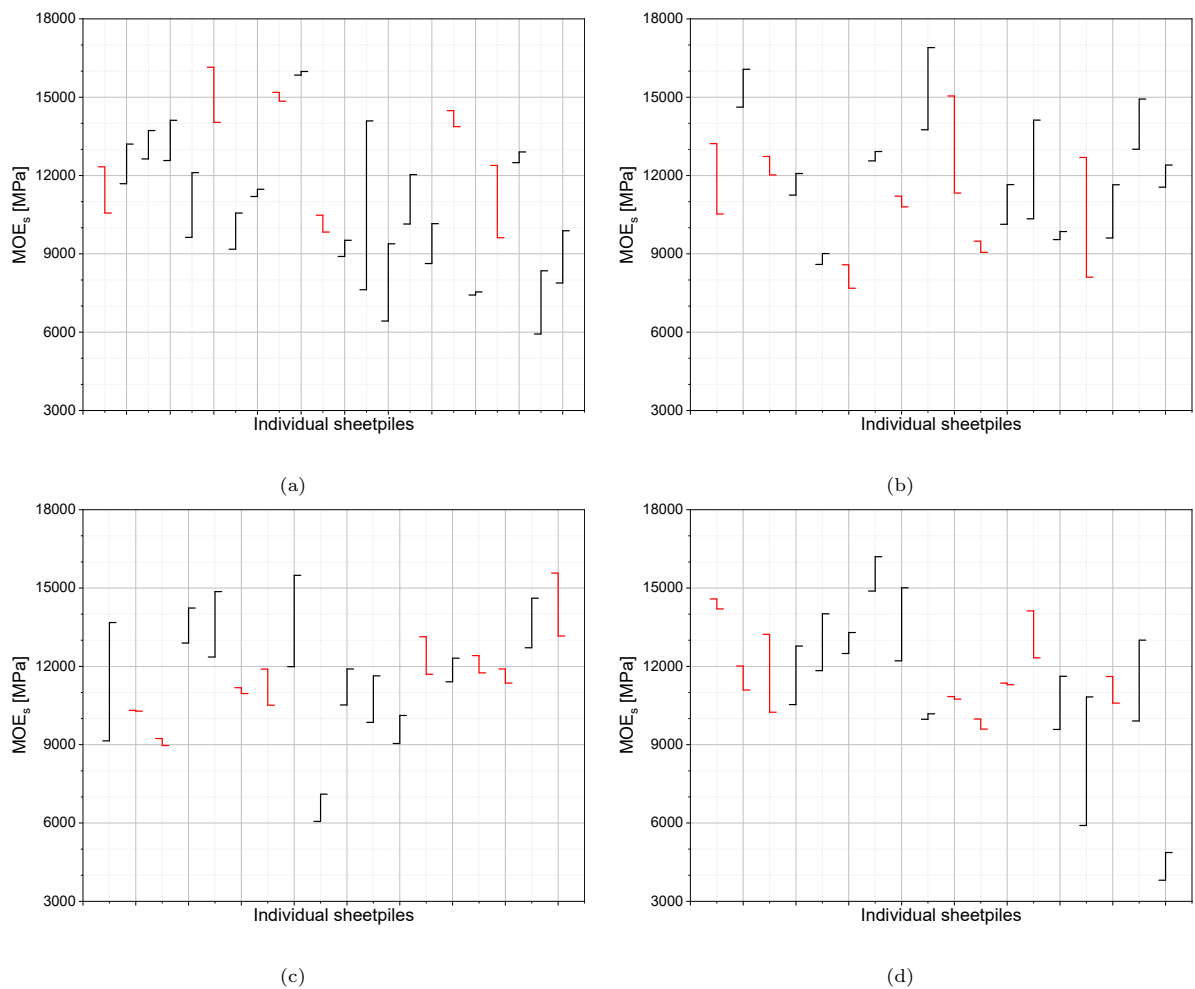


Figure 4.30: Configuration wise global static MOE - Top vs Bottom (a) Config I (b) Config II (c) Config III (d) Config IV

VDS are misrepresentative of their difference in actual mechanical properties. This statement is also reinforced by figure 4.32b, which shows the distribution of the ratio of top to bottom parameters and the distribution's median is clearly less than 1, while even the extreme 25% of the values are unsymmetrical about the unity axis and lean more towards lower the bottom half.

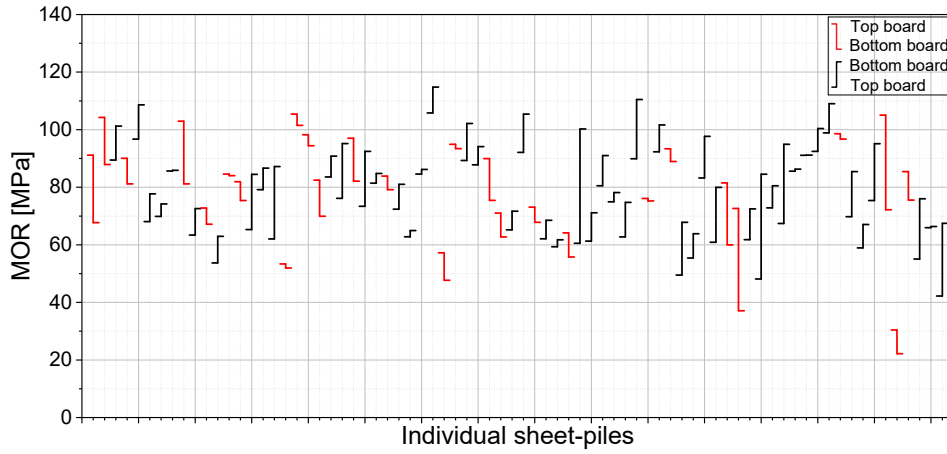


Figure 4.31: Top vs Bottom - Bending strength

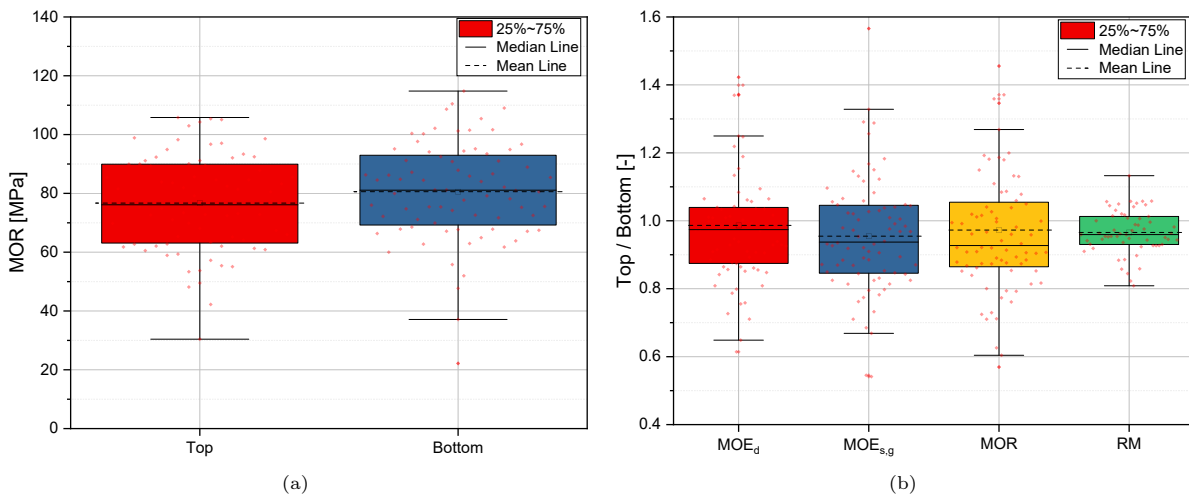


Figure 4.32: (a) Boxplot distribution Top vs Bottom boards - Bending strength (b) Ratio of top to bottom counterpart boards

4.6.2. Correlative parameters

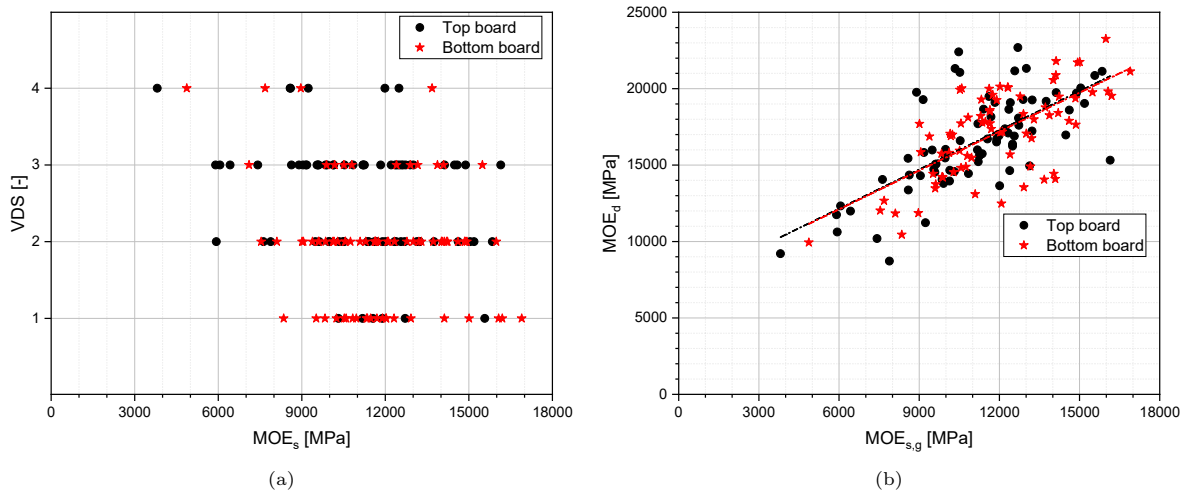


Figure 4.33: (a) Visual decay score and (b) Dynamic MOE vs Global static MOE - Top and bottom boards

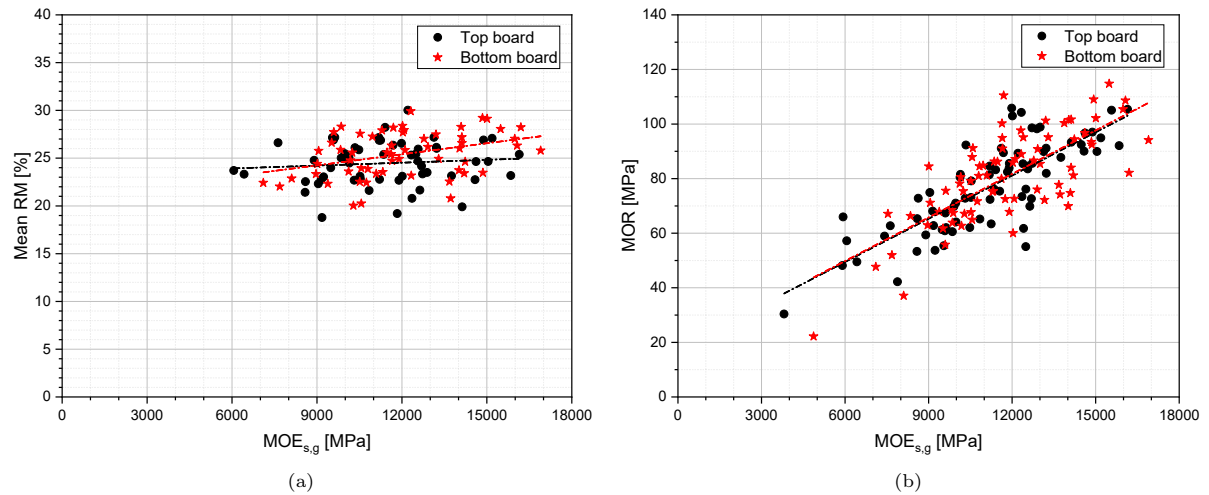


Figure 4.34: (a) Resistographic measure and (b) Bending strength vs Global static MOE - Top and bottom boards

4.7. Influence of geometry

4.7.1. Tongue and Grooves

For the calculation of the moment of inertia (that directly influences the mechanical properties of the board such as bending strength and static MOE), an equivalent rectangular cross-section is assumed as shown in figure 4.35a with a moment of inertia I_{calc} . This assumption keeps the calculation much simpler and consistent with respect to the minor changes that occur between the tongue and groove sizes of different boards. Figure 4.35b shows the ideal tongue and groove geometry, which has a moment of inertia, $I_{ideal} = 1.05I_{calc}$. Since all of the boards have undergone decay of varying levels, the best and worst case is considered in terms of the cross-sectional geometry. A board with reduced thickness towards the E side, but still has all of its tongue and grooves intact is considered as shown in figure 4.35c, while a board with the groove facing the E side completely decayed is shown in figure 4.35d. The former has an $I_{actual} = 1.06I_{calc}$ and the latter with an $I_{actual} = 1.09I_{calc}$, proving that the mechanical strength and stiffness have been underestimated in the thesis by a factor varying between 6% & 9%.

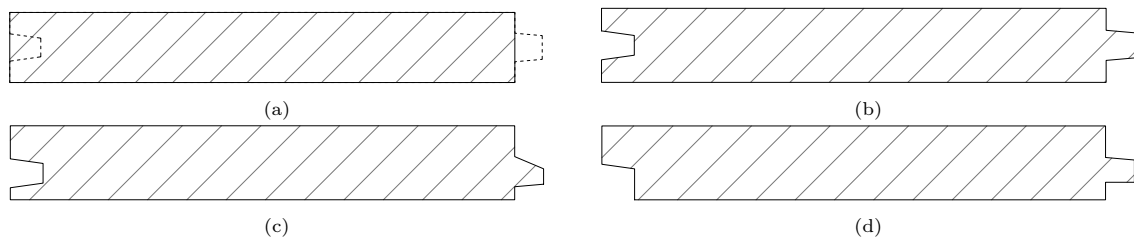


Figure 4.35: Cross-sections of the sheet-pile boards (a) assumed for calculation (hatched) vs ideal (dotted) (b) with ideal tongue and grooves (c) decayed (d) decayed and missing groove

4.7.2. Variation in thickness

Each set of thickness measurements recorded at different locations of each board is represented as an individual vertical line in figure 4.36. According to NEN 5493 (2010), while designing sheet-piles the maximum permitted deviation in the nominal thickness of the sheet-piles is ± 2 mm. However from figure 4.37, it is evident that for most of the boards, this variation in the thickness is >2 mm even though this was not due to the design intention, but due to the uneven decay. From the failure patterns observed in the four-point bending test, almost all of the boards underwent a standard failure process and except a few boards which were rigorously decayed and were awarded a VDS of 4, for the other board this difference in thickness did not play a deciding role in the failure pattern. Additionally, these differences in thickness, though not locally taken into account, are included in the bending strength and stiffness calculated by considering the average thickness of each board.

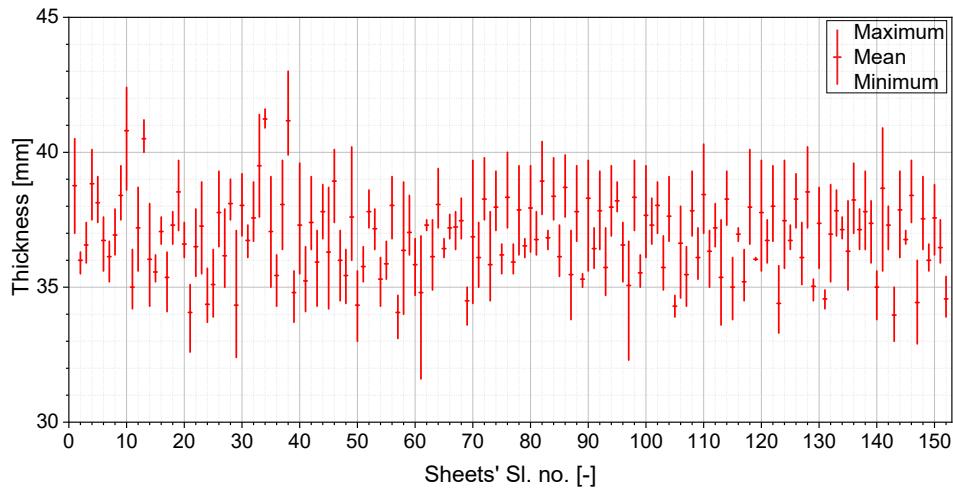


Figure 4.36: Minimum, maximum and mean thickness of each board

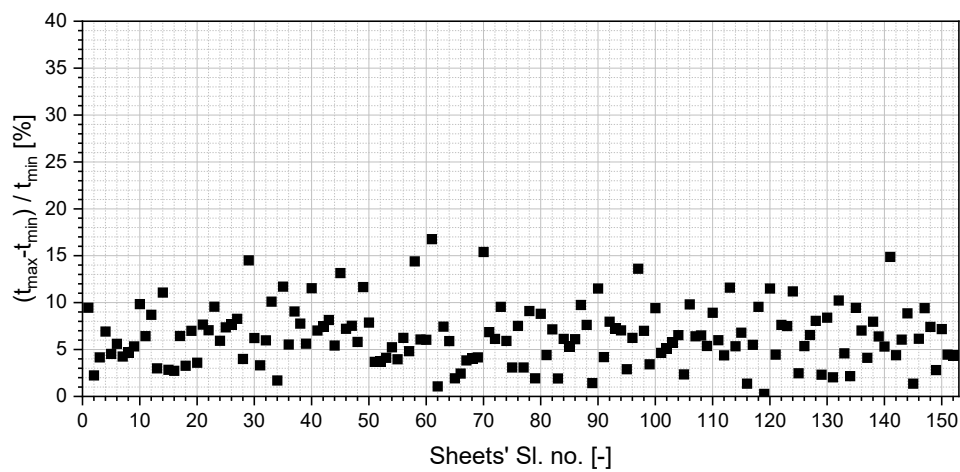


Figure 4.37: Thickness variation within each board

4.8. Comparison of data from lasers and the load cell

From figure 4.38, it is clear that the slope of the $f - d$ curves generated by the lasers is much higher compared to that by the load cell. This can mainly be attributed to the fact that the displacement in the load cell also is not exactly measured where the setup comes in contact with the board that is being tested, and hence the movement and elastic compression of the part and components that the load cell is made of contribute to the additional displacement. The slope of the LS01 curve is consistently high with respect to the LS02 and is also reflected in the distribution as shown in figure 4.38. This could prove that the side with the groove is less stiff compared to the side with the tongue, thus resulting in a minor twisting effect. However the setup with which the test was performed had the supporting frame along with the load cell slightly crooked. It could be possible that this imperfection in the geometry of the setup is resulting in the difference in slopes.

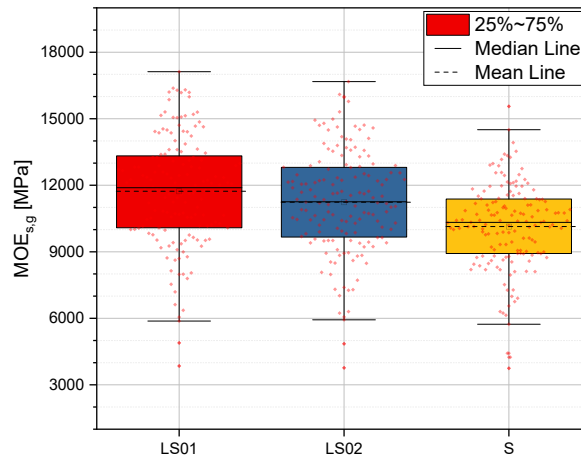


Figure 4.38: Static MOE value calculated from different displacement measuring devices

4.9. Compression test results

From figure 4.39 it is clear that the specimens can be approximated and modelled using a bilinear curve. Similar to the bending test results, the load cell's displacement and curve slope values vary significantly when compared to the values from LVDTs. However, this value is only to understand the overall compression behaviour of the boards. The MOE in compression is calculated from figure 4.39b, in which the slope of data from both LVDTs is considered and then averaged as explained in section 3.10.2. The compression strength has a good correlation with both the compressive MOE and the bending strength as shown in figure 4.40. The relation between the bending and compression strength is essential in the estimation of the tensile strength with which the numerical analysis is performed.

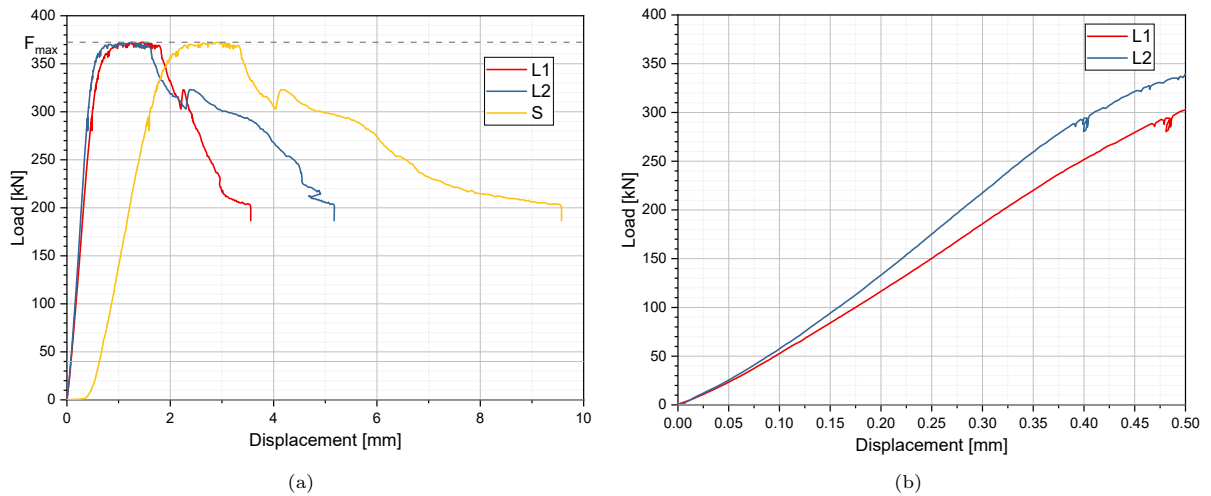


Figure 4.39: Compression force-displacement plot for the specimen PNH40

Comparison of strength and stiffness under compression to the resistographic measure values from the RPD test as shown in figure 4.41 result in a good correlation ($R^2=0.53$ and 0.33 respectively). This can be related to the mechanism used by the testing device to measure the drilling resistance which is used to compute the resistographic measured. The variation in the compressive force applied by the drilling equipment is quantified by measuring the amplitude supplied to it, thereby proportionally relating to the compressive strength of the material it is used to test itself.

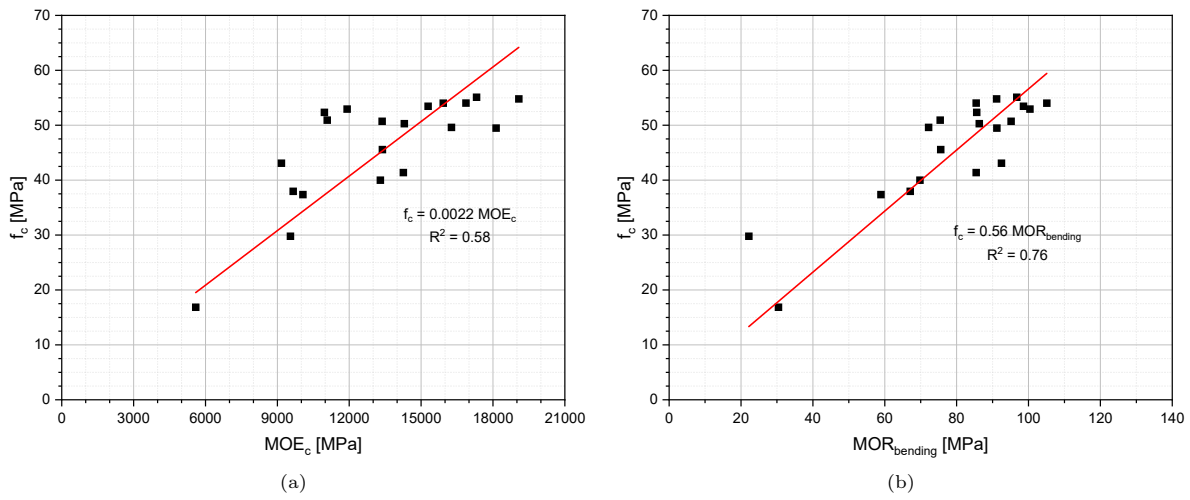


Figure 4.40: (a) Compression strength vs Compression MOE (b) Compression strength vs Bending strength

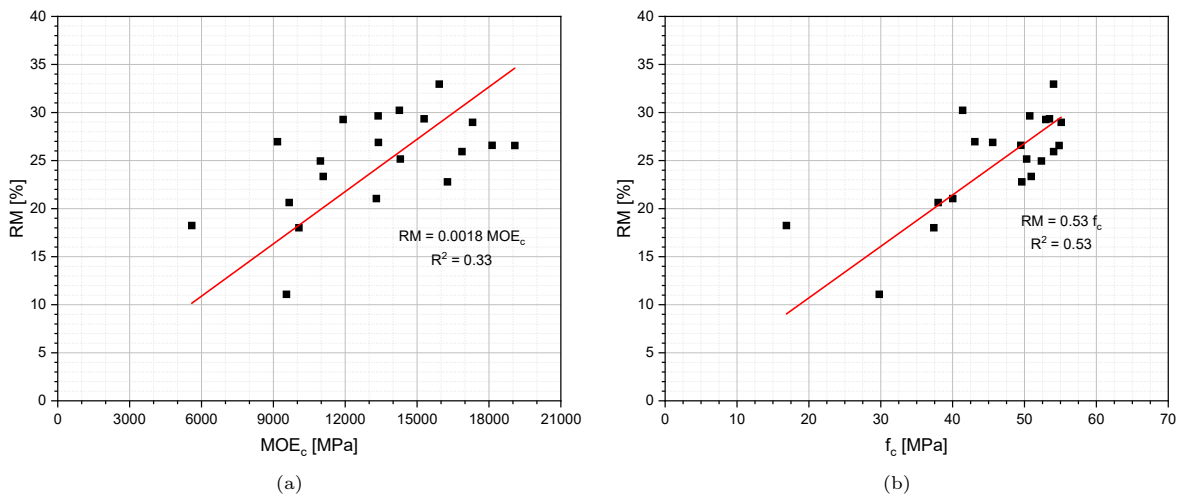


Figure 4.41: (a) Resistographic measure vs Compression MOE (b) Resistographic measure vs Compression strength

5

Numerical analysis

In this chapter, the four-point bending test setup is converted into a numerical model, by incorporating appropriate boundary conditions and using a material model that accurately interprets the behaviour of hardwood under bending. The advantages and the limitation of the different material models are discussed, so as to justify the choice of the model that has been used in the sheet-pile wall model. The process involved in the prediction of LSF along with the used method's limitation and its scope to accurately determine the LSF is also discussed.

5.1. Outline

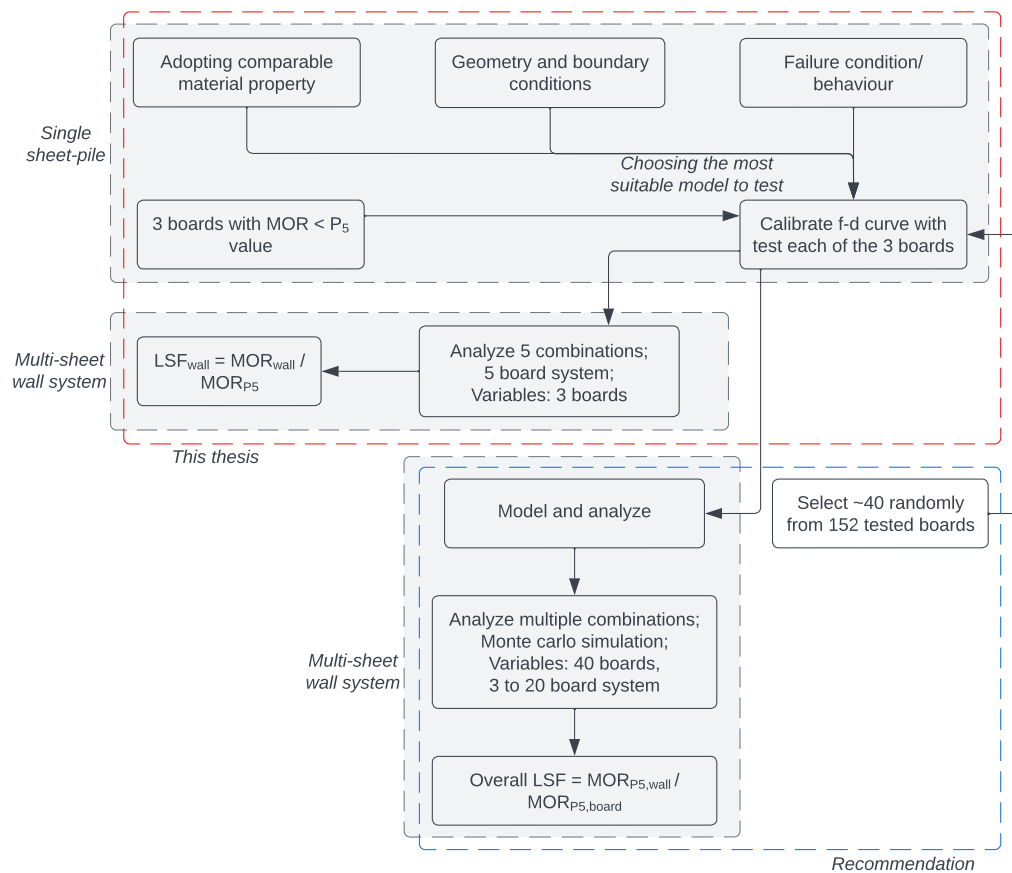


Figure 5.1: Process involved in the determination of the LSF

The numerical analysis' main objective was to forecast the load-sharing behaviour of a sheet-pile wall system and approximate the load-sharing factor. As a first step, the four-point bending test performed on a single board in the experimental analysis was attempted to be replicated numerically using the finite element method program DIANA v10.5. Numerous parameters that affect the numerical model's stability and accuracy are usually involved in this process. It was vital to note what was included in the numerical model and which assumptions were made regarding elements of the material model that were outside the scope of this research because this thesis only focuses on a certain aspect of the overall behaviour of wood. This process of conversion into a numerical model came with its own possible pitfalls. Finding the roots of each of these problems was necessary during the process. Each step involved in this process is shown in sequential order as a flowchart in figure 5.1. An overview of how the numerical analysis was carried out, tackling the problems that were faced is shown in figure 5.2.

The initial aim was to successfully replicate a numerical model as similar as possible to the experimental setup. This numerical model was then scaled up to accommodate multiple boards of the sheet-piles to form a sheet-pile wall system and the load-sharing behaviour was studied and compared with the literature. Five of the weakest combinations of sheet-pile wall systems were modelled and the load-sharing factor was calculated by comparing the bending strengths of the sheet-pile walls and the characteristic wet bending strength obtained from the experimental tests.

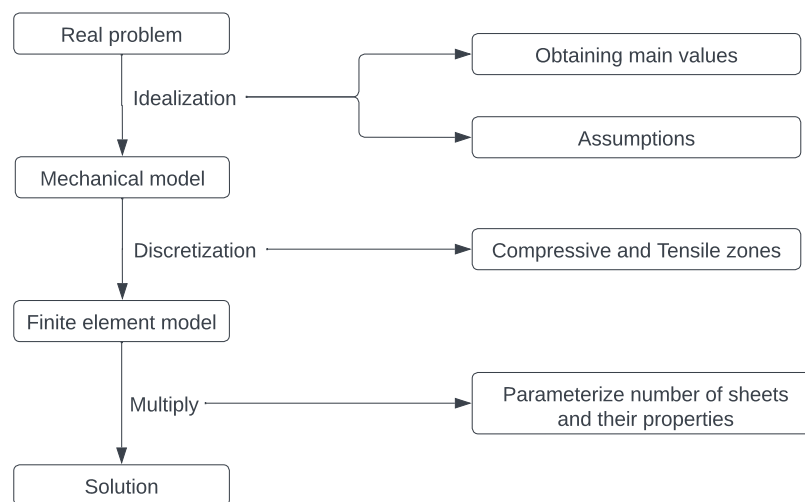


Figure 5.2: Flowchart for conversion of the experimental model for numerical usage

5.1.1. Idealization

During the idealisation process, assumptions are established that, while untrue in reality, are typically close enough to the truth that they do not significantly affect the outcomes. If this does occur, the presumptions must be revised. Establishing the mean values for material attributes and making the right assumptions for the conversion of the test setup into a FE analyzable model are the idealization's two main issues. These are significant since they can be predicted using data from prior studies, but in this instance, it is necessary to duplicate current data from the experiments as closely as possible, therefore the data must originate from the test items themselves.

Obtaining mean values

Getting the average values for a particular species of timber might be challenging, especially when they had undergone variable levels of decay. One of the reasons is that there is actually a wide variation in a species' characteristics, and even within a single tree or board, there might be discernible differences. The combination of these traits with different types and levels of decay scatters the obtainable results even more. This made determining a precise value for a test specimen challenging because not all attributes may be assessed without causing damage.

It is important to note that the mean values obtained from the FEA model will only be as accurate as the

input data used to create the model. It was therefore essential to ensure that the mechanical properties of the sheet-piles were accurately determined through physical testing. Not only the mechanical properties, but the failure behaviour of the sheet-pile board also needed to be taken into account when calculating the numerical failure value associated with it.

Assumptions made for modelling

Several assumptions and engineering judgments were made while converting the four-point bending experiment into a finite element model. These include:

1. **Homogeneity:** It was assumed that the decayed hardwood board was homogeneous, meaning that it has the same material properties throughout its entire volume. This assumption may have different levels of accuracy considering the boards are made of hardwood, which have fewer knots or local defects when sawn in comparison with softwood but could also have significant variations in density or material properties due to decay during its service.
2. **Linearity:** It is also often assumed that the decayed hardwood board behaves in a particularly linear fashion (single, bi or multi-linear), meaning that the stress-strain relationship is proportional to different extents at different stress levels. When aspects such as yielding, cracking or buckling are considered, assumption usually leads to general approximations that were specifically fitted to that particular test, geometry or material type.
3. **Continuum:** The decayed hardwood board is typically assumed to be a continuous, solid body, rather than a collection of discrete particles. This assumption may not be accurate if the board is highly decayed or has significant voids or defects, which in this case although observed were less frequent at the local level when compared to the geometry of the board.
4. **Boundary conditions:** The boundary conditions specified in the finite element model, such as the location and magnitude of the applied load and the supports and constraints on the board, may not perfectly match the experimental setup. This can affect the accuracy of the model.

5.1.2. Discretization

In a finite element model, discretization of a hardwood board being bend-tested involves dividing the model into a series of sufficiently smaller elements, each of which represents a small volume of the model. Factors to consider when discretizing the model include element size, shape, load distribution, boundary conditions, and material properties. Usually, the load should be distributed evenly across the elements to avoid introducing artificial stress concentrations or discontinuities in the model.

In this case, the mechanical problem was divided into smaller components by the discretization method. Decisions were taken regarding the bounding and interface conditions between these smaller parts, each of which was assigned certain features appropriate to themselves based on their location in the model. Other variables like what each of these parts' mechanical properties was, and what directions their nodes could move or rotate depends on the boundary conditions and the resulting stress-strain distribution.

5.2. FE modelling - Individual sheet

Taking into consideration the characteristic material properties of the hardwood such as elastic stiffness and maximum stress that it can take in tension and compression, an attempt was made to model the force-displacement graph. The model was iterated with several combinations of geometrical approximation, mechanical properties and support and loading conditions to keep them as close to the actual test setup as possible and also obtain numerical test results that agree with the experiments. Material properties that were available from the tests were considered keeping in mind the most probable or frequently occurring failure patterns although the failure of the beams showing their cross-grains cannot be directly modelled with DIANA. In order to initially model and calibrate to the experimental tests, one of the samples from the experiment (PNH133-1) that has its bending test result combination as close to the average value of the entire sample set as possible was chosen. For all that initial focus set on replicating the elastic regime of the force-displacement graph, its softening curve and the compressive stress redistribution along with the peak load were the main points of focus.

The model had a few design revisions. The basic idea of discretizing the zone undergo tensile and compressive stress due to the uniaxial bending was implemented in 3 different ways as 2D and 3D

models, with different finite element types to understand the difference between them, if there was any and also to conceive which model agreed better with the test results.

5.2.1. Model-1

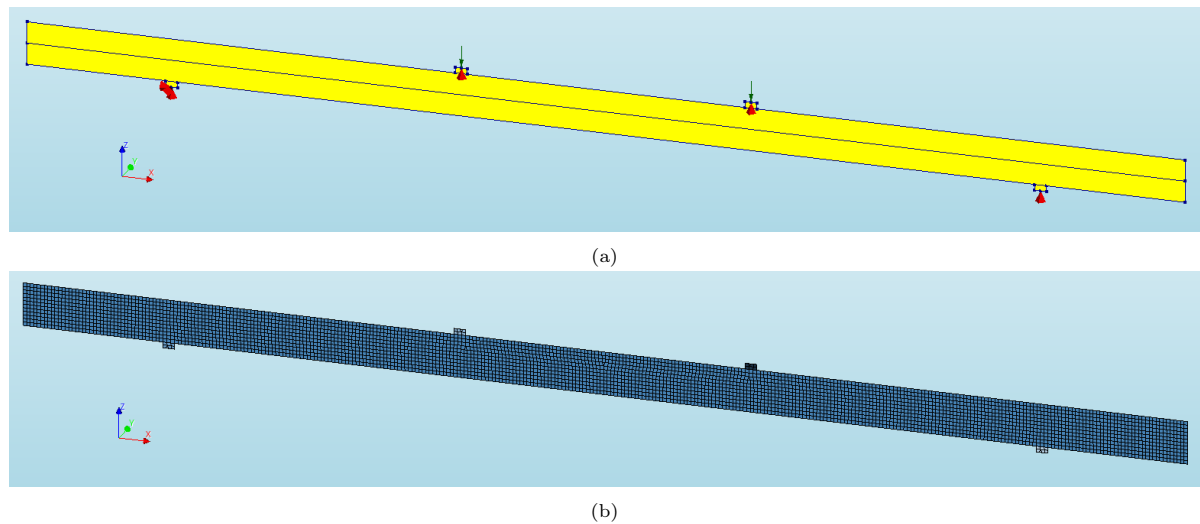


Figure 5.3: (a) Finite element model and (b) Finite element mesh of Model-1

While the model was two-dimensional in essence, the model was constrained in a three-dimensional space due to the usage of curved shell elements. The geometry of the model is shown in figure 5.3a. The loads and supports were modelled as close to the experiment as possible with a rectangular steel block of 10x5 mm cross-section. The left support was constrained with all possible translations, while only the vertical translation was constrained for the right support. Rotation is unconstrained at both support locations. The other boundary condition, a vertical load, is applied as prescribed displacement in the vertical direction on both the middle steel sections. Initially, a reference board was chosen that showed ideal bending behaviour similar to and was representative of the majority of the boards, its geometrical and material properties were applied to the model as shown in table 5.2. Self-weight of the steel sections and the board is neglected in the numerical model.

Table 5.1: Finite element type

Finite element	CQ40S	CT30S
Type	8-node quadrilateral isoparametric curved shell element	6-noded triangular isoparametric curved shell element
DOFs per element	40	30
Interpolation scheme	Quadratic	Quadratic
Integration scheme	2x2x3	3x3
Shape dimension	3D	3D
Topological dimension	2D	2D
Stress components	$\sigma_{xx}, \sigma_{yy}, \sigma_{zz}, \sigma_{xy}, \sigma_{xz}, \sigma_{yz}$	$\sigma_{xx}, \sigma_{yy}, \sigma_{zz}, \sigma_{xy}, \sigma_{xz}, \sigma_{yz}$
Shear deformation	Yes	Yes
Average element size [mm]	10	2.5
No. of elements	4016 ^a	7 ^b

^a Steel, Azobé(top) and Azobé(bottom) have 24, 1997 and 1995 elements respectively

^b Steel and Azobé(bottom) have 4 and 3 elements respectively

The sheet-pile board was modelled edgewise as two equally thick layers along its depth. This allowed the assignment of distinctive tensile and compressive yield strengths since the board undergo compressive yielding much before the part of the board subjected to tensile stresses fail. In this iteration, since only one board was tested, the orthotropic nature does not play a major role in the load distribution and hence was neglected while modelling. Two variations of this model were numerically tested: one with isotropic elasticity for the part of the beam that is subjected to tension due to bending (A) and the other with isotropic plasticity (B). The Von Mises yielding criterion was chosen since it is a simplification of the Hill anisotropic model that suits the hardwood board better.

Table 5.2: Material properties assigned in the FE model

Element	Material model	MOE [MPa]	Poisson's ratio [-]	Yield stress [MPa]
Steel	Linear elastic isotropic	210000	0.3	-
Azobé (Top)	Isotropic plastic - Von Mises	11500	0.3	45
Azobé-A (Bottom)	Linear elastic isotropic	11500	0.3	-
Azobé-B (Bottom)	Isotropic plastic - Von Mises	11500	0.3	70

A structural non-linear analysis was run with a prescribed displacement of 70 mm. In order to understand the progressive load-displacement relation, the displacement is applied as load steps at a continuous interval of 2mm. For the non-linear analysis, only the physical non-linearity was included, and the maximum number of iterations was set to 100. The convergence tolerances for force and displacement were set to 0.01, and they had to be met simultaneously. A regular Newton-Raphson iterative method was used for the solution process.

Table 5.3: Characteristics of iterative scheme

Iterative scheme	Max. no. of iterations	Convergence norms used	Convergence tolerance	On no convergence	Step size
Regular Netwon-Raphson	100	Displacement Force	0.01	Terminate	2 mm

5.2.2. Model-2

As shown in figure 5.4a, the same model was attempted to be recreated using layered shell elements in a refined manner. To reduce the computation time as the number of elements kept increasing, and since the test setup was symmetrical, only half of it was modelled. The line support on the left side was constrained for translation in the global Y and Z directions while the edge connecting the symmetrical half of the model was constrained for rotation about the Y axis and translation along the X direction, as shown in figure 5.4a. The choice of applying the supports directly on the sheets was made to maintain simplicity and the final boundary condition, the vertical load, was applied through a steel bar since applying it directly onto the board gave rise to unexpected load distribution along the width of the board also giving rise to the singularity at the tip of the edge load.

The sheet-pile board was modelled flatwise with layered shell elements. It was assigned with two equally thick layered shells similar in essence to Model-1. Four different iterations of the model were tested, A and B, similar to model-1, while the third iteration was with orthotropic yielding characteristics based on Hill anisotropy and the fourth iteration had the tension zone assigned with brittle material properties to simulate cracking. The brittle tensile curve was fed to the elements by means of a total-strain-based cracked model with fixed crack orientation available in DIANA. However in order to find the brittle tensile strength of the boards, the equation 5.1 was adopted from Ravenshorst (2015). The bending moment calculated using this formula is usually an underestimation, but still a close enough value to the actual bending strength of the material. Hence, by using the bending strength and compression

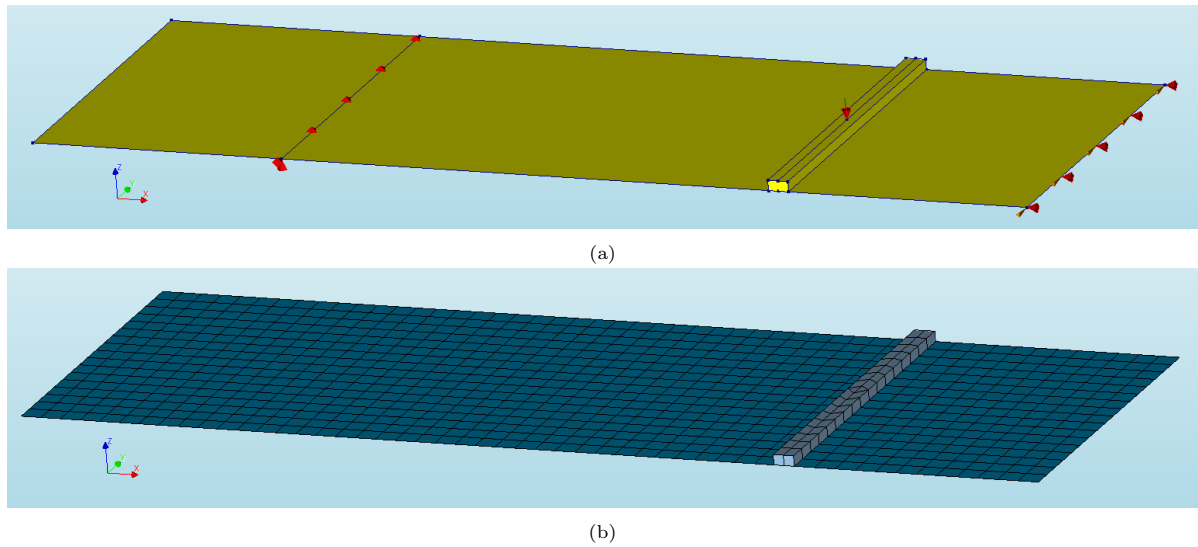


Figure 5.4: (a) Finite element model and (b) Finite element mesh of Model-2

Table 5.4: Finite element type

Finite element	CQ40L	CHX60
Type	8-node quadrilateral isoparametric layered shell element	20-node isoparametric solid brick element
DOFs per element	40	60
Interpolation scheme	Quadratic	Quadratic
Integration scheme	2x2x3	3x3x3
Shape dimension	3D	3D
Topological dimension	2D	3D
Stress components	$\sigma_{xx}, \sigma_{yy}, \sigma_{zz}, \sigma_{xy}, \sigma_{xz}, \sigma_{yz}$	$\sigma_{xx}, \sigma_{yy}, \sigma_{zz}, \tau_{xy}, \tau_{xz}, \tau_{yz}$
Average element size [mm]	10	10
No. of elements	1344 ^a	40 ^a

^a Azobé and steel load-roller are modelled with CQ40L and CHX40 elements respectively

strength values obtained from the experimental tests, the tensile values can be computed using the same formula whilst this will result in a slight overestimation of the tensile strength. This tensile value however applied only in the case of brittle crack and hence not used in models B and C. Figure 5.5 shows the stress distribution at the failure for a timber specimen that is tested flatwise and explains how the bending strength obtained from the experimental tests is approximated in the calculation.

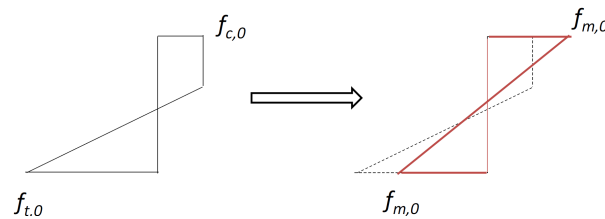


Figure 5.5: Stress distribution at failure for a timber specimen subjected to three-point bending test. The real stress distribution (Left) and the bending strength are calculated using the formula 5.1 (Right). Source: Ravenshorst (2015)

$$f_{m,0,cw} = \frac{f_{c,0} \cdot (3f_{t,0} - f_{c,0})}{f_{c,0} + f_{t,0}} \quad (5.1)$$

where,

$f_{m,0,cw}$ is the calculated bending strength of the material along the grain;

$f_{c,0}$ is the compressive strength of the material along the grain;

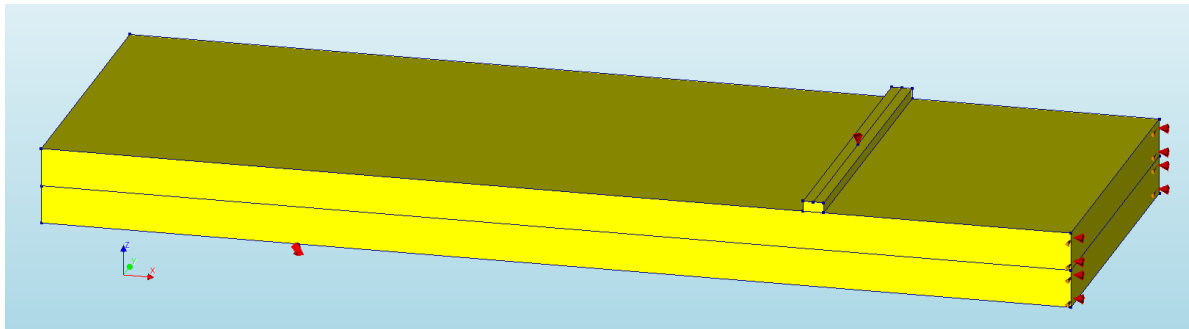
$f_{t,0}$ is the tensile strength of the material along the grain.

Table 5.5: Material properties assigned in the FE model-2&3

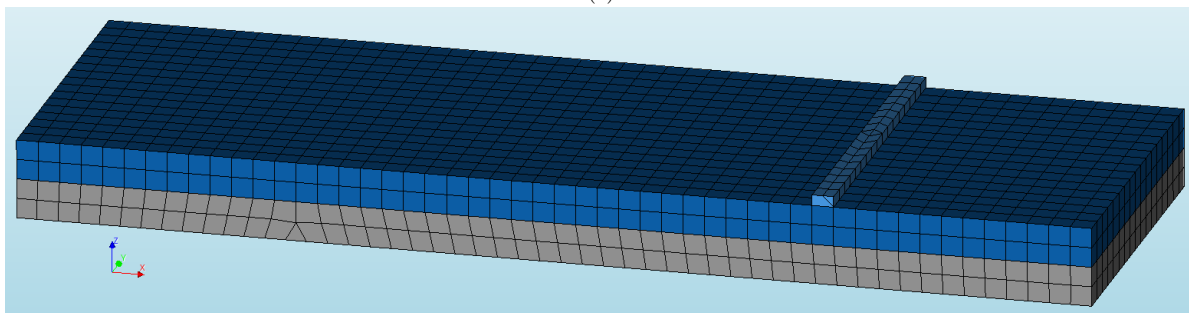
Element	Material model	MOE _x [MPa]	MOE _y [MPa]	Poisson's ratio [-]	Yield stress [MPa]
Steel	Linear elastic isotropic	210000	210000	0.3	-
Azobé-A & B (Top)	Isotropic plastic - Von Mises	11500	11500	0.3	45
Azobé-C & D (Top)	Orthotropic plastic - Hill	11500	1500	0.3	45
Azobé-A (Bottom)	Linear elastic isotropic	11500	11500	0.3	-
Azobé-B (Bottom)	Isotropic plastic - Von Mises	11500	11500	0.3	70
Azobé-C (Bottom)	Orthotropic plastic - Hill	11500	1500	0.3	70
Azobé-D (Top)	Linear isotropic brittle	11500	11500	0.3	110 ¹

¹ Calculated tensile strength for brittle cracking

5.2.3. Model-3



(a)



(b)

Figure 5.6: (a) Finite element model and (b) Finite element mesh of Model-3

In the next iteration of the model, the layered shell elements were replaced by 3D brick elements and topologically three-dimensional shapes were introduced into the model, as shown in figure 5.6a. In essence, the geometry of model 3 was a combination of the flat-wise and edge-wise representation of the previous models. Similar to model 2. three iterations of the model were created with different material properties as shown in table 5.5.

Table 5.6: Finite element type

Finite element	CTP45	CHX60
Type	15-node isoparametric solid wedge element	20-node isoparametric solid brick element
DOFs per element	45	60
Interpolation scheme	Quadratic	Quadratic
Integration scheme	4x2	3x3x3
Shape dimension	3D	3D
Topological dimension	3D	3D
Stress components	$\sigma_{xx}, \sigma_{yy}, \sigma_{zz}, \tau_{xy}, \tau_{xz}, \tau_{yz}$	$\sigma_{xx}, \sigma_{yy}, \sigma_{zz}, \tau_{xy}, \tau_{xz}, \tau_{yz}$
Average element size [mm]	10	10
No. of elements	34 ^a	3416 ^b

^a Steel and Azobé(bottom) have 17 elements each

^b Steel, Azobé(top) and Azobé(bottom) have 16, 1717 and 1683 elements respectively

5.2.4. Results

The load-displacement graph resulting from each of the iterations is compared with that of the carried-out experimental test in figure 5.7. For consistency's sake, for model-1, the displacement value is considered at the bottom node exactly at mid-span, for model-2, the value is obtained at the mid-point of the edge that runs along the mid-span, and for model-3, the value is obtained at the midpoint of the bottom edge at the mid-span. These values, in theory, should be comparable with the displacement value of the experiment as it is the average of both lasers.

All the A, B and C graphs show similar behaviour in the purely elastic region in terms of stiffness in the linear elastic region and the redistribution of compression stresses. The resulting cross-sectional stress distribution at the mid-span of each board is shown in figure 5.8a. As the loading increases, the compressive stress gets redistributed (figure 5.8b) due to yielding in the top compressive zone of the board at mid-span. This results in the curve that follows the linear-elastic region in the load-displacement curve. For models that were set up with no yielding in the tensile zone (models 1A, 2A, 3A), the curves continue in a linear fashion with reduced stiffness while the B and C models, even though continue linearly, exhibit close to zero stiffness. The latter group show better similarity in terms of behaviour compared to that of the experimentally tested specimens. Models 2D and 3D were designed not to be exactly in line with the experiments but to be used in the load-sharing factor model and the post-linear behaviour, especially for 3D would accurately represent the failing of the boards once the peak load is reached.

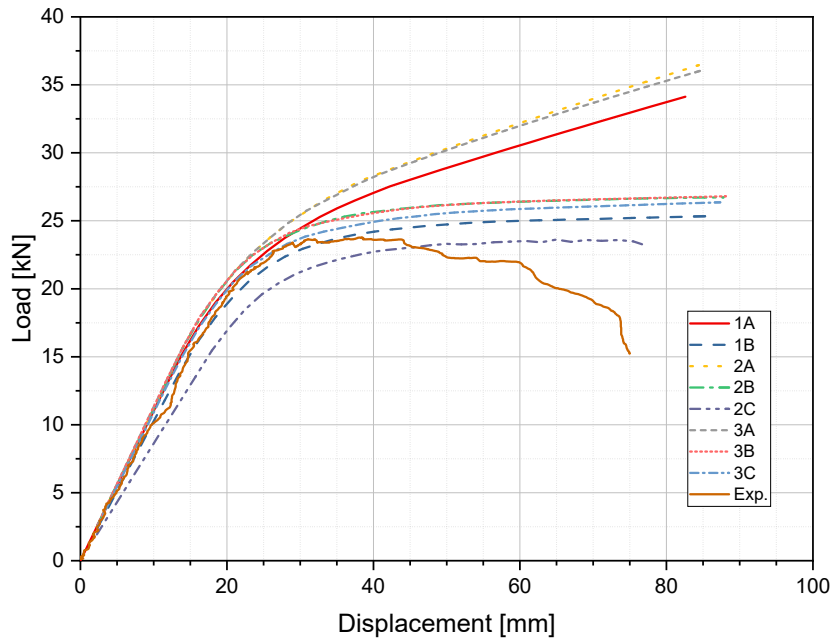


Figure 5.7: Load-displacement curve of the numerical models

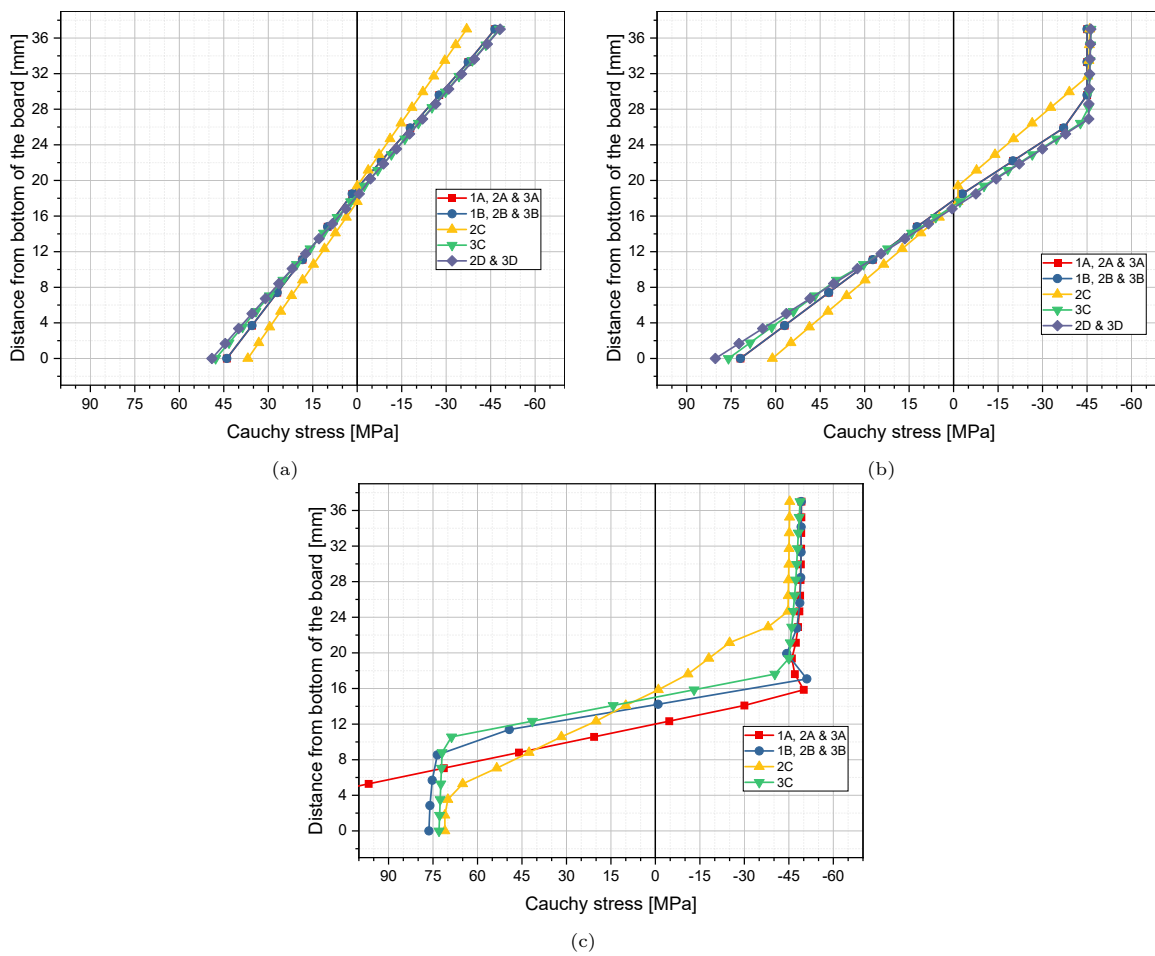


Figure 5.8: Longitudinal stress distribution at mid-span in the Azobé board when the vertical prescribed displacement is (a) 12mm (b) 20mm (c) 50mm

5.2.5. Discussion

The iterations of the material models were created to understand the pros and cons of modelling timber using DIANA since structural timber as a material is not predefined in the software application and adopting different failure models was case specific and for replicating a four-point bending test, this had to be worked out and assessed on a trial and error basis. Model A was easily predictable to not accurately depict the actual material only served as a reference to build the other models.

The Von Mises or the Hill criterion being used in the modelling of the compression behaviour of the top part of the sheet-pile has its own shortcoming. The compressive strength is accurate and the material starts yielding as shown in figure 5.8b, while the element subjected to the yielding compressive stress continues to carry the load instead of undergoing failure due to compression as it was seen in section 4.9, in which the post-compression yielding behaviour of timber is explained.

With regard to the zone under tensile stresses, models B and C allow for yielding in the tensile zone with Von Mises and Hoffman criterion. In model D, this zone is accurately modelled as a brittle material. However, the post-failure behaviour of the model is completely misinterpreted due to the stresses being redistributed in the compression zone once the tensile zone cracks as shown in figure 5.8c. This misinterpretation does not play any significant role, especially in a system with multiple sheets modelled to calculate the load sharing factor since the point of focus, in that case, would be the peak load and the failure of the weakest beam and not the post-failure behaviour.

5.3. FE modelling - Sheet-pile wall system

From the single-board models, multiple-board/sheet-pile wall system models were developed in order to assess their load-sharing factor. According to Van de Kuilen and Blass (2005), the Load-Sharing Factor (LSF) can be defined as the ratio of the characteristic value of the sheet-pile wall to the characteristic strength of individual boards obtained from the analysis.

5.3.1. Characteristic bending strength

The bending strength of individual boards subjected to experimental tests had a mean value of 78.8 MPa with a standard deviation of 16.7 MPa. Using these values the lower 5th percentile value or the characteristic bending strength value is computed as 51.4 MPa. The ideal method to find the LSF would be performing a Monte Carlo simulation as suggested in section 5.3.4. Anyhow due to the timeline of this thesis, about five combinations of five sheet-pile walls systems are chosen from the material properties of three individual boards whose bending strength values are below the characteristic bending strength value, analyzed and the mean bending strength value of these five sheet-pile walls are expected to be close to the characteristic value that would be obtained through Monte Carlo simulation. In order to perform this analysis, three boards are chosen and their material properties are calibrated so as to obtain a numerical $f - d$ curve up to the peak load similar to that of the tests as shown in figure 5.9.

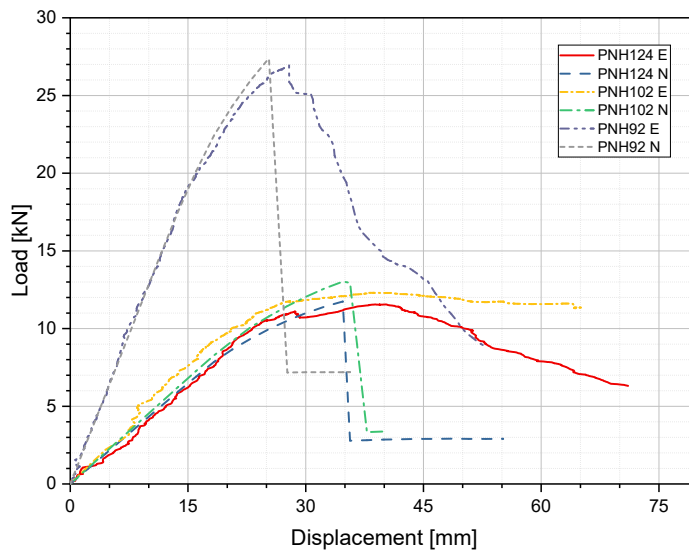


Figure 5.9: Calibrated $f-d$ curves of the board used for LSF determination in comparison with the experimental results (E- Experimental, N- Numerical).

5.3.2. Using brick elements

Model-3D was used as a basis to model multiple sheets held together by tongue and groove joints. The three-dimensionally modelled tongue and groove joint is shown in figure 5.11. The bottom vertical surfaces of the joint were detached using the disconnection elements available in DIANA, while the other surfaces in the joint were modelled with rigid connection elements, with translations connected along the y and z-axes and rotations connected about the x and z-axes. This boundary condition can be justified for this specific case, where the bottom vertical edges remain disconnected and move further apart when the board undergoes bending. Meanwhile, all the other edges either remain in contact and the top part of the board undergoes compression.

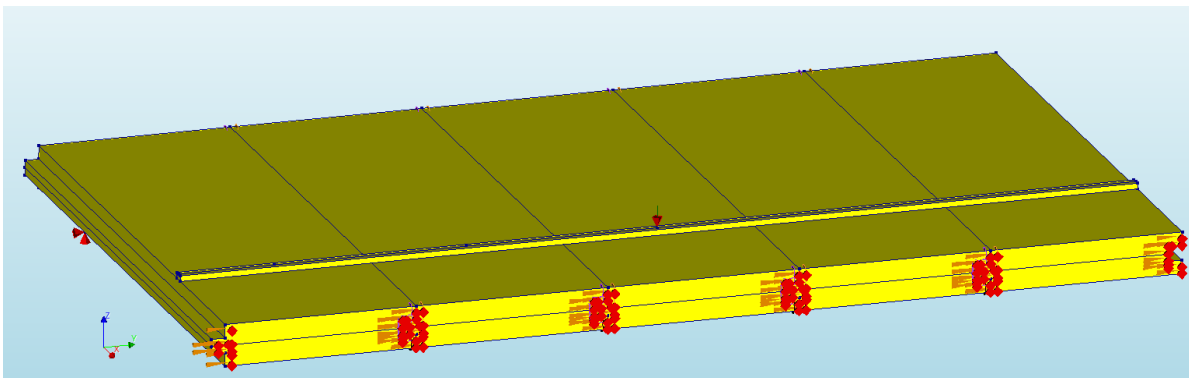


Figure 5.10: Sheet-pile wall system of 5 boards based on model-3D

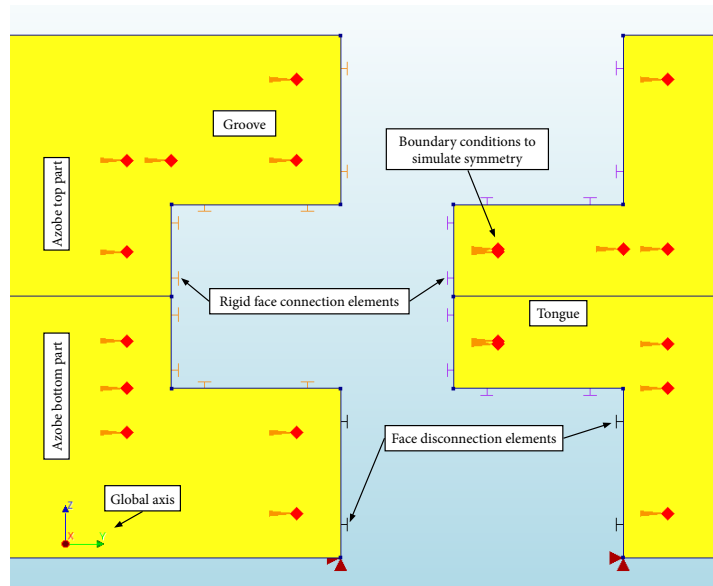


Figure 5.11: Detail of the tongue and groove joint modelled in the 3D sheet-pile wall system

5.3.3. Load-sharing factor

In order to get an idea about the LSF, some of the worst possible configurations that can be considered during a Monte Carlo simulation for a five-sheet-pile wall system that can result in the lowest possible bending strength values are considered. Using the three boards that were calibrated in section 5.3.1, five combinations were made by mixing and arranging them as a five-sheet-pile wall system. These sheet-pile walls were then assessed for their load-displacement curves and their corresponding bending strengths were calculated. This value was then divided by the characteristic bending strength of individual boards obtained from the experimental tests. The $LSF_{approx.}$ varied between 1.13 and 1.15. These values lie close to the numerical LSF value of 1.19 obtained by Van de Kuilen and Blass (1999), considering the fact that only sheet-piles with bending strength lower than the characteristic value were chosen. For one of the configurations in which out of the three boards that were considered, the strongest board (P) and the weakest board (Q) had an arrangement of PQPQP, the stress distribution across the depth at the mid-span tuned out exactly as expected as shown in figure 5.12.

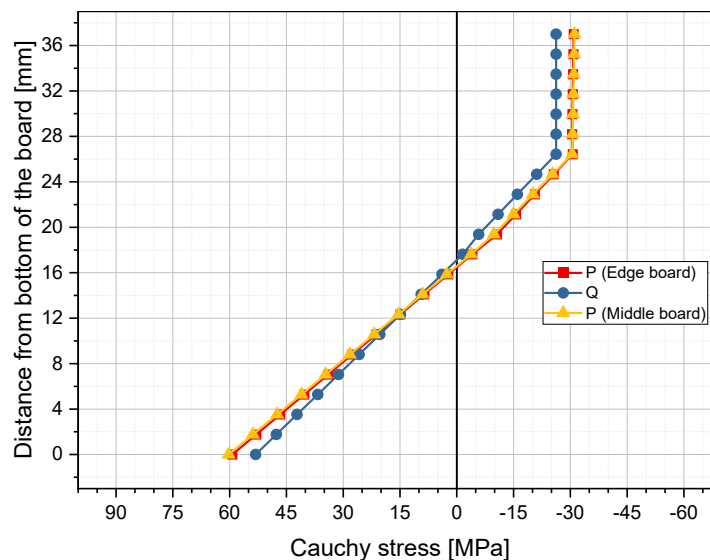


Figure 5.12: Stress distribution at the mid-span for five sheet-pile wall system PQPQP just before tensile brittle cracking

5.3.4. Recommendation

The LSF can be made more accurate by conducting a Monte Carlo simulation. In order to do this, about 40 sheet-pile boards need to be picked at random because of the huge sample size available from the experimental test results. These boards need to be carefully calibrated with their respective material properties along with their dimensions so that the numerical and experimental $f - d$ curves or the stress-strain curves match with each other similar to how it has been done in section 5.3.1. These calibrated material properties of the 40 sheets can be picked at random to form a sheet-pile wall system consisting of a variable number of boards such as 3, 5, 10, etc. The resulting sheet-pile walls can be numerically tested similar to how it has been done for 3 wall systems in section 5.3.3 to obtain their bending strengths. By analyzing the distribution of the resulting bending strengths, the characteristic bending strength of the sheet-pile wall can be obtained. Dividing this value by the characteristic bending strength of individual boards obtained from the test results would yield an accurate LSF. Though this elaborate process has not been performed due to time restrictions and because DIANA does not have a built-in option to run a Monte Carlo simulation, the feasibility and the details involved in each of these steps have been performed in this thesis. It is also important to note that increasing both the number of samples included in the simulation and the number of sheet-pile wall systems generated using these samples would certainly increase the accuracy of the LSF obtained.

Conclusion and Recommendation

6.1. Research questions

- What are the types of decay and decay patterns observed in used Azobé sheet-piles?

Since each sheet-pile was cut into two pieces, any pattern that existed with respect to the decay was studied both at the board level as well as the sheet-pile level. At the board level, this was done through the visual decay analysis and the RPD test, while on the sheet-pile level, in order to clearly convey the difference between the top and bottom boards, every test result is relevant, especially the four-point bending test since four different configurations were used. A strongly occurring pattern where the top board appeared to be less decayed compared to the bottom boards was observed during the visual decay analysis, and this resulted in most of the top boards gaining a lower VDS compared to their bottom counterparts. Anyhow, no other test results backed this up. In fact, the other test results contradicted this slightly by showing better load-bearing properties for the bottom compared to the top boards. The only test that could quantitatively explain the decay pattern at the board level was the RPD test, with the resistance measure value. However, no clear difference between different zones within the board was established and the small differences in the local density did not affect the local stiffness or strength in an evident manner.

The tension behaviour of the sheet-pile was assumed to be the decisive factor for failure and that it obeys Hooke's law and fails by brittle cracking. With respect to the boards being four-point bending tested, the bending strength of the E-side-up boards that had similar stiffness was considerably higher. This could be attributed to the much higher tensile strength of the non-decayed (W) side compared to the heavily decayed (E) side, thus proving the assumption right.

- Can the Azobé sheet-piles be reused, and how can they be graded?

Strength grading of fresh, sawn timber elements needs to be performed according to the grading procedure stated in NEN-EN 14081-1 (2019). However, in order to analyse how the decayed sheet-piles can be reused, their mechanical strength properties were determined using the tests performed during the study. By adjusting these mechanical strength properties to the reference moisture content of 12% and reference depth of 150 mm from the wet MC at which the sheet-piles were tested at a thickness/depth range of 34 to 41mm, they were allotted a strength class of D50. Specifications for Azobe by vendors and grading companies reflect a strength class of D70 in general. In the study by Ravenshorst (G. J. P. Ravenshorst, 2015), the optimization of Azobe specimens based on their characteristic strength values resulted in equal distribution under the D80 and D60 strength classes. Hence, the decayed Azobe sheet-piles can be used in the redesign of the wall system by considering strength values specified by NEN-EN 384 (2022) for the strength class D50.

- How is decay analyzed and modelled in structural elements made of hardwood?

The study of decay in timber, especially hardwood is not a well-explored track of forensic investigation. Although the type of degradation in hardwoods can be learned and the impact these mechanisms have

on the mechanical strength of the material can be analyzed, the type of application determines the type of loading the specimen undergoes, and timber being an orthotropic plastic material required during the thesis, careful integration of all of these factors together. Though compression and fracture energy in hardwood have been studied in detail using numerical analysis, modelling the overall material behaviour required a series of steps that started with the discretisation of the specimen based on the loading that it would be subjected to. The tensile behaviour of the material was accurately able to be applied to the model, but due to the discretized approach, the post-peak behaviour is not accurate. This was ignored since the model was intended to be used only for the load-sharing factor calculation which does not take into account the post-peak behaviour but only the peak and the load-bearing properties up to it. On the other hand, using the Hill criterion to model the compression behaviour of the material allowed the elements that are subjected to compressive stress equal to the compressive strength to withstand loading continuously without failure which is an inaccurate representation of the bilinear compression behaviour obtained in the experimental tests.

- Can the clear correlation that is observed between bending strength, and static and dynamic bending modulus in unused hardwood sheet-piles be expanded to decayed ones?

The first and foremost aspect to consider when differentiating the decayed sheet-piles from freshly sawn ones is the difference in the physical dimension and geometry caused by the decay. The first difference is the striped decay, which was included in the thickness calculation. This led to the underestimation of the density, bending strength and even static and dynamic MOE. Since the stripes are thin (<3.5 mm wide), there was no straightforward way to exactly calculate the actual volume of the boards. However, this could have been done using an x-ray or CT scan, and the difference in volume could then be included as a multiplication factor in the final results. The second difference is the decay of the tongues and grooves that result in an unsymmetrical cross-section across the thickness of the boards. This would also result in an underestimation of the strength and stiffness values due to the contribution of the tongue and groove to the moment of inertia value as explained in the thesis. The difference in the dynamic and static MOE values obtained is high compared to those from the literature. While several factors associated with the difference in the static MOE values can be stated, it is evident that the difference is quite big and unusual compared to fresh Azobé members.

- What is the applicability of the material model in LSF analysis?

Numerical modelling of timber specimens subjected to uniaxial bending needs to take into account the orthotropic elastic and plastic properties and the difference in behaviour when subjected to tensile and compressive stresses (bilinear compression curve vs brittle tensile failure). Though none of the models was perfectly accurate to explain these properties, the closest model (model 3D) satisfied the requirements for the model to be used in the load-sharing factor analysis: linear elastic properties with the correct cross-sectional stress distribution, compressive stress redistribution, brittle tensile failure occurring at the peak load. The analysis of the load-sharing factor was not performed through experimental tests by testing sheet-pile walls made of multiple sheet-piles, but was demonstrated by means of numerical modelling. An experimental test would require an entirely new setup and more used sheet-piles. However, by combining past literature in which the load-sharing analysis through experiments was performed, and integrating it with the bending strength obtained through the experimental tests, the load-sharing factor prediction has been performed and its feasibility has been proved in this thesis.

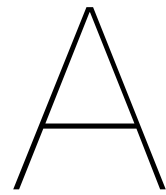
- Can the decay in tropical hardwood that affects its load-bearing capacity when used as a sheet-pile material be predicted using non-destructive methods? How necessary are the destructive tests?

Owing to multiple advantages such as safety, cost-effectiveness, repeatability, in-situ testing and preserving structural integrity when non-destructive testing, the aim of the thesis was to establish a detailed relationship between NDTs and DTs and analyze them numerically, so as to find the feasibility. Though the lack of detail and accuracy was the main concern with respect to NDTs, a systematic method was developed, so that every aspect of the board was recorded using NDTs as well as DTs which can be useful during the analysis. By comparing the obtained data with the literature and also demonstrating its applicability in the numerical analysis, the basic understanding is that the non-destructive tests can provide an accurate estimation of the load-bearing properties of the sheet-piles. However, an analysis solely based on non-destructive tests would practically be impossible.

In this case, where a certain number of boards were removed to be tested from the site, the remaining structure on site can be analyzed only using non-destructive tests in order to assess their life span and load-bearing strength and stiffness. However, to the discrepancies observed during the data interpretation from the test results and also with respect to the literature, this process needs to be carried out with a highly conservative approach due to the risk involved.

6.2. Limitations

Since the research's goal was to obtain as much data that could make the prediction of mechanical properties of the sheet-piles possible, using a straightforward method, other details related to the decay, such as what factors cause more decay in the E-side compared to the W-side, is there a difference in the local density at a different location within the board, the background behind the formation of the striped decay patterns and the distinctive difference between factor causing stripe and hold decay are not explored in detail. One factor that could explain the decay in the sheet-piles better is the three-dimensional density function that can be obtained by X-ray or CT scanning of the specimens. This density function would proportionally indicate any local flaws due to the decay that could have occurred. This data can then be cross-checked with the failure pattern in the bending test of each board. However, this elaborate process, which could undoubtedly explain any deviation of the experimental results from the general trendline was not performed due to restrictions with time and availability. While the prediction of the load-sharing factor was performed, the material model was not capable of exhibiting the exact behaviour of the sheet-piles in a four-point test. Also, though the load-sharing factor was predicted using the five weakest possible combinations of sheet-pile boards, the accurate characteristic load-sharing factor can be determined by performing a Monte Carlo simulation using the results from the experimental tests.



Appendix - A

This chapter presents the superficial conditions of sheet-piles board that belong to their respective Visual Decay Scores.

A.1. Visual decay scores

A.1.1. VDS1

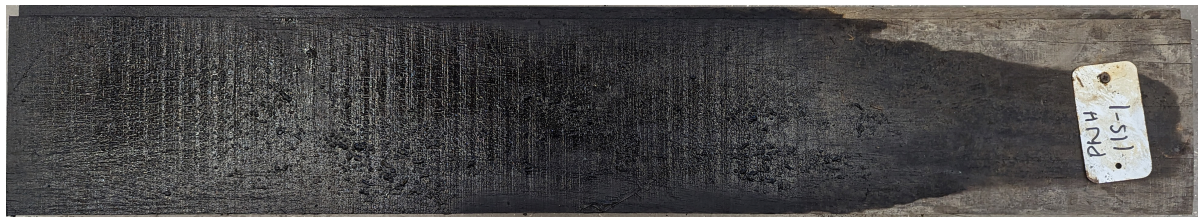


(a)



(b)

Figure A.1: PNH52-1 (a) Side W (b) Side E



(a)



(b)

Figure A.2: PNH152-1 (a) Side W (b) Side E

A.1.2. VDS2



(a)



(b)



(c)

Figure A.3: PNH97 (a) Side W (b) Side E (c) Longitudinal section showing the striped decay

A.1.3. VDS3



Figure A.4: PNH34 (a) Side W (b) Side E (c) Part of groove in side E decayed and chipped off

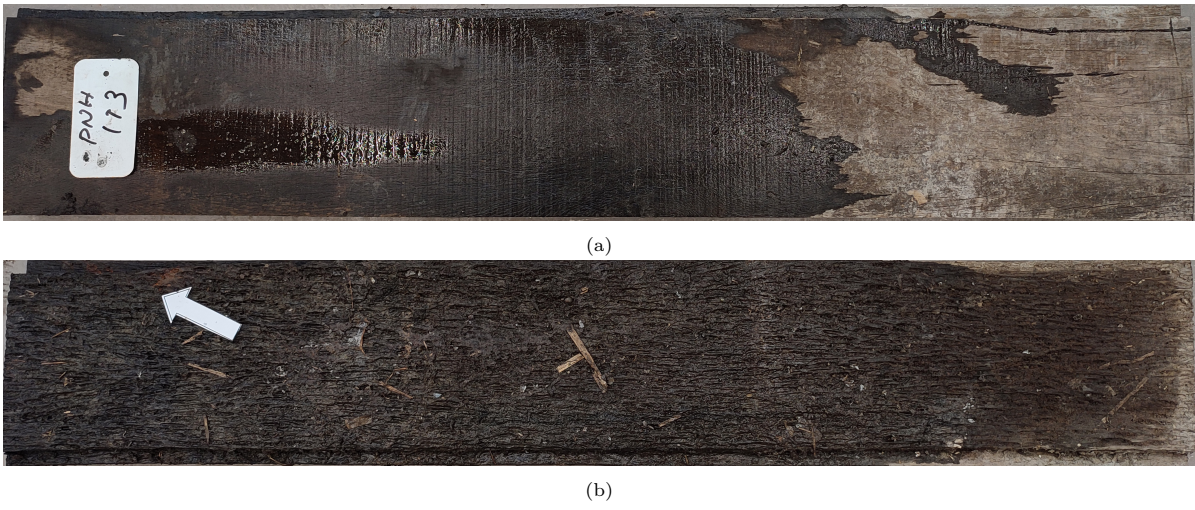
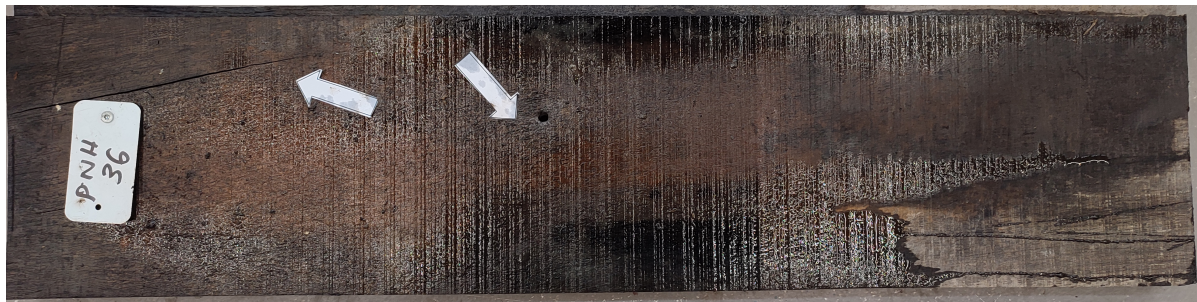


Figure A.5: PNH113 (a) Side W (b) Side E

A.1.4. VDS4



(a)



(b)

Figure A.6: PNH36 (a) Side W (b) Side E



(a)



(b)



(c)



(d)

Figure A.7: PNH94 (a) Side W (b) Side E (c) Decay holes on side W (d) Decay holes on side E

A.2. Data entry sheet

76

	Date 2/11	Sheet ID	PNH - 11001
--	---	----------	---

Initial remarks	<div style="display: flex; justify-content: space-around;"> <div style="border: 1px solid black; padding: 5px; width: 45%;">W \leftarrow</div> <div style="border: 1px solid black; padding: 5px; width: 45%;">E \rightleftarrows</div> </div> <p style="text-align: center; color: red; font-size: 1.2em;">Tongue 100%. Intact Groove intact</p>
-----------------	---

	L	R		T	M	B		
Length	1002.5	1002.5	mm	Breadth	171	174	174	mm
Mass	7310		g	Thickness	37.2	37.8	40	mm
Visual decay score	1/2		1 to 4					

~~Medium~~ Shallow

Acoustic test	Beam No. 11 mm	Frequency 1835 Hz
---------------	--	---

RPD Test	<div style="display: flex; justify-content: space-around;"> <div style="border: 1px solid black; padding: 5px; width: 45%;"> <p style="text-align: center; color: red; font-size: 1.2em;">W</p> <p style="color: red; font-size: 1.2em;">.44</p> <p style="color: red; font-size: 1.2em;">.45</p> <p style="color: red; font-size: 1.2em;">.46</p> </div> <div style="border: 1px solid black; padding: 5px; width: 45%;"> <p style="text-align: center; color: red; font-size: 1.2em;">E</p> <p style="color: red; font-size: 1.2em;">.48</p> <p style="color: red; font-size: 1.2em;">.49</p> <p style="color: red; font-size: 1.2em;">.50</p> </div> </div>
----------	--

4 Point bending	<div style="display: flex; justify-content: space-between;"> <div style="border: 1px solid black; padding: 2px;">Side up W</div> <div style="border: 1px solid black; padding: 2px;">W/E</div> </div> <div style="text-align: center; margin-top: 10px;"> </div> <div style="display: flex; justify-content: space-between; margin-top: 10px;"> <div style="border: 1px solid black; padding: 2px;">Grain angle, alpha 3.5</div> <div>degrees</div> </div>
-----------------	--

Moisture test	Weight of cut specimen Before test 269.4 g 208.4	Day 1 Day 2 Day 3 	
---------------	--	---	--

Figure A.8: Typical filled-in data entry sheet per specimen

A.3. Bending test failure patterns

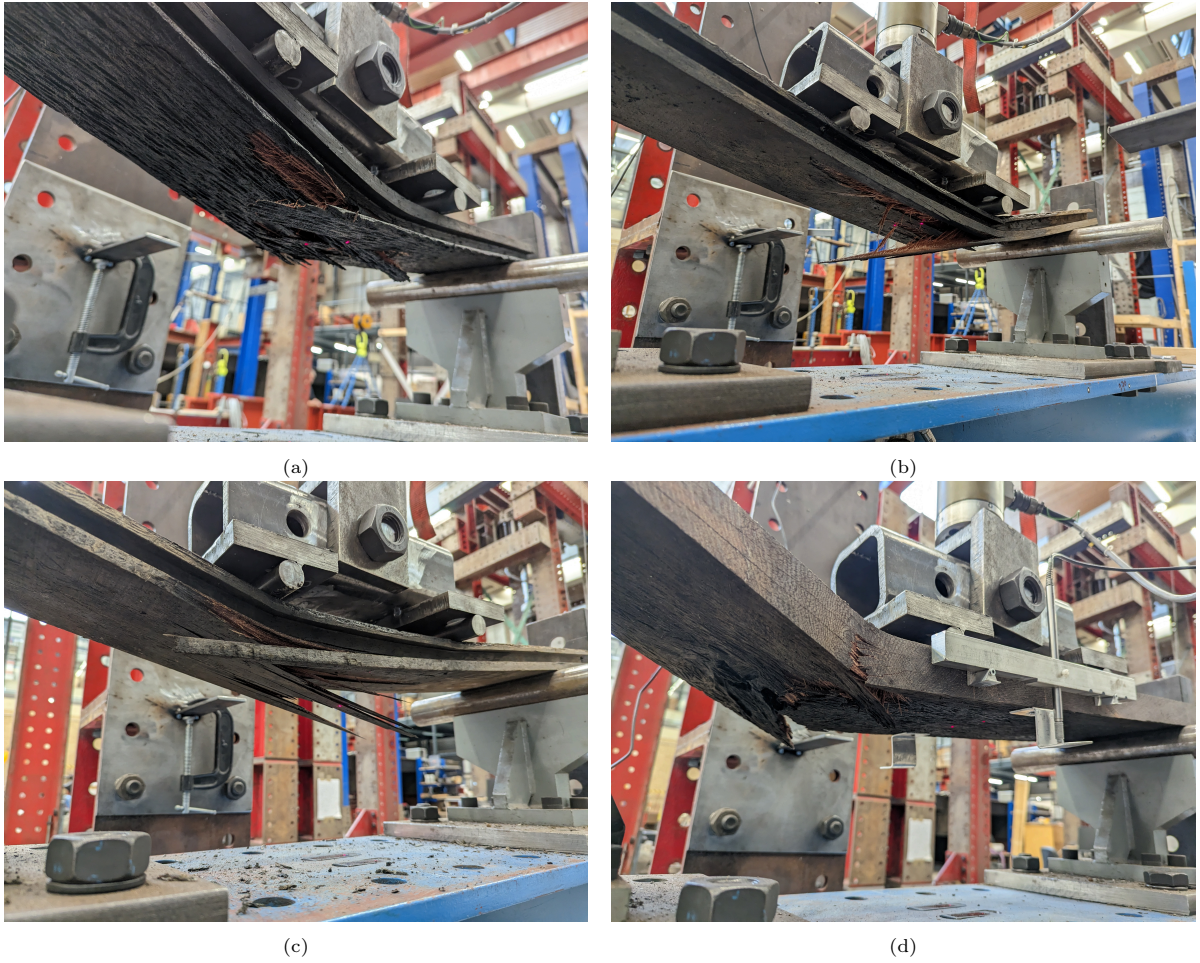


Figure A.9: Four-point bending test failure patterns



(a)



(b)

Figure A.10: Cross grains visible after failure

B

Appendix - B

This chapter explains the validity of the test results obtained from the 9 sheet-pile boards that had their moisture content lower than the fibre saturation point.

B.1. Samples with MC lower than FSP

In figure B.1, it can be seen that the 12% density of the boards whose MC during the test was below the fibre saturation point was well in line with that of other specimens. Also, for these samples, the correlation between the strength and stiffness was in agreement with the range of scattering that can be observed in figure B.1a.

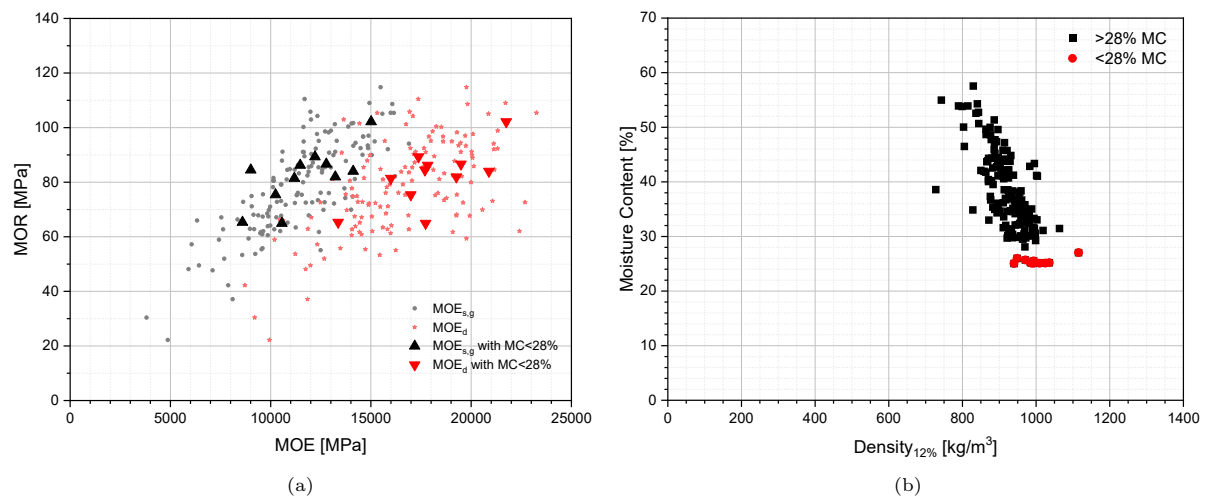
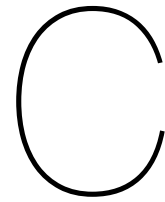


Figure B.1: All samples in comparison with samples with MC < FSP (a) Bending strength vs MOE (b) MC vs 12% MC density



Appendix - C

This chapter includes the Lab safety report that was submitted to the lab supervisor to obtain approval for conducting the experiments.

Step-by-step procedure for all the tests that will be performed in the laboratory. The safety requirements for all these steps are considered and followed. Anyhow, common sense is used when going through something that is not performing as described below or missing in the description.

Tools, equipment, and other things necessary before starting:

1. Safety shoes
2. Heat resistant gloves (up to 105°C)
3. Normal gloves (protection against dust, wooden fibres and sharp edges from the Azobé boards)
4. Mask (protection against dust/ fumes)
5. Mobile phone/ camera to capture pictures
6. Marker, Pencil(s) (coloured), eraser, ruler, protractor/set squared
7. Printed data entry sheets (to draw and fill parameters)
8. Laptop
9. Acoustic and RPD testing device
10. Workstation with organized setup to test multiple specimens
11. Fully moisture saturated Azobé sheets

C.1. Things that could go wrong

Overall

1. The sheet can slip out of hand.
2. Any equipment or the sheet could fall over a person's leg or objects left on the ground.
3. Someone else can create a dangerous situation.

RPD test

4. The drill head may fracture.
5. The drill head may become overheated and emit a burning stench.
6. A small piece of the wood may fly around once the drill has cut through it.

7. Drilling through the floor is possible when there is little space between the Azobé sheet and the floor. If this happens, the drill head or the lab floor may be harmed.

Four-point bending test

8. If the wood is positioned improperly, it may fall off or be crushed.
9. When the load pressure is on, touching the sheet even slightly can result in it getting stuck.
10. Wood fragments may come loose from the sheet and fly off during the test.

Moisture test

11. The lab staff must perform the cutting, however, the dust and wooden bits may fly.
12. When placing the sheets into the oven or taking them out, the oven can get very hot.

Data

13. Experimental data stores in the laptops/ computers can get lost/ corrupted.
14. Data entry sheets can get lost.
15. Data can be misinterpreted.

C.2. Safety precautions

To keep everything safe, it is important that basic steps like wearing the right clothing should be followed. This includes long jeans with safety shoes underneath. In addition, it is necessary to keep a check on the surroundings and have an overview of when other people in the lab are working to detect possible dangerous situations. Also, the walking pathway should be kept free. For the RPD test, there are a few things that should be followed to be safe. Due to the device's built-in safety features, the drill won't protrude when there is no pressure on the nozzle. It is necessary to press the nozzle against the wood while it is operating. When doing so, it should be made sure that there is nothing underneath the Azobé sheet and enough clearance is available between the sheet and the floor. When something feels wrong, the red button should be pressed immediately. Wearing safety goggles is required during drilling. If there are any flying bits of wood, this will help provide protection.

There are no additional concerns to take into account when attentively following the method. Safety may be more important in the four-point bending configuration than in other experiments because it is computer controlled. This implies that when anything occurs, it can only be stopped by a computer. This is the reason why, while the test is going, everyone either sits behind the computer or stays clear of the setup while donning protective goggles. This is because powerful forces are involved in this test. The computer is also positioned at a secure distance. Several saws will be used to cut the pieces so that the moisture content can be assessed. The lab worker is in complete control of all of these. Wearing ear protection and maintaining a safe distance are the only requirements. A temperature of 103°C can be reached while working with the oven. Hence making sure that the gloves are always available on top of the oven is important.

Finally, all of the data is stored on at least two distinct devices to ensure that it cannot be lost due to computer failure. All handwritten materials should also be scanned and stored on paper until the project is finished.

C.3. Test procedure

Preparation

1. The Azobé sheets should be soaked in water at least for 3 weeks in water. Since the water might contain a certain type of bacteria called Legionella Pneumophila, the pH level of the water should be brought down to 3.5 (slightly acidic), in which the bacteria cannot survive. This should be done by mixing calculated amounts of cleaning vinegar with the water.
2. The computer used for the testing procedures should be switched on and logged in with the username ./meet and the password TUD_mt01.

3. After the time spent soaking, the boards inside the metal tank should be removed. Because the Azobé sheets still contain dirt and wood fibres, you should do this while wearing gloves.
4. Only the sheets required for evaluation on the day of the experiment should be taken upstairs to the table.
5. Pictures of all sheets that are to be tested should be captured making sure the sheet IDs are clearly visible.
6. Uncertainties on the surface of the wood like knots, warping, bowing, splits, decay, and visible stripes should be taken note of and captured as pictures.
7. Possible failure mechanisms should be sketched out.

Determination of dimension and volume

8. The sheets from the table should be measured for average sizes of each of the sheets. The length, breadth and thickness of each Azobé sheet should be taken note of. The length of the sheets should be measured two times, on left and right sides of the sheet. For thickness and breadth, three measurements should be taken from each sheet at top, middle and bottom of the sheets along their length. For thickness, the least thickness near the measuring point should be chosen.
9. The tongues and grooves should also be considered for the volume calculation. The sheet piles should then be put on a weighing scale, for the mass to be determined.
10. All these measurements should be taken note of in the data entry sheets.

Acoustic test

11. The case containing the device should be brought from the storage opened and the device should be taken out. The battery level should be checked regularly before and after using the machine and when the charge is low, the battery should be charged.
12. The device should be started by pressing the left and right buttons.
13. The timber grader MTG application should be opened on the laptop as this will help collect and store the data. The USB stick in the case should be plugged into the laptop to have the license for the application verified.
14. In the application, calibrate option should be selected. In order to calibrate the device, the calibrating panel in the case and the unique number mentioned on it should be used. The testing device should be placed against the face of the panel along its length and the yellow button should be pressed for the calibration to take place. This procedure should be repeated every day before commencing testing on the Azobé sheets.
15. In the application, Azobé material should then be selected, and the batch characteristics should be filled in with a general naming format Azobé_Ganesh_acoustic_PNH_date.
16. To begin the test, the start should be pressed on the laptop.
17. The sheet should then be placed on two thin metal stands with wooden slates on top of each of them.
18. While the testing device is being held on one of the faces along the longitudinal direction, the opposite face should be tapped with a hammer as soon as the yellow button on the device is pressed.
19. Once the tapping is done, the resulting graph in the application should be checked for a clear peak. When there are multiple peaks or anomalous graph patterns, the sheet should be tested again.
20. All the good graphs result along with their associated data should be stored in a directory named Ganesh_acoustic_result_date
21. To export the data into a .CSV file, the Export batch option should be selected, and the above mentioned folder name should be mentioned.

22. After the test is done for the day, the device along with the other equipment should be cleaned, and stored away and the result data from the laptop should be copied onto a pen drive.

RPD test

23. A setup should be created in such a way that the Azobé sheets can be clamped onto them with sufficient clearance from the floor level, so that the sheet doesn't move when drilled.
24. Once the sheet is clamped, the testing device should be taken out from its case, checked for battery level and for dust near the nozzle and then firmly held on the flat surface of the sheet. In case the charge is low, the battery should be charged and if there is dust left, it should be cleaned so that the drill head can travel without hindrance.
25. The device is switched on and the rotation speed and drilling speed should be set to 5000 rpm and 25 cm/min.
26. In order to connect the measuring device for the first time, it must be connected to the computer and the red dot at the top of the computer screen must be touched. As soon as the red button is pressed, all of the data will be saved.
27. The angle between the device and the sheet should be maintained close to 90° and the drilling should be started by pressing the red button on the device. When the drilling is complete, the red button should be pressed again.
28. Drilling on the sheets should be performed from left to right. Initially, 6 drilling spots should be chosen on the sheet and distributed equally within its surface area. After performing about 2 weeks of experiments, the results should be analyzed to reconfigure the number of drilling spots on each sheet.
29. During the testing of each sheet, three photos should be taken: an overview photo, and a photograph that is zoomed in from both sides. This will provide a clear picture of the testing locations. Additionally, strange events that occurred throughout the test should be recorded. Before photographing the sheet, make sure that the holes are visible.

Four–point bending test

30. The computer should be turned on and both Re1 and MP3 should be opened.
31. When the pressurising sound is almost completely gone, the computer should be used to power on and set the pressure control in the control box to low. Once the tubes are filled with compressed air, the pressure should then be set to high.
32. To start this test, the setup should be put into rest mode. The pressing part will therefore be 50 mm or so above the support that the sheet is sitting on. (Plus for going up; minus for going down).
33. The Azobé sheet should then be placed in the supports and the side of the sheet facing up is taken note of.
34. The sensor should be checked if it is clean. The underlined CZ should then be pressed to clear the offsets.
35. The yellow triangle should be pressed and the file name should be mentioned as 4_point_Ganesh_sheetID.
36. Start the pressurising procedure, then allow the pressure to drop gradually until it hits the wood. Then, until the failure condition arises in about five minutes, the speed should be reduced, or, in accordance with NEN-408, it should be 0.003 times the estimated thickness of 30 mm, or roughly 0.09 mms⁻¹.
37. As soon as the buildup force decreases and the wood has cracked, the pressurized part should be stopped.
38. The setup should then be returned to the original position the sheet should be taken off the supports.

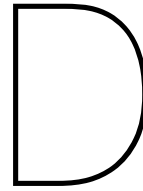
39. Data should be saved by clicking tools→export datafile → browse disk → select XLS 42. The computers should be shut down after it has been saved and the data has been placed on the pen drive.

Grain angle measurement

40. To view the grain angle rip, the Azobé board should be positioned sideways on the table or left inside the 4-point bending test setup.
41. Next, calculate the angle by measuring the angle between the bottom side and the typical tear line in the wood.
42. The tear needs to be sketched as well as photographed.

Moisture content test

43. A piece of wood should be cut off as closely as possible to the crack or rupture generated by the four-point bending test and another piece should be cut off at the other side of the crack, in order to measure the moisture content of the Azobé sheet.
44. Once more, divide these pieces into three portions of equal size. This will show the variation in moisture content across the piece's depth.
45. Once the pieces are cut, they should be numbered based on the following system: pieces close to the crack should be named with *-C* and away from the crack with *-NC* followed by *W* if water facing side, *E* if earth facing side and *M* if middle part.
46. The named pieces should be weighed and then placed inside the oven.
47. After a couple of days, the pieces should be weighed again. This process of weighing should be repeated until the difference between consecutive measurements is less than 0.5% (preferably 0.1%).



Appendix - D

This chapter contains the VBA macro codes used to process the raw data obtained from the experiments conducted in the lab into useful information that can be used for the result calculation.

D.1. RPD test

```
1 Attribute VB_Name = "Module3"
2 Sub RPD()
3 '
4 ' Keyboard Shortcut: Ctrl+Shift+w
5 '
6     Application.ScreenUpdating = False
7 'looping for all sheets in the files
8     For shtcount = 1 To Sheets.Count
9         Sheets(shtcount).Select
10
11 'convert drill and feed measurements from cell to columns
12     Range("A321:A322").Select
13     Range("A321:A322").TextToColumns _
14         DataType:=xlDelimited, _
15         TextQualifier:=xlDoubleQuote, _
16         ConsecutiveDelimiter:=True, _
17         Space:=True, Comma:=True, Space:=True, Other:=True, OtherChar:= _
18         "["
19 'convert columns into rows
20     Columns("A:B").Select
21     Range("A294").Activate
22     Selection.Insert Shift:=xlToRight, CopyOrigin:=xlFormatFromLeftOrAbove
23     Range("C321").Select
24     Range(Selection, Selection.End(xlToRight)).Select
25     Range("C321:OE322").Select
26     Selection.Copy
27     Range("A1").Select
28     Selection.PasteSpecial Paste:=xlPasteAll, Operation:=xlNone, SkipBlanks:= _
29         False, Transpose:=True
30     Application.CutCopyMode = False
31 'create a table
32     ActiveSheet.ListObjects.Add(xlSrcRange, Range("$A$1:$B$393"), , xlYes).Name = _
33         "Table1"
34
35 'filter out zero feed value rows at start
36     Dim lo As ListObject
37     Set lo = ActiveSheet.ListObjects("Table1")
38
39     i = 0
40     For n = 50 To 2 Step -1
41         If lo.DataBodyRange(n, 2) = 0 Then
42             lo.ListRows(n - 1).Delete
43         End If
```

```

44     Next
45 'filter out zero feed value rows at end
46     i = lo.DataBodyRange.Rows.Count
47     For n = i - 1 To 250 Step -1
48         If lo.DataBodyRange(n, 2) = 0 Then
49             lo.ListRows(n + 1).Delete
50         End If
51     Next
52
53 'insert column for Depth
54     Columns("C:C").Select
55     Selection.Insert Shift:=xlToRight, CopyOrigin:=xlFormatFromLeftOrAbove
56     Range("C1").Select
57     ActiveCell.FormulaR1C1 = "depth"
58 'Fill in depth % values
59     i = lo.DataBodyRange.Rows.Count
60     For n = 1 To lo.DataBodyRange.Rows.Count
61         Range("C" & n + 1).Select
62         ActiveCell.FormulaR1C1 = n * 100 / i
63     Next
64
65 'Create a scatter plot
66     Range("H5").Select
67     ActiveSheet.Shapes.AddChart2(240, xlXYScatterLinesNoMarkers).Select
68     Application.CutCopyMode = False
69
70     ActiveChart.SeriesCollection.NewSeries
71     ActiveChart.FullSeriesCollection(1).Name = Range("A1:A1")
72     ActiveChart.FullSeriesCollection(1).XValues = Range("C2:C500")
73     ActiveChart.FullSeriesCollection(1).Values = Range("A2:A500")
74
75     ActiveChart.SeriesCollection.NewSeries
76     ActiveChart.FullSeriesCollection(2).Name = Range("B1:B1")
77     ActiveChart.FullSeriesCollection(2).XValues = Range("C2:C500")
78     ActiveChart.FullSeriesCollection(2).Values = Range("B2:B500")
79
80     ActiveChart.ApplyLayout (8)
81     ActiveChart.ChartTitle.Select
82     ActiveChart.ChartTitle.Text = "RPD"
83     Selection.Format.TextFrame2.TextRange.Characters.Text = "RPD"
84     With Selection.Format.TextFrame2.TextRange.Characters(1, 3).ParagraphFormat
85         .TextDirection = msoTextDirectionLeftToRight
86         .Alignment = msoAlignCenter
87     End With
88     With Selection.Format.TextFrame2.TextRange.Characters(1, 3).Font
89         .BaselineOffset = 0
90         .Bold = msoFalse
91         .NameComplexScript = "+mn-cs"
92         .NameFarEast = "+mn-ea"
93         .Fill.Visible = msoTrue
94         .Fill.ForeColor.RGB = RGB(89, 89, 89)
95         .Fill.Transparency = 0
96         .Fill.Solid
97         .Size = 14
98         .Italic = msoFalse
99         .Kerning = 12
100        .Name = "+mn-lt"
101        .UnderlineStyle = msoNoUnderline
102        .Spacing = 0
103        .Strike = msoNoStrike
104    End With
105
106    ActiveChart.ChartArea.Select
107    ActiveChart.Axes(xlCategory).Select
108    ActiveChart.Axes(xlCategory).MaximumScale = 100
109    ActiveChart.Axes(xlValue).Select
110    ActiveChart.Axes(xlValue).MaximumScale = 100
111    ActiveChart.Axes(xlValue).MajorUnit = 20
112    ActiveChart.Axes(xlValue).MinorUnit = 10
113    Application.CommandBars("Format Object").Visible = False
114

```

```
115 'Delete irrelevant data
116 Range("A1").Select
117 ActiveCell.Offset(0, 3).Columns("A:A").EntireColumn.Select
118 Selection.Delete Shift:=xlToLeft
119
120 Range("D321").Select
121 Range(Selection, Selection.End(xlDown)).Select
122 Range(Selection, Selection.End(xlToRight)).Select
123 Selection.ClearContents
124
125 Range("A1").Select
126
127 'Close the for loop
128 Next
129
130 'looping for all sheets in the files
131
132 For shtcount = 1 To Sheets.Count
133 Sheets(shtcount).Select
134
135 'insert column for Depth
136 Range("C1").Select
137 ActiveCell.FormulaR1C1 = "depth %"
138 Range("D1").Select
139 ActiveCell.FormulaR1C1 = "RA.dh"
140 'Fill in depth and RA.dh values
141
142 Application.AutoCorrect.AutoFillFormulasInLists = True
143 Set lo = ActiveSheet.ListObjects("Table1")
144 i = lo.DataBodyRange.Rows.Count
145
146 Range("D2").Select
147 ActiveCell.FormulaR1C1 = "=[@[drill:]]*0.1"
148
149 'Fill in all the RM values
150 Set lo = ActiveSheet.ListObjects("Table1")
151 m = lo.DataBodyRange.Rows.Count
152 RAdh = WorksheetFunction.Sum(Range("D2:D" & m + 1))
153 H = m / 10
154 RM = RAdh / H
155
156 Sheets(1).Select
157 Range("F" & shtcount).Select
158 ActiveCell.FormulaR1C1 = RM
159 Range("G" & shtcount).Select
160 ActiveCell.FormulaR1C1 = Sheets(shtcount).Name
161
162 'Close the for loop
163 Next
164
165 Range("I1").Select
166
167 Application.ScreenUpdating = True
168
169 'Transposing the RM values
170 Range("F1:J12").Select
171 Selection.Copy
172 Range("L1").Select
173 Selection.PasteSpecial Paste:=xlPasteAll, Operation:=xlNone, SkipBlanks:= _
174 False, Transpose:=True
175 Range("F1:J12").Select
176 Application.CutCopyMode = False
177 Selection.ClearContents
178 Range("L1:W5").Select
179 Selection.Cut
180 Range("F1").Select
181 ActiveSheet.Paste
182
183 Columns("F:O").Select
184 Columns("F:O").EntireColumn.AutoFit
185
```

```

186     Range("I1").Select
187     Application.ScreenUpdating = True
188
189 End Sub
190 Sub RPD_graph()
191
192 'Fill in depth % values
193     Dim lo As ListObject
194     Set lo = ActiveSheet.ListObjects("Table1")
195     i = lo.DataBodyRange.Rows.Count
196     For n = 1 To lo.DataBodyRange.Rows.Count
197         Range("C" & n + 1).Select
198         ActiveCell.FormulaR1C1 = n * 80 / i
199     Next
200
201 'Create a scatter plot
202     Range("H5").Select
203     ActiveSheet.Shapes.AddChart2(240, xlXYScatterLinesNoMarkers).Select
204     Application.CutCopyMode = False
205
206     ActiveChart.SeriesCollection.NewSeries
207     ActiveChart.FullSeriesCollection(1).Name = Range("A1:A1")
208     ActiveChart.FullSeriesCollection(1).XValues = Range("C2:C500")
209     ActiveChart.FullSeriesCollection(1).Values = Range("A2:A500")
210
211     ActiveChart.SeriesCollection.NewSeries
212     ActiveChart.FullSeriesCollection(2).Name = Range("B1:B1")
213     ActiveChart.FullSeriesCollection(2).XValues = Range("C2:C500")
214     ActiveChart.FullSeriesCollection(2).Values = Range("B2:B500")
215
216     ActiveChart.ApplyLayout (8)
217     ActiveChart.ChartTitle.Select
218     ActiveChart.ChartTitle.Text = "RPD"
219     Selection.Format.TextFrame2.TextRange.Characters.Text = "RPD"
220     With Selection.Format.TextFrame2.TextRange.Characters(1, 3).ParagraphFormat
221         .TextDirection = msoTextDirectionLeftToRight
222         .Alignment = msoAlignCenter
223     End With
224     With Selection.Format.TextFrame2.TextRange.Characters(1, 3).Font
225         .BaselineOffset = 0
226         .Bold = msoFalse
227         .NameComplexScript = "+mn-cs"
228         .NameFarEast = "+mn-ea"
229         .Fill.Visible = msoTrue
230         .Fill.ForeColor.RGB = RGB(89, 89, 89)
231         .Fill.Transparency = 0
232         .Fill.Solid
233         .Size = 14
234         .Italic = msoFalse
235         .Kerning = 12
236         .Name = "+mn-lt"
237         .UnderlineStyle = msoNoUnderline
238         .Spacing = 0
239         .Strike = msoNoStrike
240     End With
241
242 End Sub
243 Sub RPD_RM()
244
245     Application.ScreenUpdating = False
246     'looping for all sheets in the files
247
248     For shtcount = 1 To Sheets.Count
249         Sheets(shtcount).Select
250
251     'insert column for Depth
252         Range("C1").Select
253         ActiveCell.FormulaR1C1 = "depth %"
254         Range("D1").Select
255         ActiveCell.FormulaR1C1 = "RA.dh"
256     'Fill in depth and RA.dh values

```

```

257 Application.AutoCorrect.AutoFillFormulasInLists = True
258
259
260 Dim lo As ListObject
261 Set lo = ActiveSheet.ListObjects("Table1")
262 i = lo.DataBodyRange.Rows.Count
263
264 Range("D2").Select
265 ActiveCell.FormulaR1C1 = "=[@[drill:]]*0.1"
266
267 'Fill in all the RM values
268 Set lo = ActiveSheet.ListObjects("Table1")
269 m = lo.DataBodyRange.Rows.Count
270 RAdh = WorksheetFunction.Sum(Range("D2:D" & m + 1))
271 H = m / 10
272 RM = RAdh / H
273
274 Sheets(1).Select
275 Range("F" & shtcount).Select
276 ActiveCell.FormulaR1C1 = RM
277 Range("G" & shtcount).Select
278 ActiveCell.FormulaR1C1 = Sheets(shtcount).Name
279
280 'Close the for loop
281 Next
282 End Sub

```

D.2. Four-point bending test

```

1 Attribute VB_Name = "Module1"
2 Sub fourpoint()
3 Attribute fourpoint.VB_Description = "d"
4 Attribute fourpoint.VB_ProcData.VB_Invoke_Func = "d\n14"
5 '
6 ' fourpoint Macro
7 '
8 ' Keyboard Shortcut: Ctrl+d
9 '
10 'Delete irrelelavant columns
11 Application.Goto Reference:="R1C1"
12 Range("A:A,B:B,H:H,I:I").Select
13 Range("I1").Activate
14 Selection.Delete Shift:=xlToLeft
15 'Convert data to table format
16 Columns("A:E").Select
17 Columns("A:E").EntireColumn.AutoFit
18 Range("A1").Select
19 Range(Selection, Selection.End(xlToRight)).Select
20 Range(Selection, Selection.End(xlDown)).Select
21 Sheets("Filtered").Select
22 lrow = Range("B" & Rows.Count).End(xlUp).Row
23 ActiveSheet.ListObjects.Add(xlSrcRange, Range("$A$1:$E$" & lrow), , xlYes).Name = _
24 "Table1"
25
26 'Filter LS values beyond failure
27 Range("F1").Select
28 Selection.FormulaR1C1 = "ls filtered"
29
30 Range("H1").Select
31 Selection.Formula2R1C1 = _
32 "=INDIRECT(""A"" & (1+MATCH(MAX(Table1[LS01(mm)_Filtered]),Table1[LS01(mm)_Filtered],0)))"
33
34 Range("I1").Select
35 Selection.Formula2R1C1 = _
36 "=INDIRECT(""A"" & (1+MATCH(MAX(Table1[LS02(mm)_Filtered]),Table1[LS02(mm)_Filtered],0)))"
37
38 'Create columns
39 Columns("A:A").Select
40 Selection.Delete Shift:=xlToLeft
41 Columns("F:F").Select

```

```

42 Selection.Insert Shift:=xlToRight, CopyOrigin:=xlFormatFromLeftOrAbove
43 Range("E1").Select
44 ActiveCell.FormulaR1C1 = "LS01"
45
46 'Finding max values
47 Range("H2").Select
48 ActiveCell.FormulaR1C1 = "F_max"
49 Range("H3").Select
50 Selection.FormulaR1C1 = "=MAX(R[-1]C[-7]:R[997]C[-7])"
51 Range("M1").Select
52 ActiveCell.FormulaR1C1 = "0.1"
53 Range("N1").Select
54 ActiveCell.FormulaR1C1 = "0.4"
55 Range("M2").Select
56 ActiveCell.FormulaR1C1 = "F1"
57 Range("N2").Select
58 ActiveCell.FormulaR1C1 = "F2"
59 Range("M3").Select
60 ActiveCell.FormulaR1C1 = "=R[-2]C*R3C8"
61 Range("M4").Select
62 ActiveCell.FormulaR1C1 = "=MATCH(R[-1]C,R2C1:R800C1,1)"
63 Range("M5").Select
64 ActiveCell.Formula2R1C1 = "=INDIRECT(""B"&R[-1]C+1)"
65 Range("M6").Select
66 ActiveCell.Formula2R1C1 = "=INDIRECT(""E"&R[-2]C+2)"
67 Range("M7").Select
68 Selection.Formula2R1C1 = "=INDIRECT(""F"&R[-3]C+2)"
69 Range("L4").Select
70 ActiveCell.FormulaR1C1 = "cell ID"
71 Range("L5").Select
72 ActiveCell.FormulaR1C1 = "S"
73 Range("L6").Select
74 ActiveCell.FormulaR1C1 = "L"
75 Range("L6").Select
76 ActiveCell.FormulaR1C1 = "LS01"
77 Range("L7").Select
78 Selection.FormulaR1C1 = "LS02"
79 Range("M3:M7").Select
80 Selection.Copy
81 Range("N3").Select
82 ActiveSheet.Paste
83 Range("N9").Select
84 Range("G5").Select
85 ActiveCell.FormulaR1C1 = "del_F"
86 Range("F1").Select
87 ActiveCell.FormulaR1C1 = "LS02"
88 Range("H5").Select
89 ActiveCell.FormulaR1C1 = "del_S"
90 Range("I5").Select
91 ActiveCell.FormulaR1C1 = "del_LS01"
92 Range("J5").Select
93 ActiveCell.FormulaR1C1 = "del_LS02"
94 Range("L3").Select
95 ActiveCell.FormulaR1C1 = "F"
96 Range("G6").Select
97 Application.CutCopyMode = False
98 ActiveCell.FormulaR1C1 = "=R[-3]C[7]-R[-3]C[6]"
99 Range("H6").Select
100 Application.CutCopyMode = False
101 ActiveCell.FormulaR1C1 = "=R[-1]C[6]-R[-1]C[5]"
102 Range("I6").Select
103 Application.CutCopyMode = False
104 ActiveCell.FormulaR1C1 = "=RC[5]-RC[4]"
105 Range("J6").Select
106 Application.CutCopyMode = False
107 Selection.FormulaR1C1 = "=R[1]C[4]-R[1]C[3]"
108 'Set number format
109 Columns("G:N").Select
110 Selection.NumberFormat = "0.00"
111 Range("M4:N4").Select
112 Selection.NumberFormat = "0"

```

```

113
114 'Adjust values using exponential smoothening
115
116 Range("I29").Select
117 ActiveCell.FormulaR1C1 = "Alpha"
118 Range("J29").Select
119 ActiveCell.FormulaR1C1 = "1-Alpha"
120 Range("I30").Select
121 Range("I30").Select
122 Selection.FormulaR1C1 = "=0.1"
123 Range("J30").Select
124 ActiveCell.FormulaR1C1 = "=1-RC[-1]"
125
126 Range("E2").Select
127 Application.AutoCorrect.AutoFillFormulasInLists = False
128 Range("E2").Select
129 ActiveCell.FormulaR1C1 = "=[@[LS01(mm)_Filtered]]"
130 Range("E3").Select
131 ActiveCell.FormulaR1C1 = "=R2C3"
132
133 lrow = Range("B" & Rows.Count).End(xlUp).Row
134 Range("E4").Select
135 Selection.FormulaR1C1 = "=R30C9*R[-1]C[-2]+R30C10*R[-1]C[-0]"
136 Selection.AutoFill Destination:=Range("E4:E" & lrow)
137
138 Range("F2").Select
139 ActiveCell.FormulaR1C1 = "=[@[LS02(mm)_Filtered]]"
140 Range("F3").Select
141 ActiveCell.FormulaR1C1 = "=R2C4"
142 Range("F4").Select
143 Selection.FormulaR1C1 = "=R30C9*R[-1]C[-2]+R30C10*R[-1]C[0]"
144 Selection.AutoFill Destination:=Range("F4:F" & lrow)
145
146 'Create scatter plot
147 ActiveSheet.Shapes.AddChart2(240, xlXYScatterLinesNoMarkers).Select
148 ActiveSheet.Shapes("Chart 1").IncrementLeft -57.75
149 ActiveSheet.Shapes("Chart 1").IncrementTop -64.5
150 ActiveChart.SetElement (msoElementLegendRight)
151 ActiveChart.FullSeriesCollection(1).Name = "=Filtered!$C$1"
152 ActiveChart.FullSeriesCollection(1).XValues = "=Filtered!$C$2:$C$1000"
153 ActiveChart.FullSeriesCollection(1).Values = "=Filtered!$A$2:$A$1000"
154
155 ActiveChart.FullSeriesCollection(2).Name = "=Filtered!$D$1"
156 ActiveChart.FullSeriesCollection(2).XValues = "=Filtered!$D$2:$D$1000"
157 ActiveChart.FullSeriesCollection(2).Values = "=Filtered!$A$2:$A$1000"
158
159 'Add two more series to the existing chart
160 ActiveChart.FullSeriesCollection(3).Name = "=Filtered!$E$1"
161 ActiveChart.FullSeriesCollection(3).XValues = "=Filtered!$E$2:$E$1500"
162 ActiveChart.FullSeriesCollection(3).Values = "=Filtered!$A$2:$A$1500"
163
164 ActiveChart.FullSeriesCollection(4).Name = "=Filtered!$F$1"
165 ActiveChart.FullSeriesCollection(4).XValues = "=Filtered!$F$2:$F$1500"
166 ActiveChart.FullSeriesCollection(4).Values = "=Filtered!$A$2:$A$1500"
167 snum = 5
168 ActiveChart.FullSeriesCollection(snum).Name = "=Filtered!$B$1"
169 ActiveChart.FullSeriesCollection(snum).XValues = "=Filtered!$B$2:$B$1500"
170 ActiveChart.FullSeriesCollection(snum).Values = "=Filtered!$A$2:$A$1500"
171
172 ActiveChart.Legend.Select
173 Selection.Left = 131.529
174 Selection.Width = 222.47
175 Selection.Height = 20.75
176 Selection.Top = 104.124
177 Selection.Left = 74.529
178 Selection.Top = 188.124
179 ActiveChart.Axes(xlValue).MajorGridlines.Select
180 ActiveChart.ChartArea.Select
181 ActiveChart.Axes(xlValue).MajorGridlines.Select
182 ActiveChart.PlotArea.Select
183 Selection.Height = 158.801

```

```

184     Selection.Width = 323
185
186     Range("F4").Select
187
188 End Sub
189 Sub corell_coeff()
190
191 'Find the correlation coeffecient
192     colnum = 16
193     rownum = 2
194     Fstart = Range("M4").Value + 1
195     Fend = Range("N4").Value + 1
196     Frange = "A" & Fstart & ":A" & Fend
197     Lsrange = "E" & Fstart & ":E" & Fend
198     ActiveSheet.Range(Cells(rownum, colnum), Cells(rownum, colnum)).Select
199     ActiveSheet.Range(Cells(rownum, colnum), Cells(rownum, colnum)).Value = _
200         Application.WorksheetFunction.Correl(Range(Frange), Range(Lsrange))
201
202     colnum = 17
203     Lsrange = "F" & Fstart & ":F" & Fend
204     ActiveSheet.Range(Cells(rownum, colnum), Cells(rownum, colnum)).Select
205     ActiveSheet.Range(Cells(rownum, colnum), Cells(rownum, colnum)).Value = _
206         Application.WorksheetFunction.Correl(Range(Frange), Range(Lsrange))
207
208     colnum = 15
209     Lsrange = "B" & Fstart & ":B" & Fend
210     ActiveSheet.Range(Cells(rownum, colnum), Cells(rownum, colnum)).Select
211     ActiveSheet.Range(Cells(rownum, colnum), Cells(rownum, colnum)).Value = _
212         Application.WorksheetFunction.Correl(Range(Frange), Range(Lsrange))
213
214 End Sub
215 Sub s_relation()
216 '
217 ' s_relation Macro
218 '
219 '
220     Range("R7").Select
221     ActiveCell.FormulaR1C1 = "=R[-1]C[-10]/R[-1]C[-9]"
222     Range("S7").Select
223     Application.CutCopyMode = False
224     Selection.FormulaR1C1 = "=R[-1]C[-11]/R[-1]C[-9]"
225     Range("R7:S7").Select
226     Selection.Copy
227     Range("R8").Select
228     Selection.PasteSpecial Paste:=xlPasteValues, Operation:=xlNone, SkipBlanks _
229         :=False, Transpose:=False
230     Application.CutCopyMode = False
231     Range("N1").Select
232     Selection.FormulaR1C1 = "0.4"
233     Range("I6").Select
234     Application.CutCopyMode = False
235     ActiveCell.FormulaR1C1 = "=RC[-1]/R[2]C[9]"
236     Range("J6").Select
237     Application.CutCopyMode = False
238     Selection.FormulaR1C1 = "=RC[-2]/R[2]C[9]"
239 End Sub

```

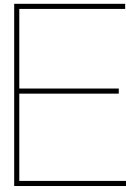
D.3. Compression test

```

1 Attribute VB_Name = "Module2"
2 Sub compression()
3 Attribute compression.VB_ProcData.VB_Invoke_Func = "t\n14"
4 '
5 ' compresison macro
6 ' Keyboard Shortcut: Ctrl+o
7 '
8 'Find F_max
9 Range("I1").Select
10 Selection.FormulaR1C1 = "F_max"
11 Range("I2").Select
12 Selection.FormulaR1C1 = "=MAX(RC[-5]:R[1498]C[-5])"
13 'Calculate and locate F1 and F2
14 Range("J4").Select
15 Selection.FormulaR1C1 = "Row No"
16 Range("J5").Select
17 Selection.FormulaR1C1 = "LVDT1"
18 Range("J6").Select
19 Selection.FormulaR1C1 = "LVDT2"
20 Range("J7").Select
21 Selection.FormulaR1C1 = "S"
22 Range("K1").Select
23 Selection.FormulaR1C1 = 0.1
24 Range("K2").Select
25 Selection.FormulaR1C1 = "F1"
26 Range("K3").Select
27 Selection.FormulaR1C1 = "=R[-1]C[-2]*R[-2]C"
28 Range("K4").Select
29 Selection.FormulaR1C1 = "=MATCH(R[-1]C,R2C4:R800C4,1)+1"
30 Range("K5").Select
31 Selection.FormulaR1C1 = "=INDIRECT(""E""&R[-1]C)"
32 Range("K6").Select
33 Selection.FormulaR1C1 = "=INDIRECT(""F""&R[-2]C)"
34 Range("K7").Select
35 Selection.FormulaR1C1 = "=INDIRECT(""G""&R[-3]C)"
36
37 Range("L1").Select
38 Selection.FormulaR1C1 = 0.4
39 Range("L2").Select
40 Selection.FormulaR1C1 = "F2"
41 Range("L3").Select
42 Selection.FormulaR1C1 = "=R[-1]C[-3]*R[-2]C"
43 Range("L4").Select
44 Selection.FormulaR1C1 = "=MATCH(R[-1]C,R2C4:R800C4,1)+1"
45 Range("L5").Select
46 Selection.FormulaR1C1 = "=INDIRECT(""E""&R[-1]C)"
47 Range("L6").Select
48 Selection.FormulaR1C1 = "=INDIRECT(""F""&R[-2]C)"
49 Range("L7").Select
50 Selection.FormulaR1C1 = "=INDIRECT(""G""&R[-3]C)"
51
52 Range("I10").Select
53 Selection.FormulaR1C1 = "F2-F1"
54 Range("J10").Select
55 Selection.FormulaR1C1 = "S"
56 Range("K10").Select
57 Selection.FormulaR1C1 = "del_LVDT1"
58 Range("L10").Select
59 Selection.FormulaR1C1 = "del_LVDT2"
60 Range("I9").Select
61 Selection.FormulaR1C1 = "=R[-6]C[3]-R[-6]C[2]"
62 Range("J9").Select
63 Selection.FormulaR1C1 = "=R[-2]C[2]-R[-2]C[1]"
64 Range("K9").Select
65 Selection.FormulaR1C1 = "=R[-4]C[1]-R[-4]C"
66 Range("L9").Select
67 Selection.FormulaR1C1 = "=R[-3]C-R[-3]C[-1]"
68
69 'Create Force-displacement graphs

```

```
70 Columns("I:L").Select
71 Columns("I:L").EntireColumn.AutoFit
72 Range("I12").Select
73 ActiveSheet.Shapes.AddChart2(240, xlXYScatterLinesNoMarkers).Select
74 ActiveChart.SeriesCollection.NewSeries
75 ActiveChart.FullSeriesCollection(1).Name = "=Filtered!$G$1"
76 ActiveChart.FullSeriesCollection(1).XValues = "=Filtered!$G$2:$G$1500"
77 ActiveChart.FullSeriesCollection(1).Values = "=Filtered!$D$2:$D$1500"
78 ActiveSheet.Shapes("Chart 1").IncrementLeft -100
79 ActiveSheet.Shapes("Chart 1").ScaleHeight 0.9079862934, msoFalse, _
80     msoScaleFromTopLeft
81
82 Range("O13").Select
83 ActiveSheet.Shapes.AddChart2(240, xlXYScatterLinesNoMarkers).Select
84 ActiveSheet.Shapes("Chart 2").IncrementLeft 210.75
85 ActiveSheet.Shapes("Chart 2").IncrementTop -51
86 ActiveSheet.Shapes("Chart 2").ScaleHeight 0.90625, msoFalse, _
87     msoScaleFromTopLeft
88 ActiveChart.SeriesCollection.NewSeries
89 ActiveChart.FullSeriesCollection(1).Name = "=Filtered!$E$1"
90 ActiveChart.FullSeriesCollection(1).XValues = "=Filtered!$E$2:E1500"
91 ActiveChart.FullSeriesCollection(1).Values = "=Filtered!$D$2:$D$1500"
92 ActiveChart.SeriesCollection.NewSeries
93 ActiveChart.FullSeriesCollection(2).Name = "=Filtered!$F$1"
94 ActiveChart.FullSeriesCollection(2).XValues = "=Filtered!$F$2:F1500"
95 ActiveChart.FullSeriesCollection(2).Values = "=Filtered!$D$2:$D$1500"
96
97 ActiveChart.SetElement (msoElementLegendRight)
98 ActiveChart.ChartArea.Copy
99 Range("O28").Select
100 ActiveSheet.Paste
101 ActiveWindow.SmallScroll Down:=6
102 ActiveSheet.ChartObjects("Chart 3").Activate
103 ActiveChart.Axes(xlCategory).Select
104 ActiveChart.Axes(xlCategory).MaximumScale = 0.5
105 Range("L33").Select
106 End Sub
```



Appendix - E

E.1. Parametrization

Because of the scattering that can be observed in the bending strength vs global static MOE (figure 4.8b), two boards were chosen, one (PNH1-1) in the lower 10th percentile and one (PNH68) in the top 10th percentile of the data, in such a way that they lie as close to the trend-line as possible and were named W (Weak) and S (Strong) sheets. Similar to how PNH133-1 was calibrated for its force-displacement relationship with the numerical and experimental agreeing with each other, both of these sheets were calibrated to obtain an f-d diagram as shown in figure E.1b.

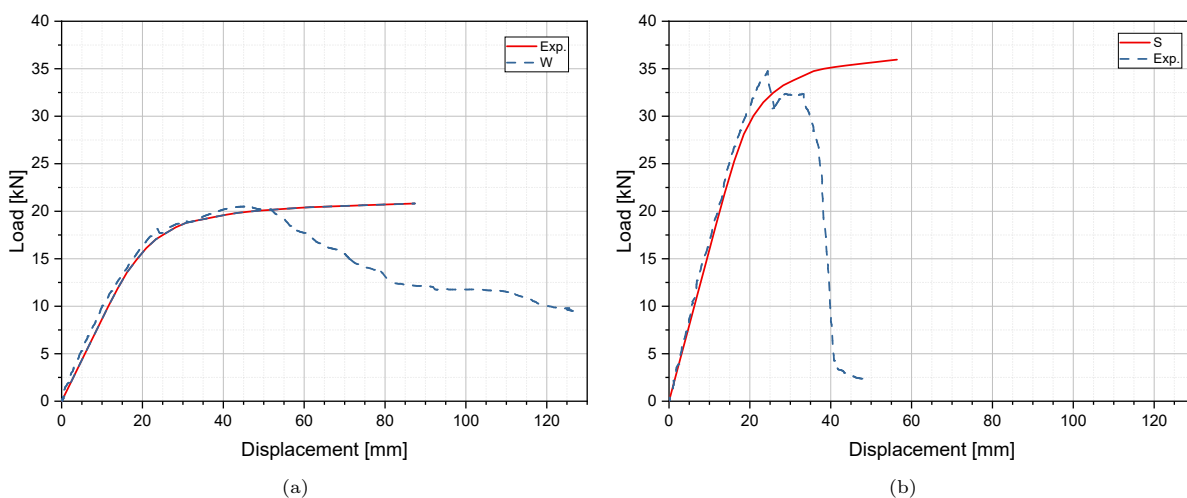


Figure E.1: Experimental vs numerical force-displacement curve (a) W, (b) S

From the set of sheet-pile wall systems that were simulated numerically, the model with 5 boards composed of 3D brick elements was chosen for parametrization. This was because of how close to the real problem the tongue and groove connection's definition was. The number of sheets was limited to 5 keeping the computation time in consideration. Based on the distribution of bending strength and global static MOE data in figures 4.5b and 4.5a, various possibilities of a setup that consists of 3 weak boards were considered. The three configurations WSWWS, SWWWS and WWSS were chosen to study how this impacts the bending strength and the stiffness of the entire sheet-pile wall system.

E.2. Results

The force-displacement curves obtained for each of the configurations are compared with fully strong (SSSSS), fully weak (WWWWW) and the initial brick model with PNH133-1 (AAAAA). No significant

difference was seen between each configuration as long as the number of weak sheets remains the same. As expected, the longitudinal stresses that are taken by S boards are significantly higher compared to that taken by W boards and the stress distribution along the depth for each of the boards is shown in figure E.3. Anyhow, this difference in stress remains unchanged within the three configurations considered.

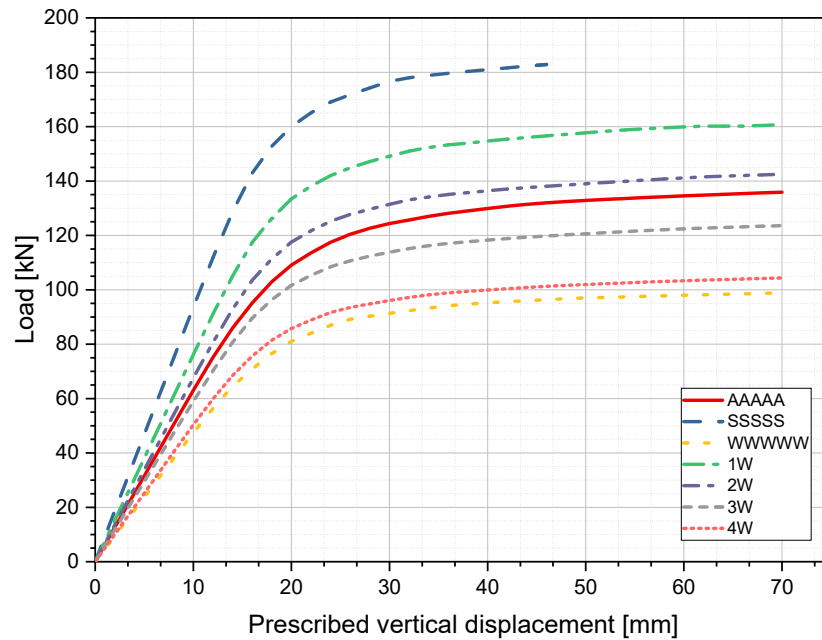


Figure E.2: Force-displacement plot of different parametrized configurations

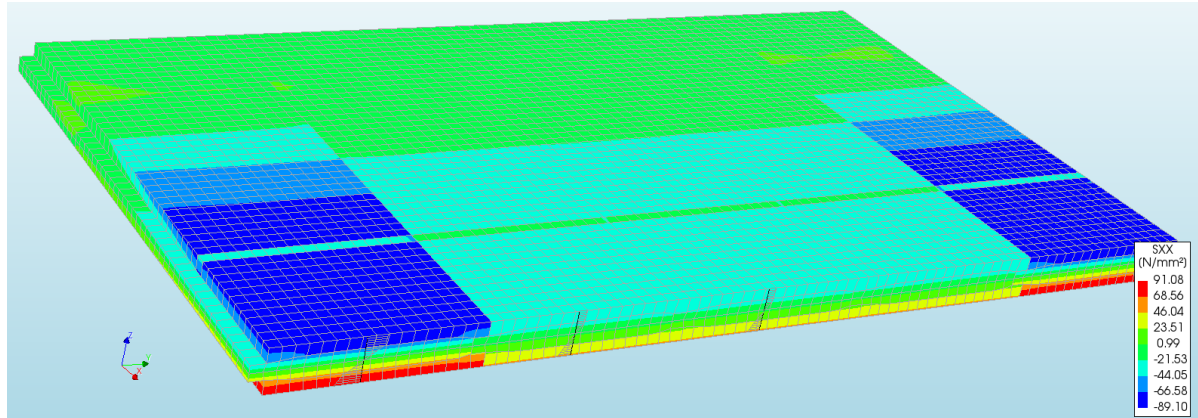
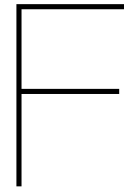


Figure E.3: Contour plot of the stress along x-direction for SWWWS configuration showing the cross-section stress distribution of each board



Appendix - F

In this chapter, the results from the RPD test performed on different samples with delay holes are shown as feed and drill amplitude percentage versus depth percentage graphs.

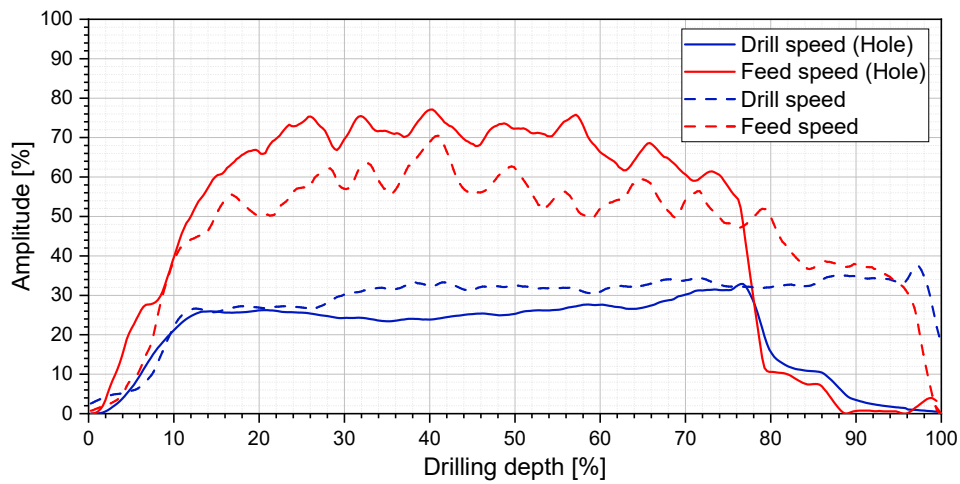


Figure F.1: RPD curves - drill at ideal location vs through a hole (PNH92-1)

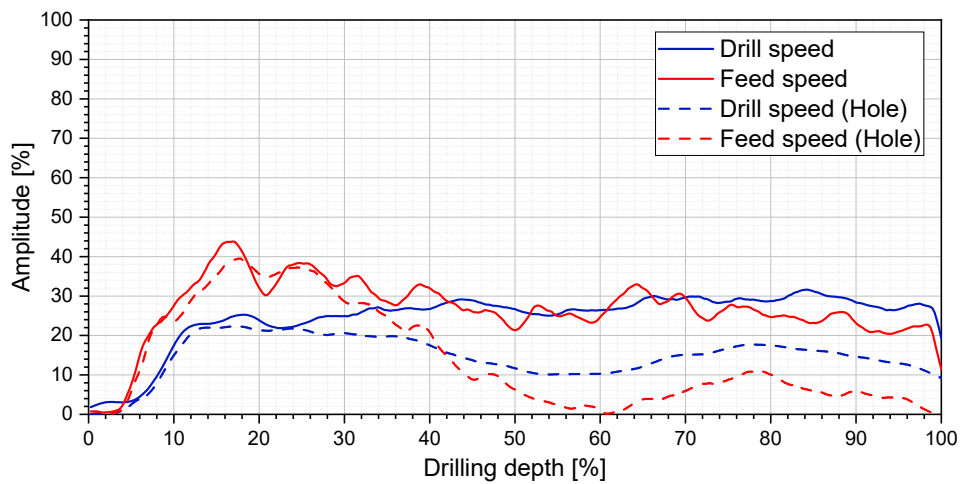


Figure F.2: RPD curves - drill at ideal location vs through a cavity (PNH87)

Bibliography

- Abrami, G. (2005). Decay in wooden foundations, the Italian situation. Final report EU project EVK4-CT 2001-00043: Preserving Cultural Heritage by Preventing Bacterial Decay of Wood in Foundation Piles and Archaeological Sites Chapter, 2, 34–45.
- Anagnostopoulou, V., & Pournou, A. (2013). Correlating visual grading with ntd methods for assessing timber condition in historic buildings. *Advanced Materials Research*, 778, 273–280.
- Barker, B., & Owen, N. L. (1999). Identifying softwoods and hardwoods by infrared spectroscopy. *Journal of chemical education*, 76(12), 1706.
- Bongers, H., & Beckers, E. (2003). Mechanical properties of acetylated solid wood treated on pilot plant scale. *Proceedings of the First European Conference on Wood Modification*, 341–350.
- Ceccato, F., Simonini, P., & Lionello, A. (2013). Long-term mechanical behavior of wooden pile foundation in Venice. *Geotechnical Engineering for the Preservation of Monuments and Historic Sites*, 249–257.
- Ceccotti, A., & Togni, M. (1996). Ndt on ancient timber beams: Assessment of strength/stiffness properties combining visual and instrumental methods. *Proceedings of the 10th International Symposium on Nondestructive Testing of Wood*, Lausanne, Switzerland, 26–28.
- Chaouch, M., Pétrissans, M., Pétrissans, A., & Gérardin, P. (2010). Use of wood elemental composition to predict heat treatment intensity and decay resistance of different softwood and hardwood species. *Polymer Degradation and Stability*, 95(12), 2255–2259.
- Dackermann, U., Crews, K., Kasal, B., Li, J., Riggio, M., Rinn, F., & Tannert, T. (2014). In situ assessment of structural timber using stress-wave measurements. *Materials and structures*, 47(5), 787–803.
- Dolwin, J., Lonsdale, D., & Barnett, J. (1999). Detection of decay in trees. *Arboricultural Journal*, 23(2), 139–149.
- Ehrhart, T., Steiger, R., & Frangi, A. (2018). A non-contact method for the determination of fibre direction of European beech wood (*Fagus sylvatica* L.). *European Journal of Wood and Wood Products*, 76(3), 925–935.
- Feio, A., Machado, J., & Lourenço, P. B. (2005). Compressive behavior and ndt correlations for chestnut wood (*Castanea sativa* Mill.) *Structural Analysis of Historical Constructions*, 369–375.
- Ferreira, D., & Manie, J. (2022). Diana reference manual. release 10.6 (tech. rep.). DIANA FEA BV, Thijsseweg 11, 2629 JA Delft, The Netherlands.
- Gard, W., & Van de Kuilen, J. (2018). Micro-drilling resistance measurements of dense hardwoods for hydraulic structures. *WCTE-World Conference on Timber Engineering*, Seoul, South-Korea.
- Hill, R. (1948). A theory of the yielding and plastic flow of anisotropic metals. *Proceedings of the Royal Society of London. Series A. Mathematical and Physical Sciences*, 193(1033), 281–297.
- Hoffman, O. (1967). The brittle strength of orthotropic materials. *Journal of Composite Materials*, 1(2), 200–206.
- Kamath, A. (2022). Bio-engineered earth retaining structure (beers): A timber sheet pile-vegetation system for stream bank protection.
- Kasal, B., & Tannert, T. (2011). In situ assessment of structural timber (Vol. 7). Springer Science & Business Media.
- Klaassen, K., Jorissen, A., & Keijer, H. (2015). Life expectation of wooden foundations a non-destructive approach. *Proceedings of the International Symposium Non-Destructive Testing in Civil Engineering (NDT-CE)*, Berlin, Germany, 15–17.
- Klaassen, R. K., & Creemers, J. G. (2012). Wooden foundation piles and its underestimated relevance for cultural heritage. *Journal of cultural heritage*, 13(3), S123–S128.
- Koczan, G., & Kozakiewicz, P. (2017). The role of shear stress in the bending strength test of short and medium length specimens of clear wood. *Drewno: prace naukowe, doniesienia, komunikaty*, 60.
- Lechner, T., Nowak, T., & Kliger, R. (2014). In situ assessment of the timber floor structure of the skansen lejonet fortification, Sweden. *Construction and Building Materials*, 58, 85–93.

- NEN-1311. (1997). Round and sawn timber - method of measurement of biological degrade. Nederlands Normalisatie-instituut, Delft, The Netherlands.
- NEN-EN-13183-1. (2002). Moisture content of a piece of sawn timber - part 1:determination by oven dry method. Nederlands Normalisatie-instituut, Delft, The Netherlands.
- NEN-EN-14081. (2019). Timber structures - strength graded structural timber with rectangular cross section. Nederlands Normalisatie-instituut, Delft, The Netherlands.
- NEN-EN-14358. (2016). Timber structures - calculation and verification of characteristic values. Nederlands Normalisatie-instituut, Delft, The Netherlands.
- NEN-EN-338. (2016). Structural timber - strength classes. Nederlands Normalisatie-instituut, Delft, The Netherlands.
- NEN-EN-384. (2022). Structural timber - determination of characteristic values of mechanical properties and density. Nederlands Normalisatie-instituut, Delft, The Netherlands.
- NEN-EN-408. (2010). Timber structures - structural timber and glued laminated timber - determination of some physical and mechanical properties. Nederlands Normalisatie-instituut, Delft, The Netherlands.
- NEN-EN-5493. (2010). Quality requirements for deciduous wood in ground, road and hydraulic engineering works and other constructional applications. Nederlands Normalisatie-instituut, Delft, The Netherlands.
- Niemz, P., & Mannes, D. (2012). Non-destructive testing of wood and wood-based materials. *Journal of Cultural Heritage*, 13(3), S26–S34.
- Nilsson, T., & Rowell, R. (2012). Historical wood–structure and properties. *Journal of Cultural Heritage*, 13(3), S5–S9.
- Nowak, T., Karolak, A., Sobótka, M., & Wyjadowski, M. (2019). Assessment of the condition of wharf timber sheet wall material by means of selected non-destructive methods. *Materials*, 12(9), 1532.
- Ravenshorst, G., Gard, W., & van de Kuilen, J. W. (2020). Influence of slope of grain on the mechanical properties of tropical hardwoods and the consequences for grading. *European Journal of Wood and Wood Products*, 78(5), 915–921.
- Ravenshorst, G. J. P. (2015). Species independent strength grading of structural timber.
- Ravenshorst, G., de Vries, P., & van de Kuilen, J.-W. (2014). Aspects of the difference between the local and global modulus of elasticity of structural (hardwood) timber. In *Materials and joints in timber structures* (pp. 773–783). Springer.
- Riggio, M., Anthony, R. W., Augelli, F., Kasal, B., Lechner, T., Muller, W., & Tannert, T. (2014). In situ assessment of structural timber using non-destructive techniques. *Materials and structures*, 47(5), 749–766.
- Ross, R. J., Pellerin, R. F., Volny, N., Salsig, W. W., & Falk, R. H. (1999). Inspection of timber bridges using stress wave timing nondestructive evaluation tools: A guide for use and interpretation. US Department of Agriculture, Forest Service, Forest Products Laboratory, Madison, Report FPL-GTR, 114.
- Sandquist, D. (2011). Poplar wood formation (Vol. 2011).
- Sass-Klaassen, U., Vernimmen, T., & Baittinger, C. (2008). Dendrochronological dating and provenancing of timber used as foundation piles under historic buildings in the netherlands. *International Biodeterioration & Biodegradation*, 61(1), 96–105.
- Shapiro, S. S., & Wilk, M. B. (1965). An analysis of variance test for normality (complete samples). *Biometrika*, 52(3/4), 591–611.
- Sharapov, E., Brischke, C., Militz, H., & Smirnova, E. (2019). Prediction of modulus of elasticity in static bending and density of wood at different moisture contents and feed rates by drilling resistance measurements. *European Journal of Wood and Wood Products*, 77(5), 833–842.
- Sousa, H. S., Branco, J. M., Machado, J. S., & Lourenço, P. B. (2017). Predicting mechanical properties of timber elements by regression analysis considering multicollinearity of non-destructive test results.
- Tannert, T., Anthony, R. W., Kasal, B., Kloiber, M., Piazza, M., Riggio, M., Rinn, F., Widmann, R., & Yamaguchi, N. (2014). In situ assessment of structural timber using semi-destructive techniques. *Materials and structures*, 47(5), 767–785.
- Turnbull, A., & Crocker, L. (2014). Four point bend testing-finite element analysis of the stress and strain distribution.

- Van de Kuilen, J., & BlaSS, H. J. (2005). Mechanical properties of azobé (*lophira alata*). *Holz als Roh-und Werkstoff*, 63(1), 1–10.
- Van de Kuilen, J., & Van Der Linden, M. (1999). Reliability based design of timber sheet pile walls. *NZ Timber Des J*, 11(1), 11–16.
- van de Kuilen, J., van der Linden, M., Katsma, H., & Stolle, P. (1996). Full size testing of sheet pile walls.
- Van der Linden, M., Van de Kuilen, J., & Blass, H. (1994). Application of the hoffmann yield criterion for load sharing in timber sheet pile walls. *Pacific Timber Engineering Conference,(PTEC) Gold Coast, Australia 1994*, 412–417.
- Wang, X., Divos, F., Pilon, C., Brashaw, B. K., Ross, R. J., & Pellerin, R. F. (2004). Assessment of decay in standing timber using stress wave timing nondestructive evaluation tools: A guide for use and interpretation. *Gen. Tech. Rep. FPL-GTR-147*. Madison, WI: US Department of Agriculture, Forest Service, Forest Products Laboratory, 2004. 12 pages, 147.
- Wang, X., Wiedenbeck, J., Ross, R. J., Forsman, J. W., Erickson, J. R., Pilon, C., & Brashaw, B. K. (2005). Nondestructive evaluation of incipient decay in hardwood logs. *Gen. Tech. Rep. FPL-GTR-162*. Madison, WI: US Department of Agriculture, Forest Service, Forest Products Laboratory. 11 pages, 162.
- Wood Handbook, C. (2010). *Wood handbook*. Forest.
- Xu, B.-H., Bouchar, A., & Racher, P. (2012). Analytical study and finite element modelling of timber connections with glued-in rods in bending. *Construction and Building Materials*, 34, 337–345.
- Xu, B.-H., Taazount, M., Bouchar, A., & Racher, P. (2009). Numerical 3d finite element modelling and experimental tests for dowel-type timber joints. *Construction and Building Materials*, 23(9), 3043–3052.